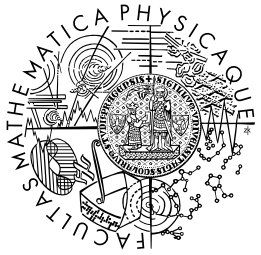

FACULTY
OF MATHEMATICS
AND PHYSICS
Charles University

DOCTORAL THESIS

Ekaterina Matveeva

Studies of plasma disruptions in the COMPASS tokamak

Department of Surface and Plasma Physics

Supervisor of the doctoral thesis:	RNDr. Milan Tichý, Dr.Sc.
Study programme:	Physics
Study branch:	Physics of Plasmas and Ionised Media

Prague 2022

I declare that I carried out this doctoral thesis independently, and only with the cited sources, literature and other professional sources.

I understand that my work relates to the rights and obligations under the Act No. 121/2000 Sb., the Copyright Act, as amended, in particular the fact that the Charles University has the right to conclude a license agreement on the use of this work as a school work pursuant to Section 60 subsection 1 of the Copyright Act.

In ..... date ..... signature of the author

I would like to express my deepest gratitude to my supervisor RNDr. Milan Tichý, Dr.Sc. and advisors Dr. Josef Havlíček and Dr. Vladimir Weinzettl for their continuous support throughout my PhD journey. They offered an exciting research topic on the cutting edge of tokamak physics. They shared ideas and were there to help me even at their busiest time.

I am profoundly grateful to Dr. Michael Lehnen, Dr. Sergei Gerasimov, Dr. Javier Artola, Dr. Vadim Yanovskiy, Dr. Vladimir Pustovitov, Dr. Leonid Zakharov, Dr. Jiří Adámek for fruitful discussions that contributed greatly to my understanding of disruptions physics.

I would like to thank the Department of Surface and Plasma Science at the Charles University for giving me an opportunity to carry out my PhD research in Prague and providing great academic environment.

I would like to thank the COMPASS team for creating inspiring and friendly work atmosphere.

Many thanks to my fellow students and friends: Galina Avdeeva, Sundaresan Sridhar, Irina Borodkina, Kirill Volosnikov and many others. Their kind help and support have made my studies a wonderful time.

I would like to thank my parents and my husband for their kindness and encouragement. They were there for me through all of the ups and downs and completion of this thesis would not be possible without them.

And last but not least, I am grateful to my supervisors during my bachelor and master studies - Dr. Sergei Tolstyakov and Dr. Nicolas Lemoine, who taught me the foundations of scientific work and shared their enthusiasm about fusion research.

Title: Studies of plasma disruptions in the COMPASS tokamak

Author: Ekaterina Matveeva

Department: Department of Surface and Plasma Physics

Supervisor: RNDr. Milan Tichý, Dr.Sc., Univerzita Karlova, Katedra fyziky povrchů a plazmatu

Abstract:

Plasma disruption in a tokamak is an important physical phenomenon, when there is a sudden loss of plasma confinement and rapid drop of plasma current. During the disruptions, there is significant mechanical stress on the constructional structures of the tokamak and thermal stress on the first wall. Allowable number of disruptions with the maximum plasma parameters in the ITER tokamak (international thermonuclear experimental reactor under construction) will be very limited. Therefore, investigation of disruptions and their consequences is a key problem for sustainable operation of tokamak devices.

The thesis focuses on studies of current quench phase and related currents flowing in the vacuum vessel at the COMPASS tokamak. An extensive disruption database was collected and critical disruptions' parameters were determined. Plasma current was measured at 5 toroidal position as a consequence of data acquisition system improvement that allowed reliable measurements by magnetic coils without analogue integrators. Special divertor tiles were installed in order to perform dedicated vertical displacement event (VDE) experiments and validate asymmetric toroidal eddy currents model (Roccella et al, Asymmetric toroidal eddy currents (ATEC) to explain sideways forces at JET, 2016). It was shown that the gaps between the plasma facing components (PFCs) can be short-circuited during disruptions creating a parallel vessel current circuit, previously neglected. This brings new perspective on estimation of electromagnetic forces acting on the vacuum vessel and PFCs. A unique set of magnetic diagnostics was used to measure poloidal and toroidal vessel currents including their distribution in poloidal cross-section. New magnetic coils were put into operation allowing measurement of halo current and their poloidal extension. The results contributed to confirmation of a hypothesis that halo current density might be limited by ion saturation current.

Keywords: fusion, tokamak, disruption, magnetic diagnostics, halo currents

Název: Studium disrupcí plazmatu v tokamaku COMPASS

Autor: Ekaterina Matveeva

Katedra: Katedra fyziky povrchů a plazmatu

Vedoucí: RNDr. Milan Tichý, Dr.Sc., Univerzita Karlova, Katedra fyziky povrchů a plazmatu

Abstrakt:

Disrupce plazmatu v tokamaku jsou důležitým fyzikálním jevem, kdy dochází k náhlé ztrátě udržení plazmatu a k prudkému poklesu proudu v plazmatu. Během disrupcí dochází k výraznému mechanickému namáhání konstrukčních struktur tokamaku a k tepelnému zatížení první stěny. Přípustný počet disrupcí při maximálních parametrech plazmatu bude v tokamaku ITER (mezinárodní termonukleární experimentální reaktor ve výstavbě) velmi omezený. Vyšetřování disrupcí a jejich následků je proto klíčovým problémem pro udržitelný provoz zařízení typu tokamak.

Tato práce se zaměřuje na studium fáze poklesu proudu a souvisejících proudů tekoucích ve vakuové komoře na tokamaku COMPASS. Byla shromážděna rozsáhlá databáze disrupcí a byly stanoveny kritické parametry disrupcí. Proud plazmatu byl měřen v 5 toroidálních polohách díky vylepšenému systému sběru dat, který umožnil spolehlivá měření magnetickými cívkami bez analogových integrátorů. Byly instalovány speciální divertorové desky, aby bylo možné provádět specializované experimenty s definovanými událostmi vertikálního přesunu (vertical displacement event, VDE) a ověřit model asymetrických toroidálních vířivých proudů (Roccella et al, Asymmetric toroidal eddy currents (ATEC) to explain sideways forces at JET, 2016). Bylo ukázáno, že mezery mezi komponentami vystavené plazmatu (plasma fasing components, PFC) mohou být zkratovány během disrupcí a mohou tak vytvářet vytvářet paralelní proudový obvod v komoře, který byl dříve zanedbáván. To přispělo k novému pohledu na odhad elektromagnetických sil působících na vakuovou komoru a PFC. Pro měření poloidálních a toroidálních proudů v komoře včetně jejich rozložení v poloidálním průřezu byla použita unikátní sada magnetické diagnostiky. Do provozu byly uvedeny nové magnetické cívky umožňující měření halo proudů včetně zvětšení jejich poloidálního rozsahu. Výsledky přispěly k potvrzení hypotézy, že hustota halo proudů může být omezena saturačním proudem iontů.

Klíčová slova:

fúze, tokamak, disrupce, magnetická diagnostika, halo proudy

Contents

Introduction

Fusion power is a leading candidate for safe energy generation. Power plants based on thermonuclear reactions can provide carbon-free electricity while keeping the presence of radioactive fuel to minimum during operation. Lower production of nuclear waste and increased safety against nuclear disasters are major advantages of the fusion power concept. In addition to this, a fusion power plant does not depend on weather conditions (e.g. sunlight, wind, tides) and is almost non-dependent on the geographical properties of natural resources of the area where it is located.

Fusion power energy is a promising solution to overcome an energy crisis humanity is facing. However, creation of a first working fusion power plant producing net energy is a tremendous challenge and requires cooperation of scientists from various research fields as well as engineers. There are a number of approaches to fusion power generation. These include magnetic confinement (e.g. tokamaks, stellarators), inertial confinement, magnetic pinches.

A tokamak is a wide-spread device for fusion research. It was first proposed in the USSR in the 1950s and the name stands for Toroidal Vessel in Magnetic Coils in Russian. Over the past decades tokamak research has progressed enormously. Tokamak devices have been built in more than 15 countries. ITER [1], which is being built in the south of France, will be the biggest tokamak in the world and aiming to be the first one to produce net fusion energy.

Sustainable operation of the future fusion devices might be prevented by an event called disruption. Disruption is an abrupt loss of magnetic confinement, resulting in a termination of a tokamak discharge. On top of that, it leads to enormous thermal and electromagnetic loads on the vacuum vessel which might result in irreversible damage to the machine.

Goals and thesis overview

The motivation of this work is to contribute to understanding of electromagnetic loads on the tokamak vacuum vessel during disruptions. The thesis aims to study disruptions at the COMPASS tokamak. The focus is on the currents flowing in the vacuum vessel and their relation to the plasma current quench and vertical displacement during disruptions. The goals include:

- Collection of disruption database at COMPASS.
- Statistical analysis of current quench characteristics.
- Improvement of the data acquisition system performance for discrete magnetic coils and connection of the new coils.
- Measurement of local poloidal and toroidal vessel currents during disruptions.
- Analysis of special type of disruptive vessel currents - halo currents.
- Investigation of possible toroidal asymmetries of the plasma during disruptions.

- Studies of possible current paths through the vacuum vessel and plasma facing components (ATEC experimental model validation).

The work was carried out in the Institute of Plasma Physics of Academy of Sciences of the Czech Republic (IPP CAS) in Prague. Significant part of the work related to ATEC model validation was performed in collaboration with ITER Organisation under two service contracts. In addition to this, several visits to JET at Culham Centre for Fusion Energy (UK) contributed to investigation of toroidally asymmetrical disruptions.

The thesis starts with an introduction to plasma confinement in chapter 1. Section 1.1 presents reactions used in fusion research and criteria for reaching self-sustainable operation of a fusion reactor. Section 1.2 focuses on a specific type of fusion devices - tokamaks. It briefly describes basic tokamak working principles and related plasma physics. Section 1.3 provides an overview of the COMPASS tokamak. Operational parameters, available diagnostics and main research topics are outlined.

Chapter 2 comprises main phases if disruption phenomenon and underlying physics. Section 2.1 presents tokamak operational limits and possible disruption causes. Section 2.2 focuses on electromagnetic loads on the vacuum vessel during disruptions. It describes each disruption phase individually introducing related vessel currents. It also defines main disruption types such as vertical displacement event, major disruption, asymmetrical disruption.

Chapter 3 contains the major results of this thesis. It starts with statistical overview of disruptions at COMPASS and points out their specific features. The following part comprises several topics:

- Section 3.1 describes magnetic diagnostics used for disruptions investigation at COMPASS. It presents in details magnetic coils characteristics, challenges of their signal processing and possible solutions. It also shows how one of the major plasma parameters - the plasma current can be reconstructed using discrete magnetic coils.

- Sections 3.2 and 3.3 summarise statistical analysis of the plasma current quench features as well as poloidal and toroidal vessel currents at COMPASS. New findings related to possible limitation of the halo current density are presented. This work was described in details in the author's paper attached to the thesis ("Current quench and vessel currents characterization at the COMPASS tokamak" was accepted for publication in Plasma Physics and Controlled Fusion journal in October 2022 and is now available online [2]).

- Section 3.4 is dedicated to toroidally asymmetrical disruptions at COMPASS. It deals with both plasma current and halo current toroidal asymmetries. Comparison with previous results at COMPASS and JET are presented.

- Section 3.5 comprises main results of dedicated disruption experiments carried out in collaboration with ITER Organization. New divertor tiles

specifically designed for direct measurement of halo current flows are described. Hypotheses to explain the observed current flows are discussed and the most reliable one (ATEC model) is pointed out.

Chapter 3.5 summarises the results of the thesis. The attachment contains the article that extends the results presented in sections 3.2 and 3.3.

1. Plasma confinement in tokamaks

1.1 Fusion reactions

Nuclear fusion reactor concept is based on gaining energy from exothermic fusion reactions, where the merging nuclei release kinetic energy according to mass-energy equivalence:

$$\Delta E = \Delta m c^2 \tag{1.1}$$

The particles involved in the reaction have to gain significant kinetic energy in order to overcome the Coulomb barrier. The reaction probability (or "cross-section" σ) with respect to the kinetic energy determines feasible reactants for potential fusion reactor. It was found that the most practical reaction with highest cross-section achieved at lowest temperature and also releasing large energy is fusion of hydrogen isotopes - deuterium and tritium:

$${}^{2}_{1}H + {}^{3}_{1}H \longrightarrow {}^{4}_{2}He(3.52MeV) + {}^{1}_{0}n(14.06MeV) \tag{1.2}$$

A large input of energy is required to initiate fusion reactions. However, with sufficient amount of released energy the reactions will become self-sustainable even without external energy source. The stage when the plasma is gaining energy from fusion reactions faster, than the energy loss to the environment is called ignition.

Ability of a fusion device to produce net energy without additional external heating is determined by so-called Lawson criterion:

$$n\tau_E \geq \frac{12k_B}{E_{fusion}} \frac{T}{\langle \sigma \upsilon \rangle} \tag{1.3}$$

where n is the plasma density, T - plasma temperature, τ_E - confinement time, E_{fusion} - energy produced by fusion reactions, $\langle \sigma \upsilon \rangle$ - product of the cross-section and the relative velocity of fusion reactions. The criterion is based on a requirement for the energy yield from fusion reactions being larger than the energy losses:

$$P_{fusion} = f E_{fusion} \geq P_{loss} \tag{1.4}$$

where f is a number of fusion reactions per volume per time. Assuming plasma with two ion species having densities n_1 and n_2 and Maxwellian velocity distribution:

$$f = n_1 n_2 \langle \sigma \upsilon \rangle \tag{1.5}$$

Therefore, the power produced by fusion reactions in volume V is defined as:

$$f E_{fusion} = n_1 n_2 \langle \sigma \upsilon \rangle V E_{fusion} = \frac{1}{4} n_e^2 \langle \sigma \upsilon \rangle V E_{fusion} \tag{1.6}$$

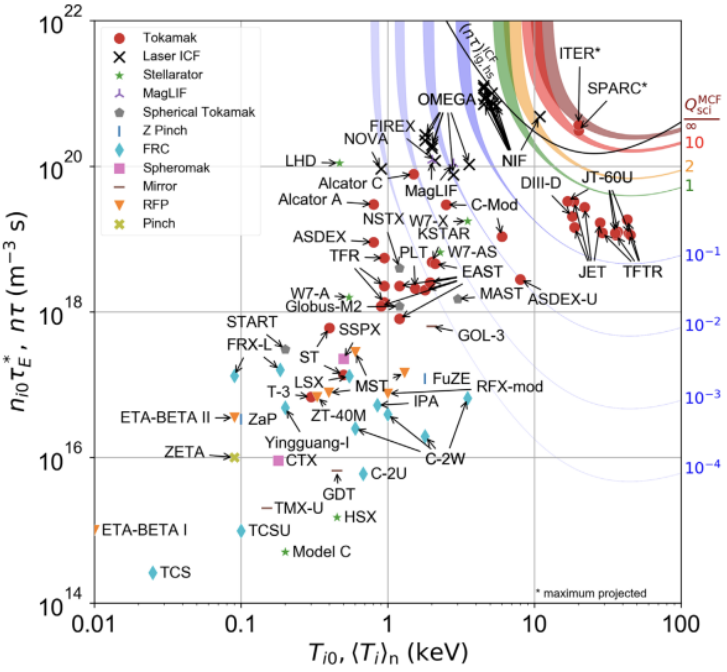

Figure 1.1: Lawson criterion shown for different concepts of fusion devices (Figure from [3]).

where we assume that $n_1 = n_2 = \frac{n_e}{2}$. Lawson criterion takes into account only radiation losses. Thermal energy stored in plasma is deduced using Boltzmann distribution (assuming equal temperature of the ions $T_1 = T_2 = T$):

$$E_{plasma} = \frac{3}{2} k_b (n_e T_e + n_1 T_1 + n_2 T_2) V = 3 k_B n_e T V \tag{1.7}$$

where n_e is the electron density and T_e is the electron temperature. So-called confinement time parameter is used to measure how fast plasma loses its energy:

$$\tau_E = \frac{E_{plasma}}{P_{loss}} \tag{1.8}$$

Therefore the Equation 1.4 transforms into:

$$\frac{1}{4} n_e^2 \langle \sigma v \rangle V E_{fusion} \geq \frac{E_{plasma}}{\tau_E} = \frac{3 k_B n_e T V}{\tau_E} \tag{1.9}$$

resulting in Lawson criterion (as in Equation 1.3). Its alternative - triple product is widely used to characterise fusion devices performance. It determines minimum necessary product of plasma density n_e, temperature T and confinement time τ_E required to achieve ignition:

$$n T \tau_E \geq \frac{12 k_B}{E_{fusion}} \frac{T^2}{\langle \sigma v \rangle} \tag{1.10}$$

The Lawson criterion or triple product are commonly used to asses fusion performance, and can be applied regardless of the machine concept (Figure 1.1).

1.2 Magnetic confinement in tokamaks

According to Lawson criterion, a balance between temperature, density and confinement time has to be found in order to achieve ignition. Fusion reactions in the Sun rely on high densities, while having temperatures ∼1 keV and enormous confinement time. For deuterium-tritium reactions on Earth the optimal temperature is ∼10 keV, and either density or confinement time has to be increased to fulfil Lawson criterion. Inertial confinement fusion (ICF) concept uses higher plasma densities ($\sim 10^{30} m^{-3}$), while having shorter confinement time ($\sim 10^{-9}$ s). On the other hand, magnetically confined fusion (MCF) approach has increased confinement time (∼1 s), while keeping lower densities ($\sim 10^{20} m^{-3}$).

Plasmas at energies of ∼10 keV cannot be contained having a direct contact with the walls of the vessel. MCF is one of the prominent concepts solving this problem by suspending the plasma in a vacuum using a complex configuration of magnetic field. As plasma consists of electrons and ions, it can be controlled by magnetic field: in uniform magnetic field the charged particles follow the magnetic field line gyrating around it with Larmor frequency due to Lorenz forces:

$$\omega_c = \frac{q_i B}{m_i} \tag{1.11}$$

where B is the magnetic field, q_i and m_i are the charge and the mass of the particle. The radius of the gyration is called Larmor radius and is defined as:

$$r_L = \frac{m_i v_\perp}{q_i B} \tag{1.12}$$

where $v_\perp$ is the particle velocity perpendicular to B. Then the field line can be closed by itself, e.g. in toroidal shape, in order to prevent particles escape. However, in toroidally-shaped devices the toroidal magnetic field lines are more dense on the inner side of the torus and more sparse on the outer side. Due to non-homogeneous toroidal field, the ions and the electrons undergo a drift in opposite directions creating charge separation and subsequent creation of an electric field **E**. The resulting $\mathbf{E} \times \mathbf{B}$ force leads to an outward expansion of the plasma, preventing confinement. The drift problem can be resolved by twisting the magnetic field lines into helical shape creating so-called 'rotational transform':

$$\iota = 2\pi \frac{d\Psi}{d\Phi} \tag{1.13}$$

where Ψ and Φ are poloidal and toroidal fluxes, respectively. Rotational transform is defined as the ratio of the number of turns magnetic field line travels in poloidal and toroidal directions. An inverse of rotational transform is called safety factor q and is commonly used when describing the confining magnetic fields in tokamaks:

$$q = \frac{d\Phi}{d\Psi} \tag{1.14}$$

The charged particles moving along the twisted magnetic field line still drift, but the direction of the drift changes throughout the travel time of the particles, which prevents the overall expansion of the plasma.

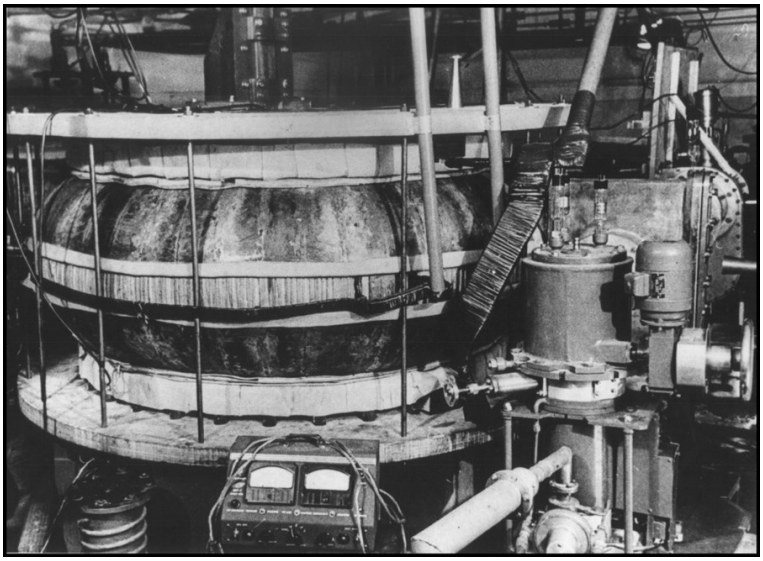

Figure 1.2: T-1 tokamak - the first operating device of this type in the world (figure from [4]).

The helical field can be generated with a complex 3D coils located outside of the vessel. This technique is used in stellarators. Alternative solution is applied in tokamaks, where the rotational transform is created by combination of the toroidal magnetic field from external coils and the poloidal magnetic field produced by the current running through the plasma.

The tokamak research was initiated in USSR by O.A. Lavrentiev, I.E. Tamm and A.D. Sakharov in 1950s. The name tokamak stands for Russian abbreviation of "toroidal chamber with magnetic coils". The first operating tokamak-type machine T-1 started operation in 1958 in Kurchatov Institute (Figure 1.2). Over the following decades a tokamak has become a leading candidate for a viable nuclear fusion reactor. Dozens of tokamak devices were constructed all over the world exploring various machines configurations. The largest currently operating tokamak JET was built in the UK in 1978-1983. International Thermonuclear Experimental Reactor (ITER), which is currently being built in France, is designed to be the first tokamak producing a net yield of energy and showing feasibility of tokamak-based fusion reactor.

A schematic example of the tokamak vacuum vessel and the fields confining the plasma is shown in Figure 1.3. An inner poloidal field coil (centre solenoid) is located in the center of the torus and works as a primary transformer circuit. The plasma serves as a secondary circuit of the transformer, allowing the induction of the current flowing in toroidal direction. The plasma current generates poloidal magnetic field, which together with the toroidal magnetic field (generated by the toroidal field coils) creates nested flux surfaces (formed by the twisted magnetic field lines). A tokamak is inherently a pulsed machine, since the direct-current (DC) drive requires monotonically time-varying magnetic field, which is limited by transformers capacity. The outer poloidal field coils are used for plasma position control and shaping. The inner part of the torus with stronger toroidal magnetic field is often referred to as high field side (HFS), while the outer part of the torus is called low field side (LFS).

Until the ignition conditions are reached, plasma needs a heating source to

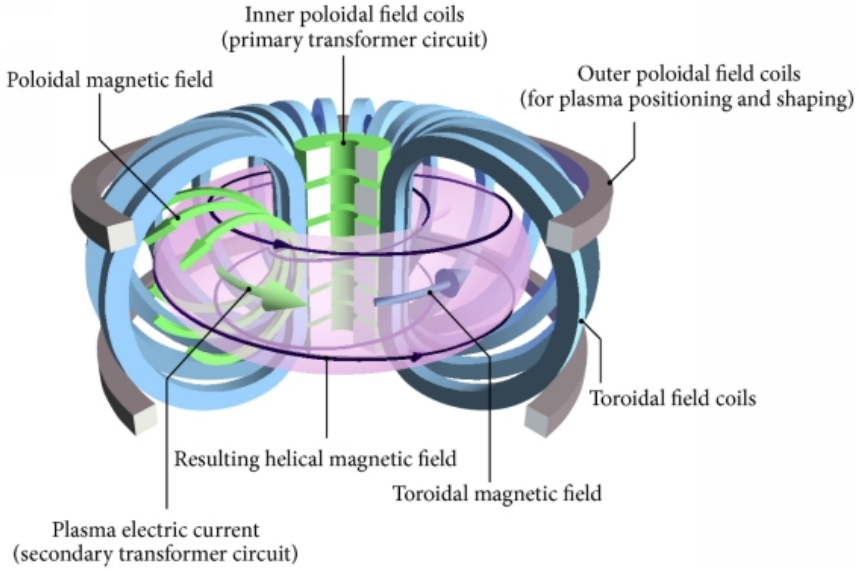

Figure 1.3: Schematic of the tokamak device concept (Image courtesy of EUROfusion).

compensate energy losses through radiation and convection. Firstly, the plasma is heated by the plasma current through ohmic heating. However, ohmic resistance of the plasma, which is determined by Spitzer conductivity, decreases as the plasma temperature grows as $R \sim T^{-\frac{3}{2}}$. Therefore, additional heating techniques are required beyond few keV plasma temperature. These includes:

- Neutral beam injection (NBI): neutrals with high kinetic energy are injected into plasma, where they become ionized and transfer their energy to the surrounding particles.
- Radio-frequency heating (RF): RF waves transfer their electromagnetic energy to ions and electrons by exciting the resonance at certain frequencies, such as electron cyclotron resonance (used in ECRH and ECCD), ion cyclotron resonance (used in ICRH), lower hybrid resonance (used in LHCD).

A so-called fusion energy gain parameter Q is used to express the ratio between the power produced by the fusion reactions and the power used for the heating:

$$Q = \frac{P_{fusion}}{P_{heat}} \tag{1.15}$$

The moment when Q=1 is reached is called breakeven, which has not yet been achieved by any device (the record among tokamaks Q = 0.67 is hold by JET). For self-sustainable operation of the machine (ignition) at least $Q \approx 5$ is required.

Many tokamaks are equipped with a divertor - specifically designed plates inside the vacuum vessel, which prevent accumulation of impurities and allows improved plasma confinement. A schematic representation of a diverted plasma is shown in Figure 1.4. The region of the hot plasma contained by the nested magnetic flux surfaces is separated from the open magnetic field lines region by the separatrix (last closed flux surface - LCFS). The X-point is the area where

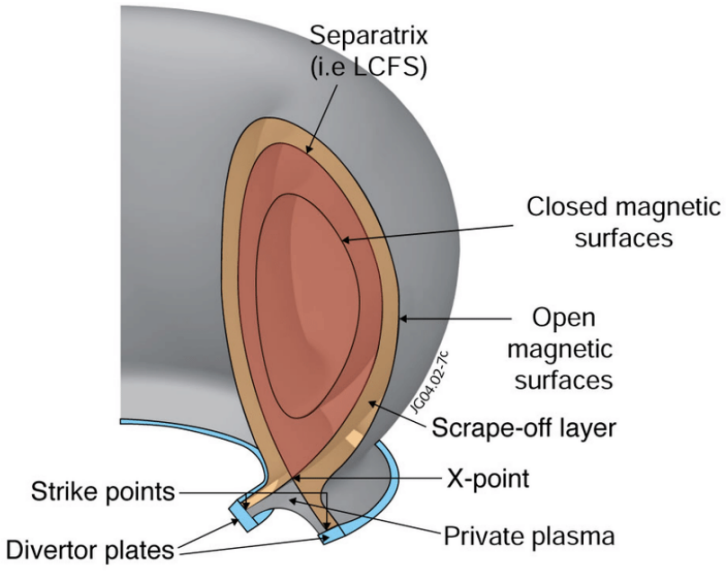

Figure 1.4: A cross-section of a tokamak vacuum vessel showing the plasma in a single-null diverted configuration with lower X-point (Figure from EFDA-JET).

the poloidal magnetic field becomes zero. The intersections of the separatrix with the divertor are called the strike points, and the area between them is the private plasma (or private flux region). The open magnetic field line area is referred to as the scrape-off layer (SOL). The field lines in SOL are guided (diverted) towards the divertor plates. The particles travelling along these field lines are pumped out in the divertor region, allowing removal of released impurities and helium "ash" from fusion reactions as well as preventing contact of the hot plasma with the rest of the vacuum vessel and in-vessel components.

Tokamak plasmas can deviate from circular cross-section (as in the case of diverted plasma), which is expressed by plasma elongation κ and triangularity δ:

$$\kappa = \frac{b}{a}$$
$$\delta_{upper/lower} = \frac{R_{geo} - R_{upper/lower}}{a} \tag{1.16}$$

In Equation 1.16 a is the minor radius of the plasma defined as the radial distance between inner and outer sides of LCFS in the midplane; b is the vertical distance from the midplane to the maximum (or minimum) vertical coordinate of LCFS (Figure 1.5). Plasma triangularity is defined as the difference between the radius of the geometrical axis of the plasma and the radius of highest or lowest points of LCFS. Therefore, upper and lower triangularities can be distinguished.

While tokamak is a promising concept in fusion research, it faces numerous difficulties, both technical and physical. Operation of a tokamak requires advanced technologies of plasma heating, handling plasma facing components (PFCs) interaction with high-energy plasmas, cutting-edge diagnostics for plasma control and many more. The presence of the current running through the plasma column is a primary source of various MHD instabilities, which might lead to a loss of the plasma confinement and sudden termination of the discharge (disruption). Therefore, disruptions investigation is a distinct challenge in tokamak fusion plasmas.

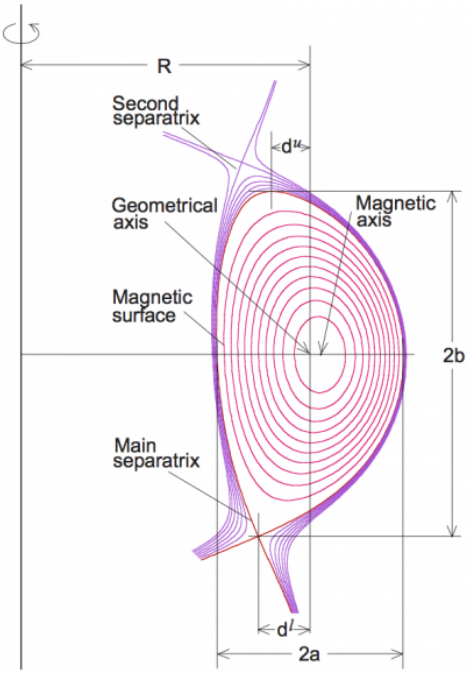

Figure 1.5: Schematic representation of plasma elongation and triangularity in a single-null diverted configuration with lower X-point.

1.3 The COMPASS tokamak

The machine was originally designed in Culham Science Centre, the United Kingdom, where it worked until 2001 as COMPASS-D. It was then reinstalled as COMPASS in the Institute of Plasma Physics (IPP) of the CAS in Prague in 2007 [5] (Figure 1.6), first plasma was achieved in 2008 [6]. It operated until permanent shut-down in August 2021 due to installation of the new COMPASS Upgrade tokamak [7, 8].

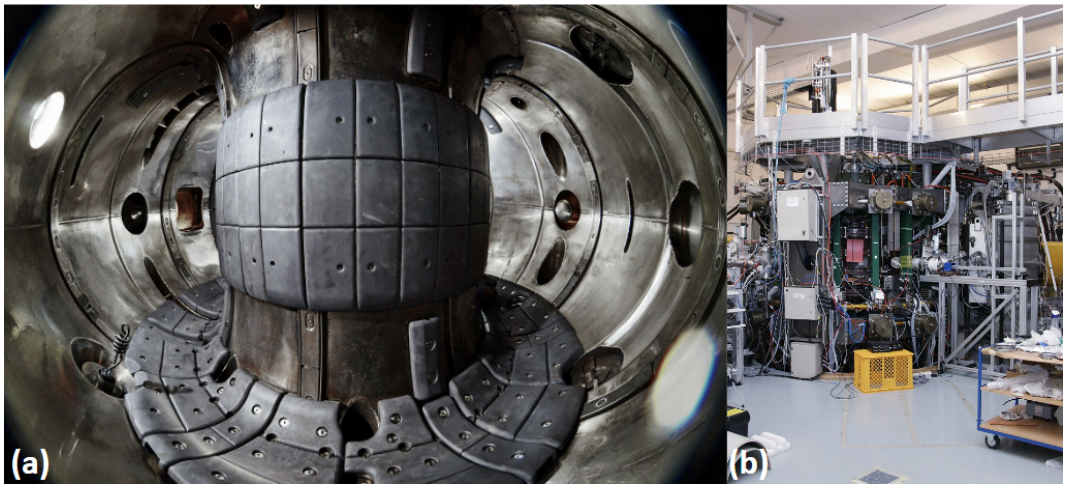

Figure 1.6: Photograph of the inside of the COMPASS vacuum vessel (a) and the experimental hall (b).

The COMPASS tokamak has a compact vacuum vessel with size and shape

relevant to ITER plasmas (one tenth smaller in the linear scale as shown in Figure 1.7). The typical machine parameters are listed in Table 1.1. The vessel is divided into 16 sectors according to the number of toroidal field coils. The COMPASS tokamak is equipped with a graphite divertor located in the bottom part of the vacuum vessel. Circular, elliptic and single-null diverted (SND) plasma shapes are available for operation. HFS wall of the vacuum vessel is covered with limiter graphite tiles. A number of tiles is also distributed in the top part of the vacuum vessel. Dozens of ports in the HFL, LFS, top and bottom enable good plasma coverage by the diagnostics. The working gases are hydrogen, deuterium and helium. Nitrogen and argon can be used as impurity seeding. Standard directions of the plasma current I_p and toroidal field B_t are counter-clockwise when looking from the top of the vacuum vessel. In addition to this, independent reversal of I_p and B_t directions is possible. Wall conditioning is ensured by helium glow discharges between the experimental sessions as well as periodic baking of the vacuum vessel at 150 °C as well as boronization [9]. Auxiliary heating is performed by two NBI beams, capable of operating in co- and counter- I_p direction. An improved energy confinement regime (H-mode) was first achieved in 2012 and is regularly used in experimental campaigns (both in ohmic and NBI-assisted discharges). Plasma equilibrium reconstruction is obtained by EFIT code, which uses magnetic diagnostics data to solve equilibrium force-balance (Grad-Shafranov equation).

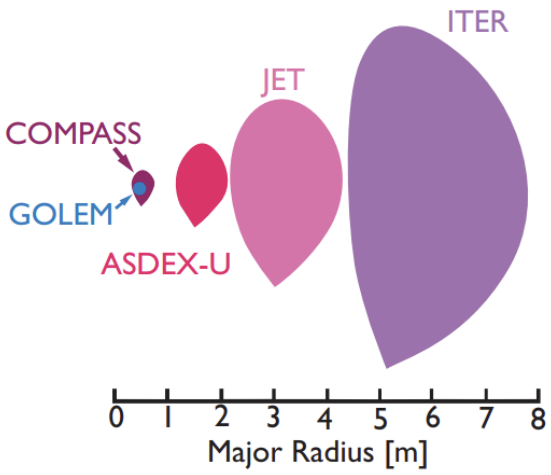

Figure 1.7: COMPASS vacuum vessel scale compared to other European machines with ITER-relevant vacuum vessel shapes. GOLEM tokamak (formerly operated at IPP) is added for scale. (Figure from [10]).

The plasma current at COMPASS is generated by 16 copper toroidal field coils (TF), which are equidistantly distributed toroidally. Poloidal field coils (PF) are used for plasma positioning and control (Figure 1.8). They are arranged into the following independent circuits:

- Magnetising Field Power Supply (MFPS): used to generate and ohmically sustain the plasma current.
- Shaping Fields Power Supply (SFPS): used to modify plasma shape and create divertor configuration.

- Equilibrium Field Power Supply (EFPS): used to control vertical position of the plasma and to prevent plasma expansion due to $\mathbf{E} \times \mathbf{B}$ force.
- Radial (horizontal) magnetic field (BR): used to control vertical position of the plasma.
- Vertical magnetic field (BV): used to control radial position of the plasma.

Quantity	Value
Major torus radius R	0.56 m
Minor torus radius a	0.23 m
Total plasma current I_P	$<$ 350 kA
Toroidal magnetic field B_t	$<$ 2.1 T (typically up to 1.15 T)
Flat-top duration	up to $\sim$ 200 ms
Elongation κ	1-1.8
Upper triangularity	0.3
NBI beam heating P_{NBI} 40 keV	2×0.350 MW
Line integrated density	$1.2 \times 10^{20} m^{-3}$ for B_t=1 T
Vacuum pressure	$1 \times 10^{-6} Pa$ s
Vessel material	Inconel 625
Vessel wall thickness	3 mm
Divertor material	graphite

Table 1.1: COMPASS parameters

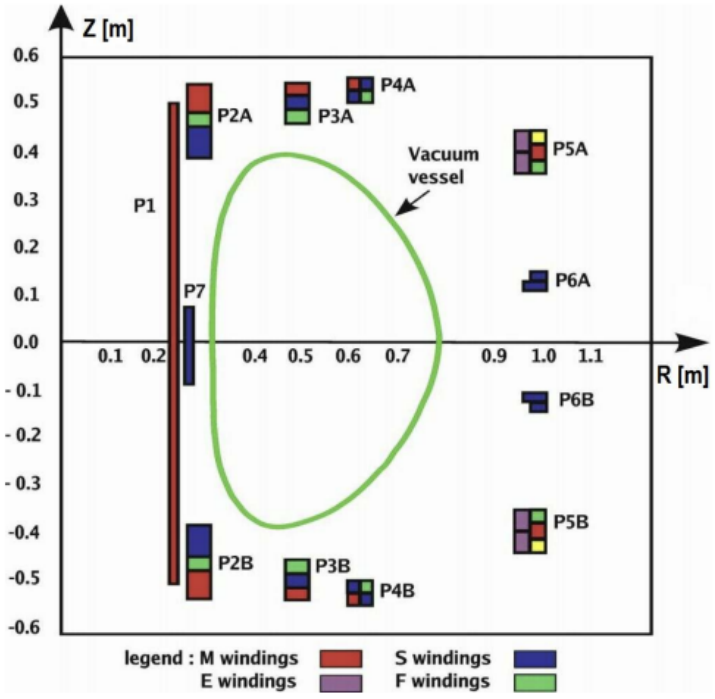

Figure 1.8: Configuration of PF coils at the COMPASS tokamak (Figure from [11]).

The COMPASS tokamak is equipped with a comprehensive set of diagnostics [12], which includes:

- Magnetic diagnostics (internal and external full Rogowski coils, Mirnov coils and partial Rogowski coils, diamagnetic loop), which will be further described in 3.1.
- Microwave diagnostics (2-mm interferometer, ECE and EBW radiometer, microwave reflectometer).
- Spectroscopic diagnostics (Thomson scattering, fast VIS cameras, multichannel optical system for VIS radiation measurement, fast bolometry, SXR monitoring, plasma rotation measurement).
- Beam and particle diagnostics (beam emission spectroscopy, atomic beam probe, neutral particle analyser).
- Probe diagnostics (divertor probes, reciprocating probes).

The research covers various topics including H-mode, disruptions, pedestal physics, ELMs, transport in the edge plasma and SOL, physics of runaway electrons and many more. As the COMPASS tokamak is a relatively small machine having moderate I_p magnitudes and heat loads, there is no need for disruption avoidance or mitigation strategy. Disruptions do not pose a significant threat to the COMPASS vacuum vessel, allowing accumulation of a large set of disruptive discharges both unintentional and planned.

2. Disruptions

2.1 Basic principles

Disruption is an abrupt degradation of magnetic confinement resulting in a discharge termination. It might prevent sustainable operation of the large tokamak devices due to enormous thermal and electromagnetic (EM) loads following the event. Addressing a problem of disruption plays a critical role in future machines design and requires profound understanding of the underlying physical processes.

Disruption starts with a precursor phase, which triggers an MHD instability followed by the edge cooling. In order to keep the total toroidal plasma current intact an unstable plasma current density profile develops with a steep gradient around q=2 rational surface and flat region in the plasma centre. This initiates growth of macroscopic instabilities such as magnetic islands. The instability progresses leading to stochastization of magnetic field lines and subsequent enhancement of perpendicular heat diffusivity. This phase is called thermal quench (TQ) and it causes loss of thermal energy and temperature on a very short timescale. Thermal quench is often accompanied by a characteristic spike of the plasma current, appearing due to conservation of magnetic helicity after the current profile flattening. In the final phase of the disruption temperature drop leads to resistivity increase and subsequent rapid decrease of the plasma current (current quench - CQ). Loop voltage cannot be sufficiently increased by the present tokamak transformers. Therefore, the entire plasma current drops to zero. Disruption is accompanied by plasma displacement towards the vacuum vessel wall. The case of simultaneous movement and loss of plasma current is called major disruption [13]. In elongated plasma fast loss of vertical stability might result in the plasma column reaching the wall with full thermal energy and plasma current. This type of disruptions is called vertical displacement event (VDE). It can happen that only a fraction of thermal energy is lost during TQ and plasma can survive without full loss of the plasma current. Such a case is referred to as a minor disruption [14].

The initiating event triggering a disruption might be of various nature, e.g. H-L transition, giant ELM, mechanical failures etc [15]. However, they all result in a disruption precursor such as shape or position control loss, impurity influx leading to violation of the tokamak operational limits, beyond which large MHD instabilities are developed and plasma edge cools down. The following limits determine tokamak operational space:

1. Troyon beta limit. Plasma performance can be evaluated by the ratio of the plasma pressure to magnetic pressure $\beta = \frac{\langle p \rangle}{p_{mag}} = \frac{nk_BT}{B^2/(2\mu_0)}$. Beta must be maximised for effective plasma confinement as fusion power increases quadratically with plasma pressure $P_{Fusion} \propto \langle p^2 \rangle V \propto \beta^2 B^4 V$, but pressure-driven instabilities develop (e.g. ballooning mode) if β exceeds the following limit: $\beta_{max}[\%] = \frac{\beta_N I_p}{aB_0}$ where $\beta_N = 2.8$ (determined numerically).

2. Plasma current limit (Kruskal–Shafranov limit). At a given toroidal magnetic field plasma current maximum magnitude is limited due to development of kink instability (displacement of plasma column cross-section). The kink instability forms if its characteristic wavelength is longer than the tokamak major radius.

Therefore, the stability criterion is $L = \frac{2\pi a B_t}{Bp} > 2\pi R$ which implies limitation of the plasma current via safety factor:

$$\begin{aligned} q &= \frac{aB_t}{RB_p} \\ L = 2\pi qR > 2\pi R &\longrightarrow q > 1 \\ I_p &= \frac{2\pi a B_p}{\mu_0} \\ q &= \frac{2\pi a^2 B_t}{I_p \mu_0 R} > 1 \\ I_p &< \frac{2\pi a^2 B_t}{\mu_0 R} \end{aligned} \tag{2.1}$$

The limit $q > 1$ is a necessary, but not a sufficient condition and typically $q > 2$ is required for stable operation.

3. Greenwald density limit. Increase of electron density beyond Greenwald limit $n_G = \frac{I_p}{2\pi a^2}$ leads to radiative collapse. Plasma radiated power includes bremsstrahlung, electron cyclotron and line radiation. The latter becomes dominant as a result of density growth and subsequent excessive edge cooling.

Disruption triggers are widely studied in order to develop disruption prediction techniques as well as mitigation strategies. Modelling and statistical analysis are commonly used and are described in [16, 17, 18].

A major reason for investigating disruption phenomenon is its hazardous effect on the vacuum vessel and in-vessel components. Sudden release of large thermal energy pose a high risk of damage for PFCs. This is a particular concern for larger machines as the stored energy scales as R^5 major radius. At JET and ITER it reaches ∼10 MJ and ∼350 MJ respectively [19]. The thermal load might also be very localized.

An additional damage to the PFCs is caused by formation of runaway electrons (RE). They are produced during CQ phase due to an induced toroidal electric field larger than the critical value. Then electrons with high energy will not be slowed down by friction force and they will be accelerated by an electric field. In case of ITER, it is expected that up to 70% of the plasma current can be converted to RE.

A number of mitigation and prevention techniques can be applied in order to prevent vacuum vessel and in-vessel components damage. These methods require:

- Reliable plasma position control.
- Redistribution of the thermal energy during TQ.
- Control over plasma current profile during CQ.
- Prevention of an excessive RE generation.

2.2 Electromagnetic loads on the vacuum vessel

Vertical displacement of the plasma, the rapid change of the plasma current and its flow into the vacuum vessel wall during disruption result in large currents

flowing in the vacuum vessel and in-vessel conducting components. When coupled with the magnetic fields this currents result in forces acting on the vacuum vessel, which can lead to the damage of the vessel and in-vessel components:

$$\mathbf{F} = \mathbf{J_{tor}} \times \mathbf{B_{pol}} + \mathbf{J_{pol}} \times \mathbf{B_{tor}} + \mathbf{J_{pol}} \times \mathbf{B_{pol}} \tag{2.2}$$

where J_{tor} and J_{pol} are toroidal and poloidal current densities in the vacuum vessel. Note that poloidal vessel current and poloidal magnetic field are not necessarily parallel and also contribute to the total force. The vessel currents can be classified as follows:

- The currents induced by the displacement of the plasma column, i.e. the stabilizing wall eddy currents (flow in toroidal direction).
- The currents induced by TQ, i.e. the net poloidal eddy current.
- The currents induced by CQ, i.e. the net poloidal and toroidal eddy currents.
- Halo currents: occur during CQ, flow along the open magnetic field lines when in plasma and along the least resistance path in the vacuum vessel.

Schematic representation of the vessel currents distribution is shown in Figure 2.1.

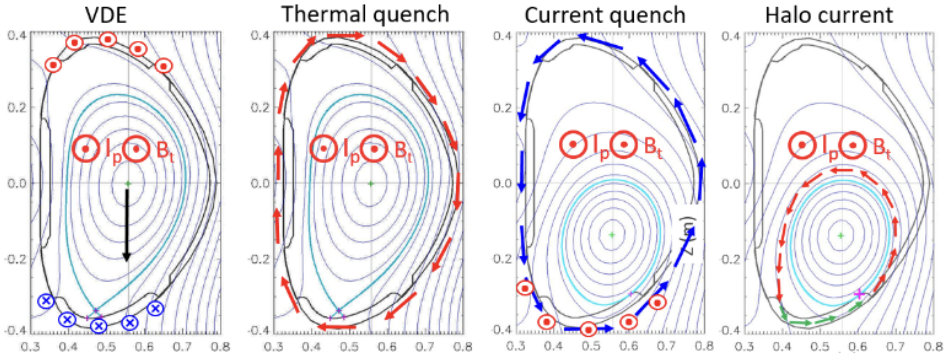

Figure 2.1: Current in the vacuum vessel: vertical displacement of the plasma column (labelled as VDE) - currents flowing toroidally in the opposite direction in the top and bottom part of the vacuum vessel in order to stabilize the motion of the plasma column; thermal quench - currents flowing poloidally, having symmetric distribution over the vacuum vessel cross-section; current quench - poloidal and toroidal induced currents, toroidal currents are more dense in the area closer to the plasma column; halo current flows along the open magnetic field lines in the plasma (red arrows) and closing its circuit poloidally in the vessel (green arrows).

The various contributions to the total force acting on the vacuum vessel has been considered in a number of equilibrium codes such as TSC, DINA, and CarMa0NL. The approaches include self-consistent solution of the plasma evolution (DINA [20], TSC [21] and CarMa0NL [22]) as well as engineering approach focusing on the maximum envelope of possible forces (COMPASS-U [23], NSTX-U

[24]). The forces can be also measured indirectly, e.g. by detecting displacement of the vacuum vessel as it is done at JET [25, 26].

The stabilizing wall eddy currents

It was shown that higher elongation and triangularity are preferable to obtain higher β [27, 28]. However, elongated plasmas is inheritably unstable to vertical displacement ([29], p.400). This is due to poloidal field coils being used to obtain elongated configuration. Each coil has the current flowing in the co-I_p direction, hence producing forces that attract plasma towards the top and bottom part of the vacuum vessel (as illustrated in Figure 2.2). The force acting on the plasma is proportional to the distance between the plasma column and the coil. Therefore, a small displacement leads to imbalance of the forces, pulling plasma further away from the stationary position. On the timescales comparable to the resistive diffusion time of the vacuum vessel the vertical displacement can be stabilized by the currents induced in the conductors around the plasma (including the vessel) or by additional stabilizing systems. However, vertical stabilization system might not react fast enough leading to uncontrolled vertical movement of the plasma towards the wall. This phenomenon is called vertical displacement event (VDE) [30]. The initial vertical displacement can be triggered by TQ due to rapid flattening of the plasma current profile (as shown in [31]). In addition to this, the asymmetry of the vacuum vessel and the presence of the divertor can contribute to the dragging effect, since they affect the eddy currents distribution.

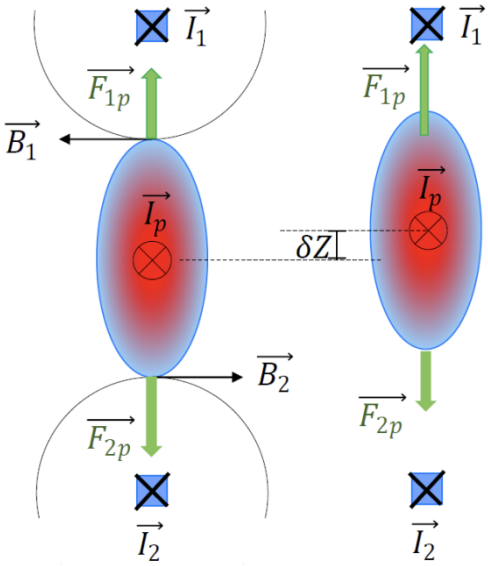

Figure 2.2: Schematic illustration of the vertical instability of the plasma column. Left: stable plasma elongated by the poloidal field coils. Right: plasma displaced by δZ towards the top part of the vacuum vessel. (Figure from [32])

According to Faraday's law the stabilizing wall eddy currents are induced in the surrounding conducting structures to prevent the vertical displacement of the plasma column. They have dipole structure, meaning that in case of downward plasma displacement the stabilizing wall eddy current flows in the counter-I_p direction in the bottom part of the vacuum vessel, and in co-I_p direction in the top. Similarly, upward plasma displacement induces counter-I_p stabilizing wall eddy currents in the top part of the vacuum vessel, and co-I_p currents in the

bottom part. These currents are routinely taken into account in plasma position feedback control systems. Plasma interaction with the passive conductors (e.g. vacuum vessel) and control coils is often described by a lumped element circuit model [33, 34, 35, 36, 37, 38, 39], which in general can be written as:

$$\mathbf{M} \cdot \dot{\mathbf{I}} + \mathbf{R} \cdot \mathbf{I} = \mathbf{V} \tag{2.3}$$

where $\mathbf{M}$ is a matrix of mutual inductances between the circuits, $\mathbf{R}$ - matrix of resistances, $\mathbf{V}$ - vector of externally applied voltage and $\mathbf{I}$ - the circuit current. For passive conductors V=0 and Equation 2.3 for the stabilizing wall eddy currents takes the following form [40]:

$$M_{VV}\dot{I}_V + R_V I_V + M_{VC}\dot{I}_C + M_{VP}\dot{I}_p = 0 \tag{2.4}$$

where M_{VV}, M_{VC} and M_{VP} are self-inductance of the passive conductor (i.e. the vacuum vessel), mutual inductance between the vessel and the control coils and mutual inductance between the vessel and the plasma, respectively; R_V is the resistance of the passive conductor; I_V, I_C and I_p are the currents in the passive conductor, control coils and the plasma, respectively. This circuit Equation 2.4 is coupled with the momentum balance of the plasma:

$$m_p \frac{d^2 z}{dt} = F_z(z) - F_{eddy} \tag{2.5}$$

In Equation 2.5 $F_z(z)$ is the destabilizing force from equilibrium field arising due to small vertical displacement z of the plasma [41]:

$$F_z(z) = I_p 2\pi R \frac{dB_R}{dz} z \tag{2.6}$$

The second term F_{eddy} is the force produced by the stabilizing wall eddy currents:

$$F_{eddy} = I_p I_V \frac{\partial M_{VP}}{\partial z} \tag{2.7}$$

where M_{VP} is the mutual inductance between the plasma and the conducting structures. Plasma inertia term $m_p \frac{d^2 z}{dt}$ is often considered negligible as it plays role on a timescale shorter than the time of plasma stabilization. Possible consequences of such an approximation are discussed in [42]. In addition to this, the lumped element circuit model assumes uniform rigid vertical displacement of the plasma and conservation of the plasma current. The plasma current in equation 2.4 can be represented as a single filament as well as an array of filaments.

Current quench eddy current

Another contribution to toroidal eddy currents is caused by the CQ and related rapid change of poloidal flux. The associated forces are greater in case when the vertically displaced plasma reaches the wall before the TQ occurrence (hot VDE). In case of hot VDE events TQ is initiated by the plasma-wall contact and subsequent destruction of the magnetic flux surfaces.

Net poloidal eddy current

Net poloidal eddy current arises due to the fast change of the toroidal magnetic flux during TQ (due to diamagnetic flux quench) as well as CQ (due to poloidal

component of I_p quench). Both contributions can be described by the model proposed in [43]:

$$\Delta\Phi \approx \frac{2\kappa}{1+\kappa^2}\frac{(\mu_0 I_p)^2}{2\pi B_0}(1-\beta_p) \tag{2.8}$$

where $\Delta\Phi$ is the flux change, κ is the plasma elongation, B_0 is the external toroidal magnetic field. $\Delta\Phi$ increases during TQ when $\beta_p < 0$ and plasma loses its diamagnetism. On the other hand, during CQ $\Delta\Phi$ decreases together with I_p loss. The model is based on electromagnetic equation for the poloidal current in the vessel and the conservation of the toroidal flux (as Equation 24 in [43] or similarly to 2.4):

$$L_w\frac{dI_{eddy}}{dt} + \frac{d}{dt}\Delta\Phi + R_w I_{eddy} + L_w\frac{dI_c}{dt} = 0 \tag{2.9}$$

where L_w and R_w are the poloidal inductance and resistance of the vessel wall, I_c is the poloidal current in toroidal control coils. The model exploits an assumption that the plasma and the wall act as ideal conductors. Therefore, the last two terms of the equation 2.9 vanish. In addition to this, the axisymmetric plasma is considered. This allows direct relation of the net poloidal eddy current to the flux change through β_p and I_p. The force contribution due to the net poloidal eddy current has been considered in a number of simulations including MAXFEA and CarMa0NL analysis for IGNITOR [44], DINA, TSC and CarMa0NL for EAST [45], JT60-SA [46], ITER [47], COMPASS-U [23].

Halo current

Shrinkage of the plasma column cross-section and I_p decay result in currents flowing in the SOL region. They are called halo currents and are considered to be one of the major sources of the forces acting on the vacuum vessel. In SOL region plasma is no longer confined, the temperature and pressure significantly decrease and the plasma is considered to be force-free $\mathbf{J}\times\mathbf{B} = \nabla p \approx 0$. Therefore, halo currents flow parallel to the open magnetic field lines when in plasma [48]. As they enter the vacuum vessel their direction is not restricted by the magnetic field anymore and is determined by the least resistive path (mainly poloidally). While flowing in the wall, the halo current induces Laplace force acting on the vacuum vessel wall (poloidal halo current coupling with toroidal magnetic field). In addition to this, the halo current path from the plasma to the vacuum vessel wall plays role, e.g. the halo current flowing through the PFCs connections perpendicular to the wall also interacts with the toroidal magnetic field and induces EM loads on them.

In force-free region of the plasma the destabilizing force $\sim I_p^2$ is balanced by the halo force $\sim I_{halo}B_t$ leading to quadratic dependence of the halo current on the plasma current $I_{halo} \sim (I_p)^2/B_t$ [49]. This relation also indicates, that the direction of the halo current is determined by B_t and is not affected by I_p direction. The amount of halo current flowing in the vacuum vessel wall can be described as an integral of the halo current flow perpendicular to the wall $J_\perp^{halo}$ over the surface of the wetted area:

$$I_{halo} = \int J_\perp^{halo} dS^{in} \quad or \quad I_{halo} = \int J_\perp^{halo} dS^{out} \tag{2.10}$$

where S^{in} and S^{out} are the wall surfaces, where halo current flows inside and outside of the vacuum vessel, respectively. The first direct measurement of halo current was performed at DIII-D tokamak [50] in 1991. Special PFCs tiles equipped with Rogowski coils enabled measurement of the current flowing from the plasma to the vacuum vessel - halo current flow. Since then many tokamaks detected halo currents both directly (as a flow from plasma to the vessel) and indirectly (as a part of poloidal current in the wall). These include JET [51, 52], NSTX [53, 54], ASDEX Upgrade [55], DIII-D [56], MAST[57], TORE-SUPRA [58], JT60-U [59], EAST [60]. Halo current measurements were also performed at COMPASS-D [61] and extended with the same diagnostics after the vessel reinstallation in Prague (COMPASS [2]). Analytical description was reported in [62].

Asymmetries during disruptions

An important aspect of electromagnetic forces evaluation is possible major toroidal asymmetry of the plasma vertical displacement, which results in asymmetric currents flow in the vessel. During rapid vertical displacement and shrinkage of the poloidal cross-section of the plasma column significant drop of safety factor is often observed. This makes the plasma prone to various instabilities, e.g. kink modes. As a consequence, plasma might undergo complex 3D deformations, e.g. radial shift, vertical tilt, twist of the plasma column.

In case of n=1, m=1 kink mode the resulting asymmetry can be represented as a vertical tilt of the plasma column (Figure 2.3). This phenomenon is called asymmetric vertical displacement event (AVDE). Toroidally asymmetric plasma interacts mainly with the toroidal magnetic field, and hence induces sideway forces acting on the vacuum vessel. Note that higher modes are also possible, but their detection is a challenging task as it requires large number od sensors at different toroidal positions. Mode n=1, m=1 detection is possible with a minimum of 3 measurement points.

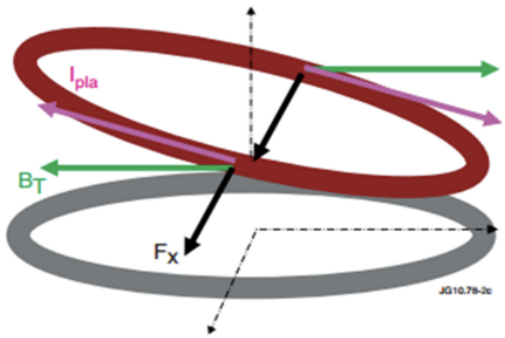

Figure 2.3: asymmetrical disruption schematic [63]

In experiments the asymmetry of the plasma column can be manifested as a non-uniform toroidal distribution of halo current or plasma current. Halo current asymmetries were reported in several tokamaks including Alcator C-Mod [64], NSTX [18], MAST [57], JET [49], ASDEX-U [55], JT-60U [65].

A typical parameter to characterize the amount of halo current is the halo current fraction (as in [66]):

$$F = \frac{I_{halo}^{max}}{I_p^{disr}} \tag{2.11}$$

where I_{halo}^{max} is the maximum value of the asymmetric halo current and I_p^{disr} is the plasma current prior to CQ. The asymmetry of the halo current is routinely described by toroidal peaking factor (TPF):

$$TPF = \frac{max(j_{halo,n})}{I_{halo}/2\pi} \tag{2.12}$$

where $j_{halo,n}$ (A/rad) is the halo current density measured at n different toroidal positions and $I_{halo} = 2\pi\frac{\sum_N^1 j_{halo,n}}{N}$. A measure of halo current asymmetry is described by the product $F \times TPF$. It has been shown that the boundary of $F \times TPF$ reaches 0.7, meaning that at TPF=1 up to 70% of I_p^{disr} can be converted to halo current (Figure 2.4).

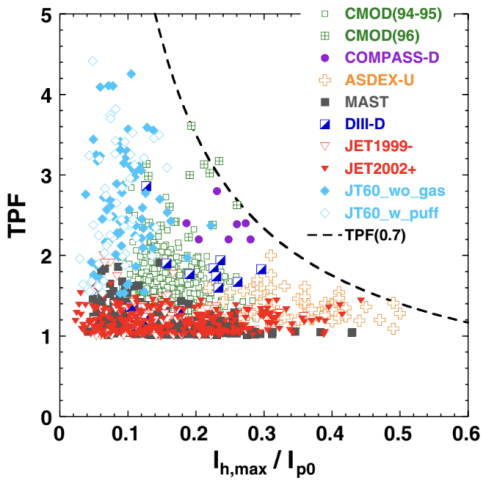

Figure 2.4: Halo current database: toroidal peaking factor with respect to halo fraction (Figure from [67])

A different approach to describe AVDE is the asymmetry of I_p measurement indicating asymmetric current flow to the vacuum vessel. This is used at JET and COMPASS [68]. An analytical model describing the relation between the sideway forces and the I_p was proposed in [69].The model considers the plasma as a rigid current filament asymmetrically displaced in the vacuum vessel and exploits vertical current moments to determine the total sideway force:

$$F_x \approx \pi I_p B_0 R_0 \alpha = \pi B_0 \Delta(I_p Z) \tag{2.13}$$

where $\Delta(I_p Z)$ is the toroidal variation of the plasma current and vertical position, R_0 - major radius of the filament, B_0 toroidal magnetic field at R_0, and $\alpha = \frac{\Delta Z}{R_0}$ is the vertical tilt of the filament.

Dynamic evolution of the plasma column asymmetry provides an additional contribution to forces during AVDE. Rotating as well as locked asymmetries were observed at JET, DIII-D, Alcator-C and others. Rotation at low frequencies might contribute to mechanical loads on the machine in case of a resonance with the natural frequencies of the vacuum vessel [70]. Asymmetrical halo currents have been considered theoretically [71]. Simulations with M3D-C1 [72, 73, 74], NIMROD [75] and JOREK [32] codes allow to include 3D geometry of the plasmas and estimate the sideway forces.

3. Disruptions at COMPASS

The COMPASS tokamak works at a wide range of plasma parameters often close to operational limits. Since the beginning of its operation many of the discharges resulted in disruptions. Since COMPASS is a relatively small device with moderate values of I_p and B_t, electromagnetic forces during disruption were never considered as a serious threat. There are neither disruption mitigation nor avoidance systems that would affect disruption occurrence. Therefore, COMPASS is a suitable device for performing dedicated disruption experiments as well as analysis of unintentional disruptions. Note that although in general disruptions at COMPASS are routine event without any detrimental consequences, several exceptional cases were reported causing damage to magnetic coils casing cover (Figure 3.1).

Figure 3.1: Magnetic coils casing damaged during a disruption.

The COMPASS disruption database was created based on the operation period 2012-2020. Statistical analysis was conducted to determine disruption rates, typical predisruptive plasma parameters and specific features of disruptions. About 60% of plasma discharges at COMPASS terminate with disruption. The disruption database has 7284 entries out of 21812 discharges stored in CDB (COMPASS database). Note that non-negligible fraction of CDB entries are faulty discharges without plasma. Disruption can occur at any stage of the discharge - ramp-up, flat-top or ramp-down. Ramp-up disruptions at COMPASS are excluded from the database by cutting the data below 1050 ms (a typical time when the flat-top is already reached after the breakdown at 950 ms and fast change of the Magnetizing Field Power Supply current). About 50% of COMPASS disruptions are happening during the flat-top, while the rest occur during the ramp-down.

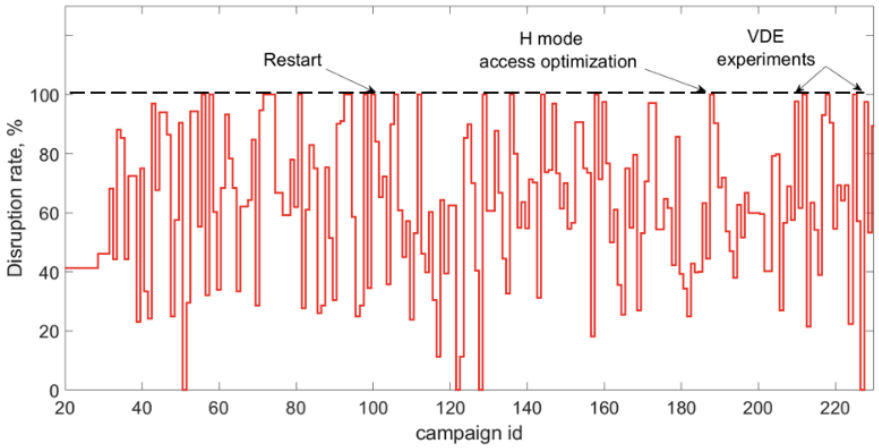

Figure 3.2: Disruption rates at different campaigns in COMPASS.

During disruptions plasma moves towards the vacuum vessel wall downward (40 %), upward (25 %) or radially to the HFS (35 %). It should be noted that HFS disruption occur mainly in circular plasma which is prone to instability of the radial position, while elongated plasma tends to be dragged up or down by PF coils.

Disruption rate is defined as the ratio between disruptive discharges to the total number of plasma discharges in a certain group. Disruption rate calculated for individual experimental campaigns is shown in Figure 3.2. It varies strongly depending on the campaign goals, required plasma parameters and wall conditions. It can be noticed, that sometimes disruption rate reaches almost 100 %. This is usually the case for the experiments prone to large MHD instabilities (e.g. H mode access optimization) or working close to the operational limits (e.g. investigation of density limit disruptions). Sometimes, a special group of experiments might require triggering of intentional VDEs. This can be achieved with the MARTe real-time plasma control system [76]. The plasma position is set to ± 10 cm (depending on the preferred upward or downward direction), which is achieved no sooner than 0.5 ms (the resistive time of the vessel). Such a displacement is comparable to the minor radius of COMPASS (0.23 m) and inevitably leads to VDE.

When operating with diverted plasma the COMPASS tokamak exhibits two types of disruptions: major disruption ($\sim$ 24%) and hot VDE ($\sim$ 76%). Representative disruptions for both cases are shown in Figure 3.3. Start of the current quench can be detected with SXR reconstruction [77]. The major disruption exhibits a characteristic I_p spike followed by CQ with simultaneous vertical movement of the plasma column. The hot VDE starts with vertical displacement and only when the plasma is reaching the vacuum vessel wall the TQ begins. Therefore, almost full plasma current and full plasma energy are deposited on the vacuum vessel, resulting in more severe thermal and electromagnetic loads.

Figure 3.4 shows plasma current I_p, plasma electron density n_e, poloidal beta β_p and edge safety factor q_{95} at the time instant 0.5 ms before CQ start. The distinct spikes around I_p of 170 kA, 230 kA and 300 kA are related to typical flat-top request values. Majority of q_{95} values are concentrated in the interval 2-6. A small number od q_{95} lower than 2 originates from RE campaigns with

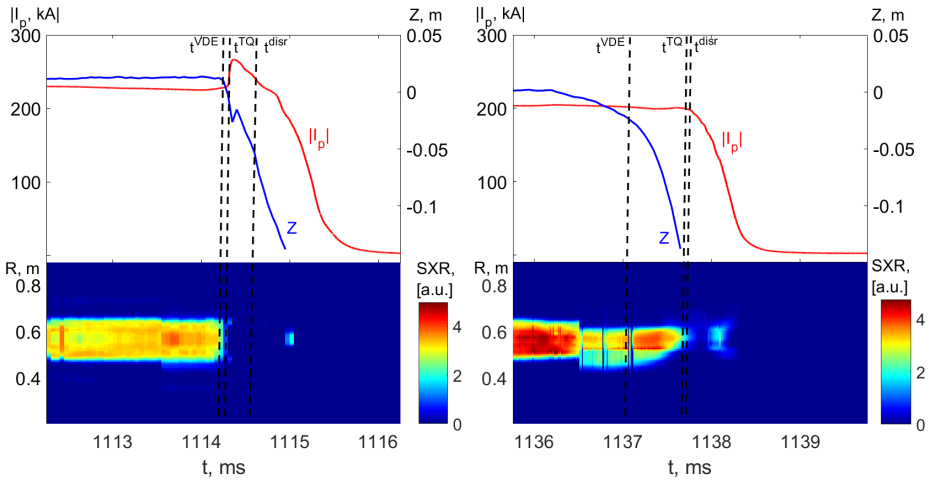

Figure 3.3: Illustration of the two types of disruptions: major disruption in discharge #15353 (left) and hot VDE in discharge #18744 (right). Top figure shows sequence of the plasma vertical movement Z (blue curve) and the plasma current I_p (red curve). Bottom figure shows SXR reconstruction, where the TQ can be seen.

ramp-down disruptions. They are often proceeded by a relatively long I_p decay and multiple I_p spikes that indicate partial loss of thermal energy.

Operational space of a tokamak can be represented by Hugill diagram [78], which describes plasma state as a function of inversed safety factor 1/q depending on $n_e R/B_t$. Operational space at COMPASS was produced by sampling of I_p, n_e, B_t, and q_{95} in 5263 discharges. A sampling period of $t_{sampling}$=0.05 ms was used in the interval where $I_p > 30kA$. In total $\sim 65 \cdot 10^6$ data entries were collected for each parameter, where 3095 samples were labelled as disruptive (closest to the start of CQ). An example of I_p sampling is shown in Figure 3.5. Note that not all of the sampling instants are depicted for better visual clarity.

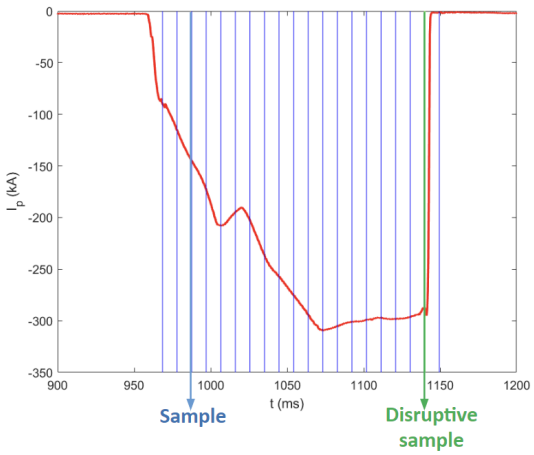

Figure 3.5: Illustration of the plasma parameters sampling (I_p in this case) for operational space assessment. Only few sampling point are depicted, while the real sampling period is $t_{sampling}$=0.05 ms. The sample closest to the current quench start (if present) is referred to as disruptive sample.

Likelihood of disruption occurrence at certain plasma parameters is described

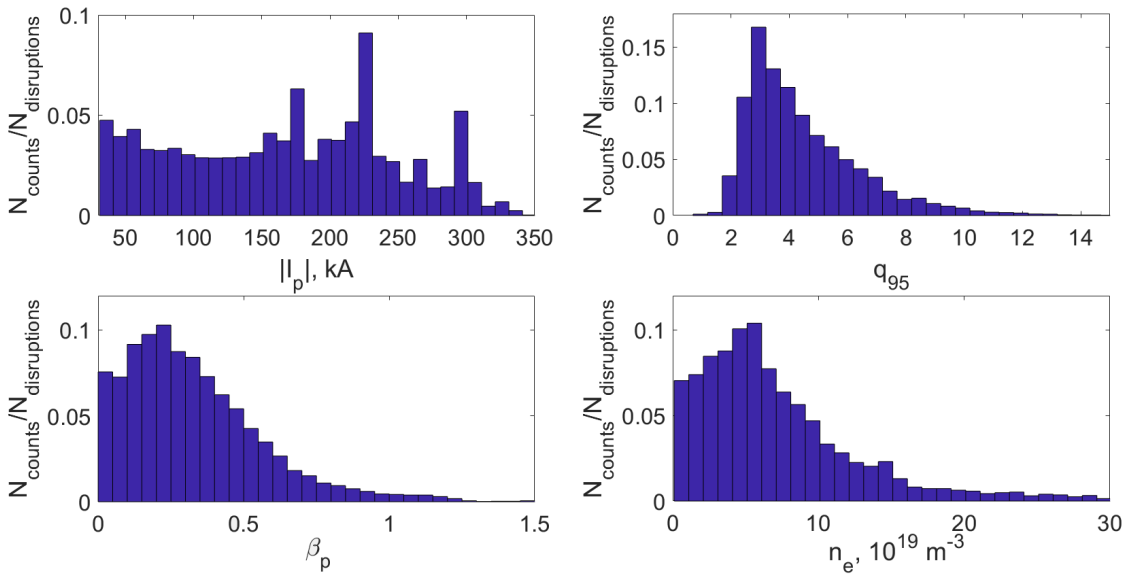

Figure 3.4: Number of occurrence of predisruptive plasma parameters in disruptive discharges. Top left: the plasma current I_p; bottom left: poloidal beta β_p; top right: the edge safety factor q_{95}; bottom right: electron density n_e.

by so-called disruptivity [79]:

$$Disruptivity = \frac{N_{samples}^{disruptive}}{N_{samples} \cdot t_{sampling}} \tag{3.1}$$

where $N_{samples}^{disruptive}$ is the number of disruptions observed in a certain plasma state and $N_{samples} \cdot t_{sampling}$ is the total plasma operation time spent in this state. Disruptivity is expressed in 1/s, while its inversed value defines the average time plasma can survive at given parameters before it disrupts. Disruptivity dependence on I_p is depicted in Figure 3.6. It can be seen that disruptivity tend to increase at larger $|I_p|$. In addition to this, pronounced spikes are observed around 170 kA, 230 kA and 300 kA both in the count of samples as well as in disruptivity. It should be noted that these are typical request parameters during COMPASS operation. Some of this discharges had a programmed disruption. In addition to this, disruptivity tends to be lower at the parameters where plasma rarely operates. This is explained by a lack of statistical points.

Disruptivity dependence on n_e is shown in Figure 3.7. Upper bound of the Greenwald density limit can be estimated as $n_G = \frac{I_p}{\pi a^2} = \frac{0.4MA}{\pi(0.23m)^2} = 24 \cdot 10^{19} m^{-3}$. It is clear that disruptivity growth when the density is approaching n_G.

Disruptivity dependence on q_{95} is shown in Figure 3.8. The highest disruptivity is observed close to $q_{95} = 2$ as expected from the plasma current operational limit.

Overall operational range is shown by Hugill diagram (Figure 3.9, top), which can be as well used for disruptivity representation (Figure 3.9, bottom). The diagram allows clear indication of density and plasma current operational limits. The majority of the sampled data points lie within the indicated limit, although operation close to the limits is seldom observed. Visibly less data is depicted

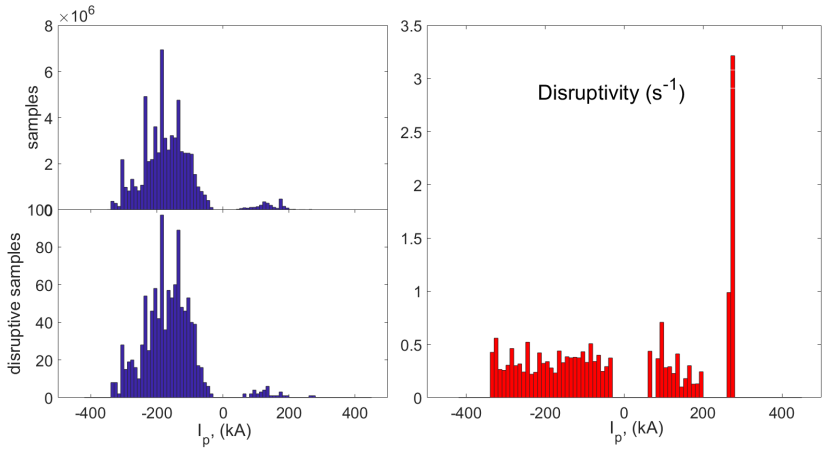

Figure 3.6: Disruptivity with respect to the plasma current I_p

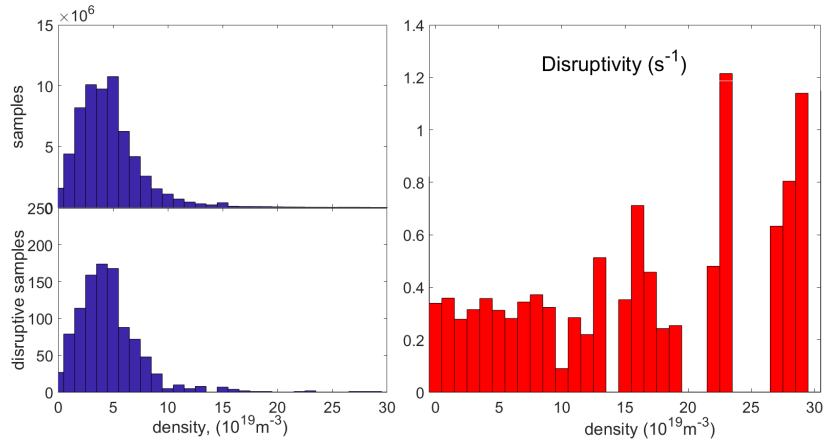

Figure 3.7: Disruptivity with respect to the plasma density n_e

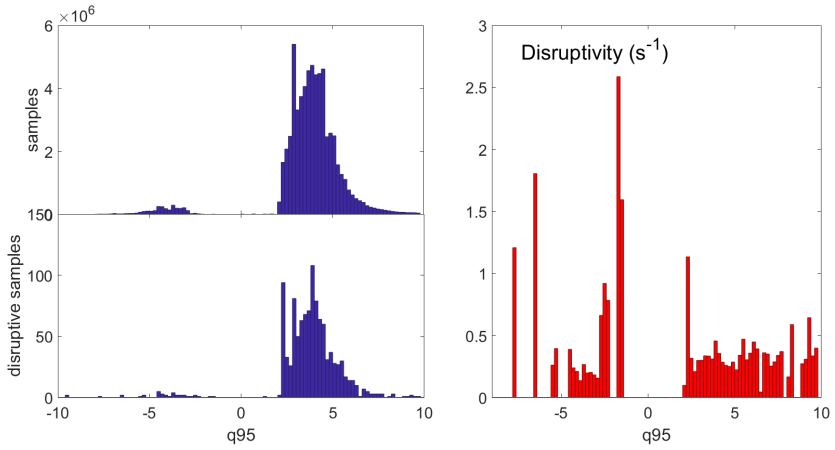

Figure 3.8: Disruptivity with respect to the safety factor q_{95}

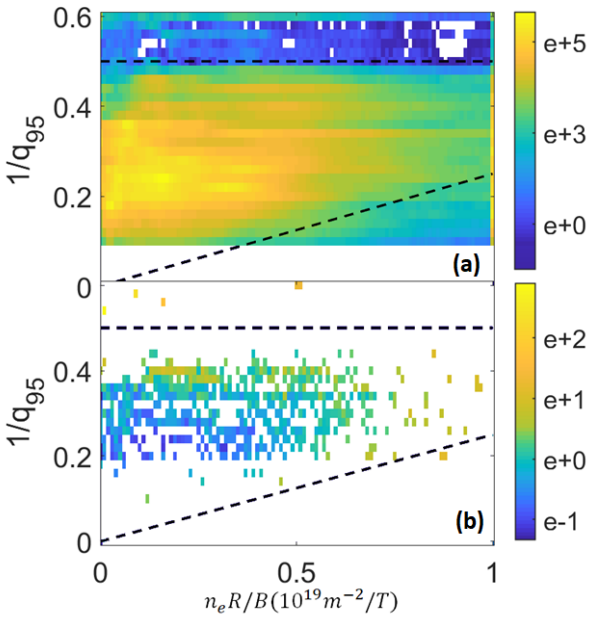

Figure 3.9: Hugill diagram for the plasma operational space (top) and disruptivity (bottom). Logarithmic scale is used. 5263 discharges with 3095 disruptions are taken used in the database. Plasma current limit and Greenwald density limit are marked by dotted lines.

in the disruptivity diagram. Only disruptive samples can be seen here. The disruptivity tend to increase towards the plasma current limit, although no clear dependence is observed closer to Greenwald limit.

Previous research of disruptions at the COMPASS tokamak includes studies of the plasma current asymmetries [68], locked mode as a disruption precursor [16], density limit disruptions [80], halo current density limitation [81, 82], Recently a manuscript on plasma current and vessel current characterization was accepted for publication [2] and is attached to this thesis.

3.1 Magnetic diagnostics

Magnetic diagnostics is essential for tokamak operation as well as for physics studies. It is used to determine the key plasma parameters such as the plasma current, radial and vertical positions, magnetic energy and many others [83]. It is involved in equilibrium reconstruction, MHD modes detection, feedback control. In addition to this, magnetic diagnostics is frequently used for disruptions studies as it can provide information about local vessel currents as well as major toroidal asymmetries of the plasma column.

The COMPASS tokamak is equipped with a comprehensive set of magnetic diagnostic (Figure 3.10) allowing measurement of the plasma current in 5 toroidal positions, detection of local poloidal vessel currents as well as local toroidal vessel current densities. The magnetic diagnostics include:

- Full internal Rogowski coil
- Full external Rogowski coil

- Internal partial Rogowski coils (IPRs): 16 coils evenly covering the poloidal cross-section of the vacuum vessel
- External partial Rogowski coils (EPRs): 16 coils evenly covering the poloidal cross-section of the vacuum vessel
- Toroidal, poloidal and radial Mirnov coils (MC): 3 toroidal positions, 24 coils each, evenly covering the poloidal cross-section of the vacuum vessel.

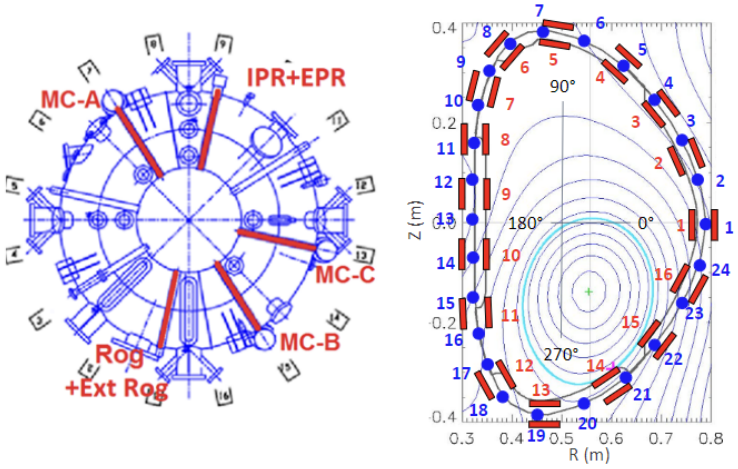

Figure 3.10: Distribution of magnetic diagnostics in toroidal direction (left figure) and in poloidal cross-section (right figure). Full Rogowski coils is labelled as 'Rog'; external full Rogowski coil - 'Ext Rog'; Mirnov coils Rings A, B and C - 'MC-A', 'MC-B' and 'MC-C', respectively; Internal Partial Rogowski coils and External Partial Rogowski coils - 'IPR' and 'EPR'. IPR and EPR coils pairs are depicted by red rectangles and Mirnov coils are shown as blue dots.

3.1.1 Full internal and external Rogowski coils

Rogowski coils are routinely used in tokamaks in order to measure plasma current [84]. It comprised a helical solenoid encircling the current of interest (e.g. plasma) with a return center wire (to eliminate possible contribution from the surrounding fields). The working principle of the coil is based on Ampere's and Faraday's laws. The plasma current generates poloidal magnetic field:

$$\oint_l B_p dl = \mu_0 I_p \tag{3.2}$$

where the integration is performed over the path poloidally encircling the plasma (Rogowski coil contour). The change of magnetic flux induces voltage, which allows to determine I_p after integration:

$$\begin{aligned} \Phi &= n \int_S dS \oint_l B_p dl = nS\mu_0 I_p \\ U &= -\frac{d\Phi}{dt} = -\mu_0 nS \frac{dI_p}{dt} \end{aligned} \tag{3.3}$$

where n is the uniform winding density per unit length, S - is the area of a single winding. Rogowski coil for I_p at COMPASS is mounted inside of the vacuum

Magnetic coil	R [mm]	Z [mm]	angle [deg]
IPR 1	788.50	0.00	90.000000
IPR 2	756.30	131.70	113.650000
IPR 3	685.00	249.50	128.992210
IPR 4	584.90	342.50	148.008500
IPR 5	457.40	382.90	180.000000
IPR 6	372.60	331.30	241.985290
IPR 7	333.40	226.60	258.330530
IPR 8	324.00	115.50	270.000000
IPR 9	324.00	0.00	270.000000
IPR 10	324.00	-115.50	270.000000
IPR 11	333.40	-226.60	281.669470
IPR 12	372.60	-331.30	298.014710
IPR 13	457.40	-382.90	0.000000
IPR 14	584.90	-342.50	31.991499
IPR 15	685.00	-249.50	51.007794
IPR 16	756.30	-131.70	66.350000

Table 3.1: IPR coils positions. The angle is measured from a vector pointing to the LFS, positive values correspond to the counter-clockwise direction.

vessel and consists of a single continuous segment, hence in this manuscript it is referred to as full internal Rogowski coil. The coil encircles the plasma column and allows to directly deduce I_p magnitude. Another full Rogowski coil is located on the outside of the vacuum vessel at the same toroidal position as the full internal Rogowski coil. This coil is called full external Rogowski coil and it encircles the plasma current together with the net toroidal currents flowing in the vacuum vessel. Both internal and external full Rogowski coils use analogue integration and are connected to ATCA data acquisition system [85]. The data is sampled with 2 MS/s, 16 bit resolution. The main purpose of internal and external full Rogowski coils is measurement of the plasma current and total toroidal net vessel current.

3.1.2 Internal and external partial Rogowski coils

Similarly to full Rogowski coil, a discrete pick-up coil can be used to measure local variations of magnetic flux. At COMPASS these coils are positioned both inside and outside of the vacuum vessel wall, making pairs evenly distributed over the poloidal cross-section as shown in Figure 3.10. They are oriented parallel to the poloidal cross-section of the vessel, hence measuring mainly poloidal flux:

$$\Phi = NSB_p \tag{3.4}$$

where N is the number of turns in the coil, S is the cross-sectional area of the coil and B_p is the magnetic field component along the probe axis. The exact coils position and orientation are listed in 3.1.

These coils are referred to as internal and external partial Rogowski coils - IPR and EPR, respectively. Note that EPR coils will detect the magnetic flux change induced both by plasma and toroidal currents flowing in the vacuum vessel. IPR

coils have a core of 4 cm length, 8.25 mm × 25 mm cross-section with R=2 mm round corners. The wire of 0.4 mm diameter takes 161 turns of the windings mounted in 2 layers, forming 347 cm^2 effective area. EPR coils are larger (10 cm) and are slightly curved. All IPR coils are connected to ATCA1, while EPRs use Nimbus data acquisition systems. In both cases the data is sampled with 2 MS/s, 16 bit resolution. The main purpose of IPR is real time position control and EFIT reconstruction. They also enable calculation of the plasma current. Combination of EPR and IPR coils allows determination of local toroidal vessel currents.

3.1.3 Mirnov coils

So-called Mirnov coils are similar to partial Rogowski coils, but their length is comparable to the diameter. A total of 216 coils are installed in COMPASS. They are arranged in 3 array (labelled as Ring A, B and C) at different toroidal positions. Each toroidal position has 3D coils distributed evenly at 24 poloidal angles. Therefore, each location (blue dots in Figure 3.10) correspond to 3 coils measuring toroidal, poloidal and radial fields. The coils have effective area S=17.977 cm^2 and are wound on a cylindrical core of 5 mm length and 4.7 mm diameter. The coils' exact positions are listed in Table 3.2. The coils are mounted in a metallic casing (Figure). The coils are connected to Nimbus and ATCA4 data acquisition systems. Only poloidal Mirnov coils in Ring B have analogue integrators, the rest are integrated numerically. Toroidal Mirnov coils allow determination of local poloidal vessel currents. Poloidal Mirnov coils can be used for the plasma current reconstruction.

Care should be taken when processing Mirnov coils data as their measurements might be affected by neighbouring PFCs as well as the casing holding the coil. Any conducting element between the plasma and the coils might lead to parasitic signal. The positioning of the coils in the vacuum vessel is shown in Figure 3.11. On the bottom part of the vessel they are covered by divertor plates inside a groove in a metal backplate. On the HFS the coils are located in the gaps between the PFCs, there are no continuous conducting structures between the coils and the plasma. On the top part of the vacuum vessel the coils casing is directly exhibited to the plasma. The divertor backplate might corrupt toroidal Mirnov coils measurements. The stainless steel backplate is ∼10 mm sick and has resistivity $6.9 \cdot 10^{-7} \Omega \cdot m$, while the vacuum vessel made of Inconel 625 is only 3 mm thick and has resistivity almost twice as high $12.9 \cdot 10^{-7} \Omega \cdot m$. Therefore, the backplate is a more favorable electrical path for the halo current entering the divertor compared to the vacuum vessel.

Another difficulty is related to the damage of the coils casings. The original design comprises magnetic coils covered by a metal strip that has no electric contact to the sides of the casing, hence no parasitic current can flow in front of the coil. However, the cover was damaged in several places due to exceptionally excessive electromagnetic loads during disruption. It was repaired by putting a 0.5 mm thick metal patch on top of the casing creating unwanted electrical connection (Figures 3.12 and 3.13). Part of the vessel current might flow through the patch instead of the vacuum vessel wall (which is 3 mm thick).

Mirnov coil #	ϕ		θ		R	
	R [mm]	**Z [mm]**	**R [mm]**	**Z [mm]**	**R [mm]**	**Z [mm]**
1	789.2	9.5	789.2	0	791.2	-9.5
2	769.9	98	772.9	89	777.7	80.6
3	736.8	171.7	741.1	163.2	747.2	155.7
4	678.7	257.5	684.5	250	691.9	243.8
5	614.2	322.4	621.3	316	629.7	311.2
6	535.9	367.3	544.7	363.7	554.2	361.9
7	448	384.8	457.5	384.5	467	386.3
8	386.1	353.3	393.4	359.4	399.3	367.1
9	351.7	289.3	355.3	298.1	357	307.6
10	331.6	217.2	333.6	226.5	333.5	236.2
11	325.1	161.7	324.9	152.2	322.6	142.7
12	324.5	85.7	324.5	76.2	322.5	66.7
13	324.5	9.5	324.5	0	322.5	-9.5
14	324.5	-66.7	324.4	-76.2	322.5	-85.7
15	324.9	-142.7	325.2	-152.2	323.4	-161.7
16	331.5	-217.2	333.5	-226.5	333.5	-236.2
17	351.7	-289.3	355.3	-298.1	357	-307.6
18	386.1	-353.2	393.3	-359.4	399.2	-367.31
19	448	-384.8	457.5	-384.5	467	-386.3
20	535.1	-367	544.4	-363.1	554	-361.3
21	614	-321.3	621	-315	629.4	-310.1
22	678.7	-257.4	684.6	-250	692	-243.7
23	745.4	-154.8	741.1	-163.3	738.6	-172.6
24	775.8	-80	772.8	-89	771.8	-98.6

Table 3.2: Positions of toroidal-ϕ, poloidal-θ and radial-R Mirnov coils.

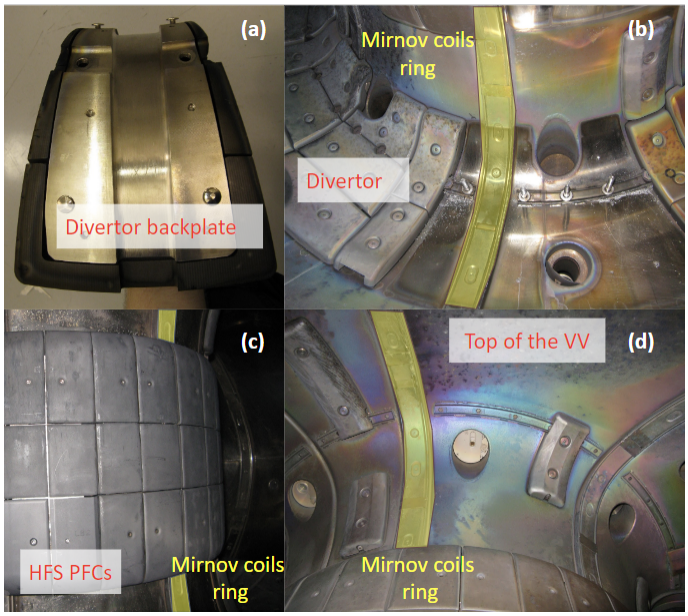

Figure 3.11: Mirnov coils casing position in the vacuum vessel with respect to surrounding PFCs.

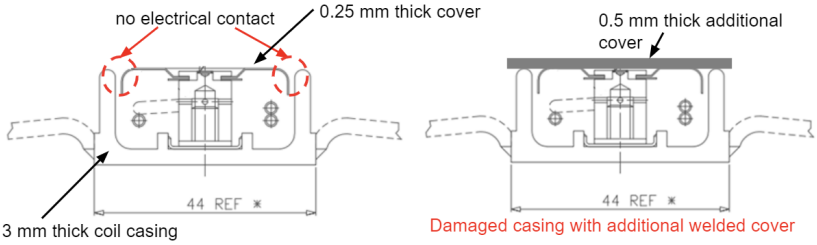

Figure 3.12: Coil casing cover: original design (left) and with metal patch on the top (right).

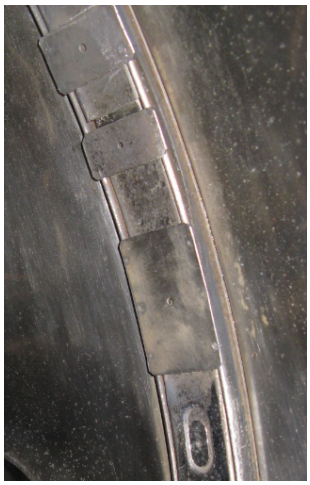

Figure 3.13: Mirnov coils casings repaired with a metal patch after being damaged during a disruption.

3.1.4 Diamagnetic loop

Diamagnetic loop detects changes in the toroidal magnetic flux related to the plasma current and pressure. The diamagnetic loop measures the difference between the total toroidal flux and unperturbed flux:

$$\Delta\Phi = \Delta\Phi_D = \Phi_{total} - \Phi_{vacuum} \approx \frac{2\kappa}{1+\kappa^2}\frac{(\mu_0 I_p)^2}{2\pi B_0}(1-\beta_p) \tag{3.5}$$

The two diamagnetic loops at COMPASS are located at the positions of toroidal field coils 5 and 11. The diamagnetic loops are used to measure plasma magnetic energy. In addition to this, net poloidal vessel current can be obtained.

3.1.5 Poloidal Mirnov coils data acquisition

Poloidal Mirnov coils at COMPASS are used for I_p reconstruction as will be described in Section 3.1.7. While Mirnov coils in Ring B have analogue integrators, the coils in Ring A and C require numerical integration. This leads to a corruption of the integrated data as indicated by a spurious offset of the signal after disruption. The reason lies in the data acquisition channels working range. The default acquisition range is set to ±10 V with resolution 0.3 mV/bit. This results in accumulation of an error during the discharge flat-top. Alternative data acquisition range ±2 V with resolution 0.06 mV/bit is available in Nimbus. However, while it improves the data quality during the flat-top it cannot cope with the large change of voltage during disruption and the signal saturates (Figure 3.14). Therefore, one has to choose between poor data quality during the discharge flattop and loss of the data during disruption. The following solution was implemented: each poloidal Mirnov coil was connected two 2 data acquisition channels (DAC) with different sensitivity (±10 V and ±2 V). The data from the two DAQ are then combined improving the signal quality during disruption. The basic combination of the channels is done in a following way:

$$\begin{aligned} S_{combined}(t) &= S_{\pm 10V}(t) if S_{\pm 2V}(t) > 1.9V \\ S_{combined}(t) &= S_{\pm 2V}(t) if S_{\pm 2V}(t) < 1.9V \end{aligned} \tag{3.6}$$

This allows to use more precise ±2 V channel, while the data is replaced by ±10 V channel at individual time instances where ±2 V channel is saturated. Care should be taken when combining the two channels with different acquisition range as they might have different filter characteristics, calibrations and offsets. The measured filter characteristics of several Nimbus channels having different acquisition ranges is shown in Figure 3.15. According to Nyquist–Shannon sampling theorem the signal has two be sampled with the frequency at least twice higher than the original signal to avoid aliasing. Nimbus collects data with 2 MHz frequency. Therefore, the filter characteristic frequencies of interest lie below 1 MHz. It can be seen in Figure 3.15 that the difference between the channels at this frequency range is $\sim 1dB$, which can be neglected when combining the two acquisition channels.

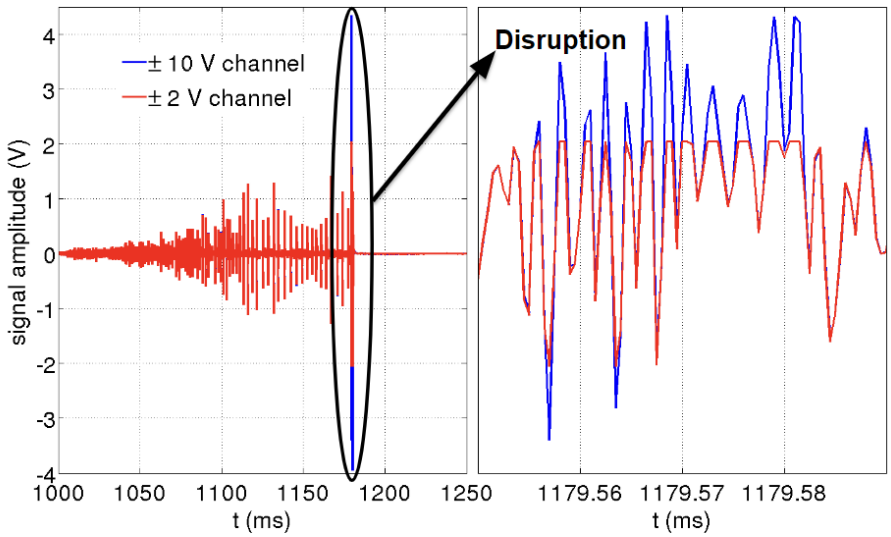

Figure 3.14: Mirnov coil data without numerical integration collected by ±2 V (0.06 mV/bit resolution) and ±10 V (0.3 mV/bit resolution) DAC channels. Left: the whole discharge; Right: during disruption.

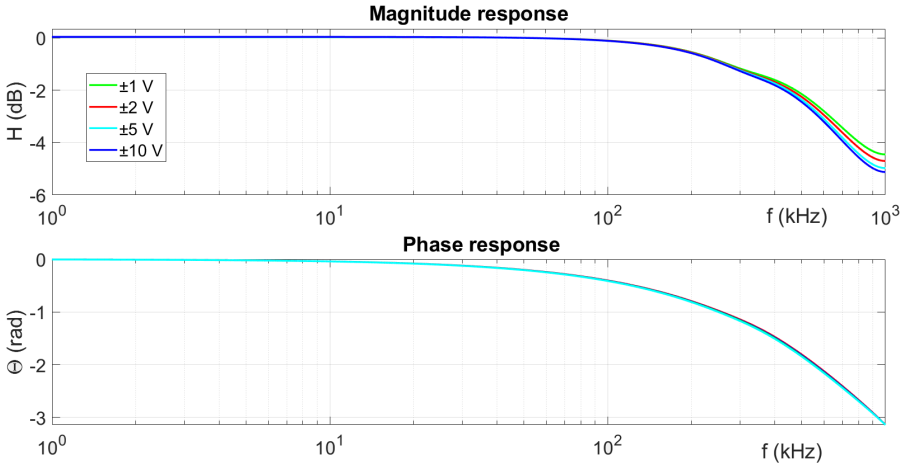

Figure 3.15: Measured filter characteristic of Nimbus DAC with ±1 V, ±2 V, ±5 V and ±10 V acquisition ranges. The attenuation of less than 5 dB at 1 MHz is observed, while the difference between the channels is less than 1 dB. Credits: the measurement was performed by Ales Havranek (IPP CAS).

An alternative approach of filter characteristic determination is its derivation from a test pulse wave signal collected by Nimbus channels. A pulse generator creates a wave with magnitude 1.8 V, which is recorded by Nimbus. In to achieve higher resolution signal and higher Nyquist BW the signal is oversampled - a step function is created as a multiple of overlapped steps from the original signal (Figure 3.16). This allows to calculate filter characteristic with frequencies reaching 10 MHz (Figure 3.17). The filter characteristics of the two acquisition channels ±2 V and ±10 start to deviate significantly at frequencies larger than 2 MHz, which is another confirmation that the channels can be combined without risk.

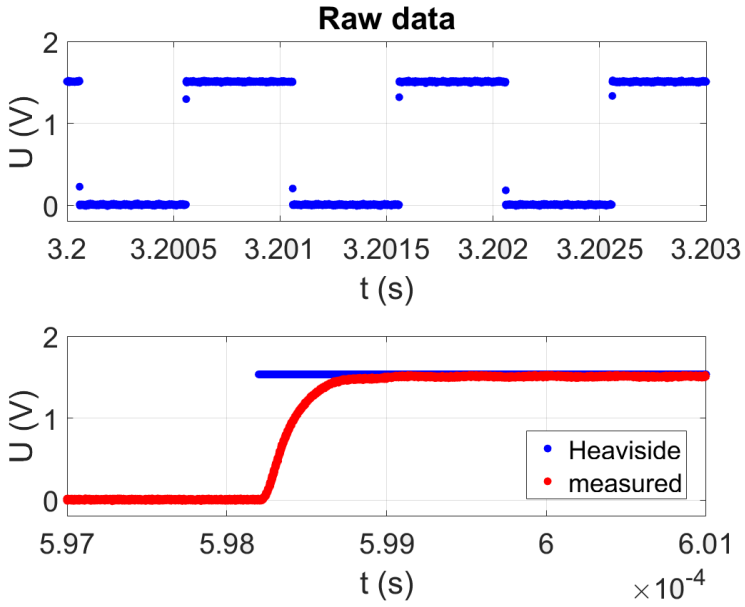

Figure 3.16: Left: Pulse generator signal measured with Nimbus. Right: Oversampled Nimbus signal and modelled Heaviside step function.

Another effect to consider when combining the two DACs is electronics recovery time after saturation. Several points of ±2 V DAC should be excluded after the channel returns from saturation. This is illustrated in Figure 3.18 where a

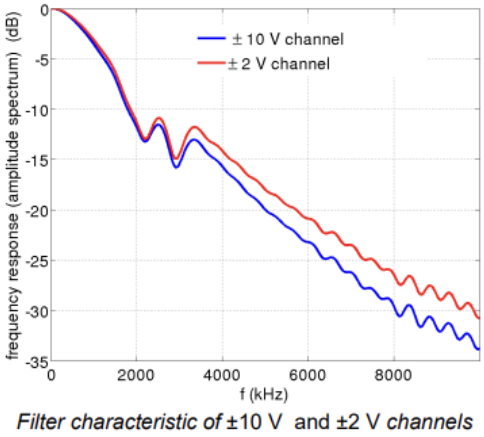

Figure 3.17: Filter characteristic of Nimbus DAC with acquisition range ±2 V and ±10 V

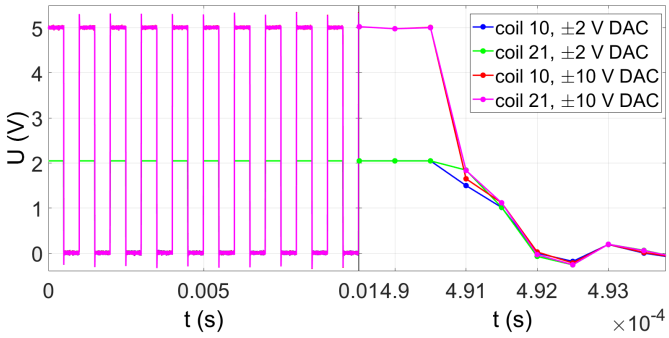

Figure 3.18: DAC recovery after saturation.

signal from a pulse generator is recorded by Nimbus DACs with ±2 V and ±10 V acquisition ranges. The magnitude of the pulse wave is 5V, hence ±2 V DAC reaches saturation, while ±10 V DAC remains in operation. When the magnitude changes from 5 V to 0 V it can be noticed, that ±2 V DAC slightly deviates from ±10 V DAC at 1-2 points of the ramp down. For safety margin 5 point are excluded after ±2 V DAC saturation in the two channels combination procedure.

Finally, different calibration and offset of the channels should be taken into account. Knowing that ±2 V and ±10 V DAC channels measure the same underlying signal, the calibration and offset can be found using regression between the channels measurements. However, linear regression cannot be used as both ±2 V and ±10 V DAC signals have their independent errors. Therefore, orthogonal distance regression method is implemented, where offset K_{offset} and slope K_{calibr} coefficients of the resulting line correspond to calibration and offset coefficients for DACs combination. Any of the channels can be used as a reference one, and the other should be pre-processed before combining the two of them together:

$$\begin{aligned} S_{\pm 2V} &= K_{offset} + K_{calibr} * S_{\pm 10V} \\ S_{\pm 10V} &= S_{\pm 10V} \end{aligned} \tag{3.7}$$

The finalised procedure of the channels combination consists of the following steps:

- Replacement of ±2 V DAC raw data points with ±10 V DAC raw data points at instances where ±2 V DAC is saturated
- Replacement of ±2 V DAC raw data points with ±10 V DAC raw data points at 5 time instances after ±2 V DAC returns from saturation.
- Elimination of the differences between the channels due to calibration and offset
- Numerical integration

An example of integrated data improvement by combination of two DACs with ±2 V and ±10 V acquisition range is shown in Figure 3.19. It can be seen that both channels individually result in a parasitic offset after disruption (although the underlying reason for that differs). However, the combination sets the offset to almost zero, indicating reliability of the integrated data.

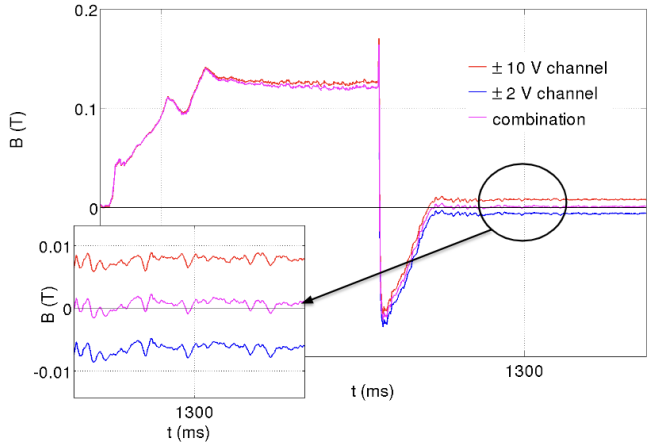

Figure 3.19: Combination of two DACs with ±2 V and ±10 V after numerical integration.

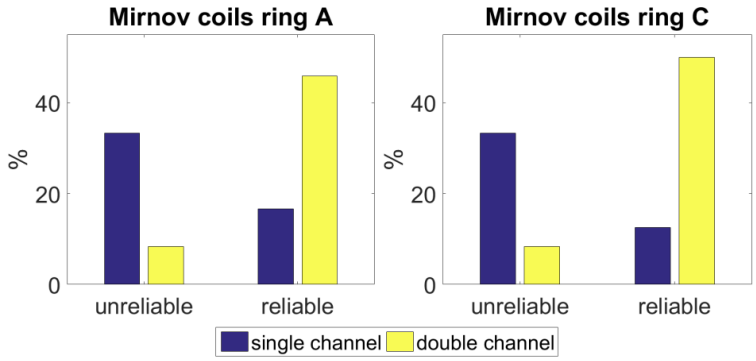

Figure 3.20: DAC improvement statistics

In order to assess overall performance of the channel combination technique 132 discharges were analysed. The channel was considered to be reliable if the offset after disruption does not exceed 1% of the flat-top I_p value. On the contrary, an unreliable channel is defined as having an offset larger than 5%. Only these two extreme cases are considered. Figure 3.20 shows that since implementation of the DACs combination procedure the number of reliable channels significantly increased, while the number of unreliable channels dropped.

3.1.6 Toroidal Mirnov coils connection

The COMPASS tokamak is equipped with 3 rings of Mirnov coil that measure variation of the toroidal magnetic field. These coils are referred to as toroidal Mirnov coils. However, only Ring A was connected before May 2019, when Rings B and C were also put into operation. The coils were connected to ATCA4 data acquisition system and require numerical integration. The data processing is complicated by $\pm 10V$ acquisition range of ATCA4 channels, while the raw signal during disruptions rarely reaches 1 V (an example is shown in Figure 3.21). This results in accumulation of error during numerical integration and subsequent spurious offset after the disruption (indicating corruption of the integration). In order to amplify the signal it was suggested to replace two resistors in ATCA4

channel electronics to change the integration gain (Figures 3.22 and 3.23).

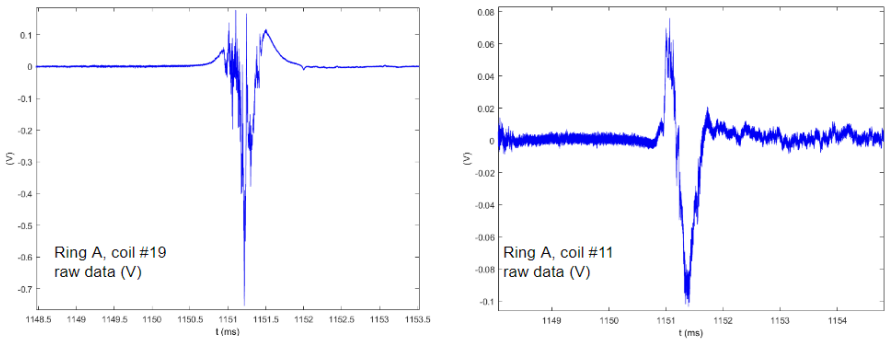

Figure 3.21: Raw signal of toroidal Mirnov coils #19 and #11 in the vicinity of the plasma-wall contact during disruption. These coils are expected to detect one of the largest toroidal magnetic field variation compared to the other coils due to the close presence of plasma and halo currents flowing in that region. The signal magnitude does not exceed 1 V

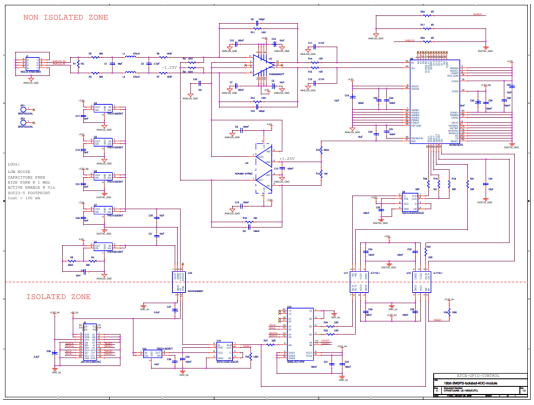

Figure 3.22: Electronic schematics of ATCA A/D channel

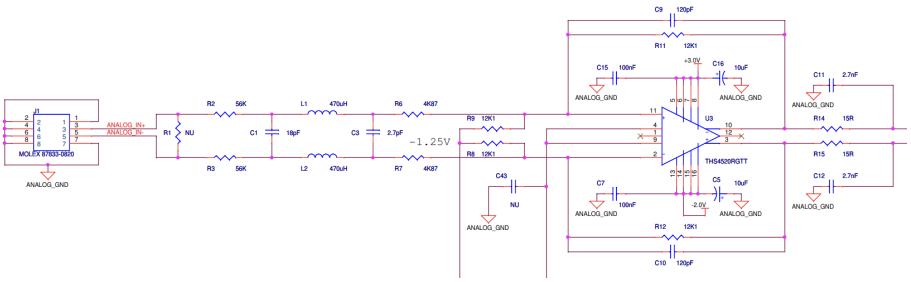

Figure 3.23: Part of the electronic schematics of ATCA A/D channel. Resistors R2 and R2 are replaced from 56 kOhm to 6,2 kOhm, changing the acquisition range from $\pm 10V$ to $\pm 2.12V$

The result of the resistors change is illustrated in Figure 3.24. It can be seen that the majority of discharges had large offset after disruption at $\pm 10V$ acquisition range (blue curve). The offset drastically decreases after modification of ATCA A/D channel.

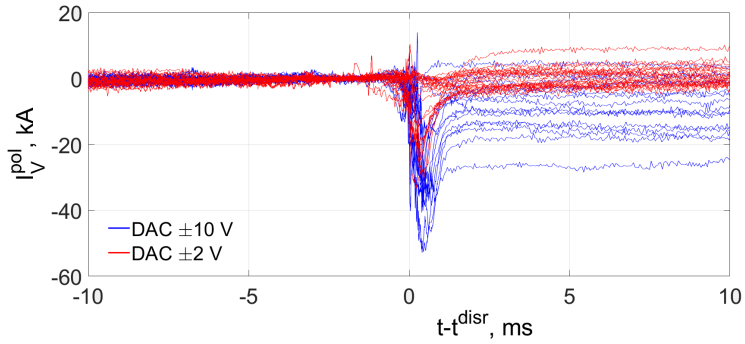

Figure 3.24: Toroidal Mirnov coil #5 Ring B: integrated signal during numerous upward disruptions (having plasma-wall contact in the vicinity of the coil). Red curve corresponds to new acquisition range $\pm 2.12V$ and blue curve - $\pm 10V$. The time axis is centred around disruption time.

3.1.7 Plasma current reconstruction by discrete coil

In addition to the plasma current measurement provided by the full internal Rogowski coil, it is possible to reconstruct I_p using IPR and Mirnov coils [86]. In this case integration in Equations 3.2 and 3.3 is replaced by a discrete summation:

$$\sum_i B_p^i l_{eff}^i \approx \mu_0 I_p \tag{3.8}$$

where B_p^i is the poloidal field measured by the coil and l_{eff} is the effective length of each coil. l_{eff} parameter is introduced in order to interpolate the magnetic field between the coils. It exploits an assumption that the magnetic field is a const=B_p^i around predefined distance along the vacuum vessel wall. The end points of l_{eff} are defined as the coordinates in the middle between the coils. The effective lengths of Mirnov coils and IPRs are listed in Table 3.3

The magnetic field detected by IPR and Mirnov coils includes parasitic signal from PF coils and the vacuum vessel. In order to reliably reconstruct I_p these crosstalk has to be eliminated. Crosstalk removal is done with the help of a special vacuum discharge, where the contributions from various PF coils can be separated in time and treated individually. Figure 3.25 illustrates processing of Mirnov coil #9 in Ring A signal in a vacuum discharge # 14855. The voltage detected by the coil is shown in the Figure 3.25 (top left). According to Faraday's law the voltage measured at the ends of the coils wire is proportional to the time-derivative of the magnetic field:

$$\oint_l Edl = -\frac{d}{dt}(\int_S BdS)$$
$$U = -S\dot{B} \tag{3.9}$$

where S is the effective area of the coil. Therefore, integration of the signal is required. While IPR and Mirnov coils Ring B have analugue integrators, Mirnov coils Rings A and C have to be integrated numerically. Backward Euler integration method is used:

$$S_i = S_{i-1} + t_{int} \cdot S_i^{raw} \tag{3.10}$$

Coil #	Mirnov coils l_{eff} [m]	IPR l_{eff} [m]
1	0.090621945	0.13602458
2	0.085749128	0.13693183
3	0.092317927	0.13778504
4	0.097649731	0.13632390
5	0.091052104	0.11940165
6	0.090372090	0.10775746
7	0.080375175	0.11209263
8	0.071577956	0.11360674
9	0.073809696	0.11551406
10	0.074900541	0.11360674
11	0.075440601	0.11209263
12	0.076121595	0.10775746
13	0.076202341	0.11940165
14	0.076102482	0.13632390
15	0.075427552	0.13778504
16	0.074894042	0.13693183
17	0.073788115	-
18	0.071631039	-
19	0.080354964	-
20	0.090406541	-
21	0.090904738	-
22	0.097365943	-
23	0.092269458	-
24	0.085789725	-

Table 3.3: Effective length L_{eff} of Mirnov coils and IPR coils.

where integration time step t_{int} is DAC sampling interval ($5 \cdot 10^7 ms$), S is the integrated data and S^{raw} is non-integrated signal. Accumulation of errors during numerical integration result is a baseline drift that can be seen in Figure 3.25 (top right). It is removed by fitting a first order polynomial to the time intervals where only linear noise is drifting and there are no variations in PF coils currents. Universal intervals for drift removal that can be applied to majority of COMPASS discharges are 550-640 ms and 1300-1400 ms. The resulting baseline is then subtracted from the numerically integrated signal. The signal without linear drift is shown in Figure 3.25 (bottom left). Figure 3.25 (bottom right) shows each PF coil contribution individually.

First step of cross-talk removal consists of determination of normalization coefficients that allow conversion from PF coils currents to the corresponding created magnetic field:

$$K_{PF-coil} = \frac{< S_{magn-coil} >}{< I_{PF} >} \tag{3.11}$$

where $< S_{magn-coil} >$ is the time-averaged integrated signal from magnetic coil (Mirnov or IPR), $< I_{PF-coil} >$ is the time-averaged current in PF coil and $PF-coil$ denotes the type of PF coil (MFPS, SFPS, EFPS, BR or BV). The averaging is performed in the time intervals where PF coils currents have stabilized.

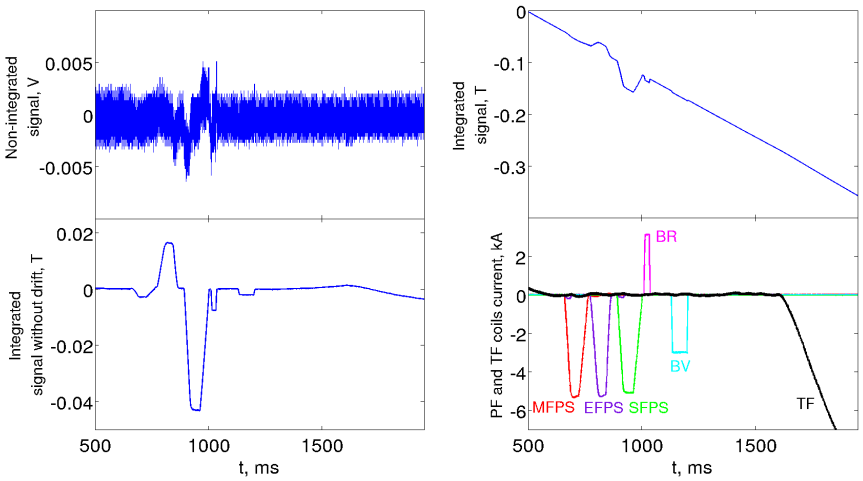

Figure 3.25: Processing of Mirnov coil #9 in Ring A signal in a vacuum discharge # 14855. Top left: raw non-integrated signal. Top right: numerically integrated signal with drift. Bottom left: numerically integrated signal after drift removal. Bottom right: currents in PF coils.

Therefore the cross-talk field take the following form:

$$S^{linear}_{cross-talk} = \sum_{PF-coil} K_{PF-coil} \cdot I_{PF} \tag{3.12}$$

The cross-talk field is subtracted from the magnetic coil integrated signal, which in case of the vacuum discharge results in an almost zero signal. An example of such a treatment is shown in Figure 3.26 (top). It can be seen that the integrated data from Mirnov coil #9 Ring A has significant jumps of the signal which correspond to PF coils currents in time (red curve). The signal after cross-talk removal eliminates this effect (blue curve). However, upon closer inspection it can be noticed that some faster variations of the signal are present ar the time corresponding to PF coils currents ramp up and ramp down. This is so=called non=linear cross=talk due to vessel currents induced by the fast change of magnetic field. It can be eliminated by solving lumped element circuit model 2.3 for PF coils assuming that contributions from each magnetic diagnostic coil can be treated individually and mutual inductance between them can be neglected. Variation of I_p is not taken into account. Equation 2.3 then reduces to the following form:

$$I_{PF} = \tau_{mut} \frac{dI_{VV}}{dt} - \tau_{self} \frac{dI_{PF}}{dt} \tag{3.13}$$

where $\tau_{mut} = \frac{L_{VV,PF}}{R_{PF}}$ and $\tau_{self} = \frac{L_{PF,PF}}{R_{PF}}$ are treated as non-linear cross-talk coefficients. With known current in PF coils I_{PF} equation **??** can be solved using backward Euler integration for each PF coil for any pair of τ_{mut} and τ_{self}. The coefficients were then manually adjusted to minimise the cross-talk effect. The resulting signal after non-linear cross-talk removal is shown in Figure 3.26 (bottom).

Up until now the vessel currents induced by the plasma current quench during disruptions have not been considered. A simplified method to account for this

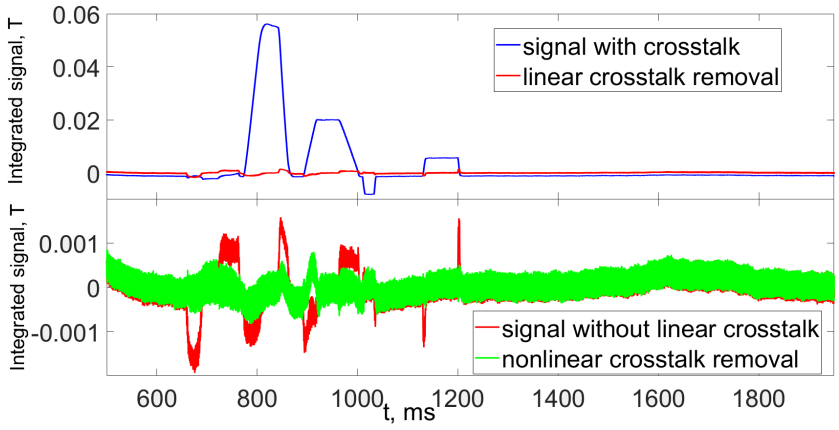

Figure 3.26: Illustration of PF originated cross-talk in Mirnov coil #9 in Ring A signal in a vacuum discharge # 14855. Top: linear cross-talk removal. Blue curve - Mirnov coil signal after integration and drift removal, strong cross-talk up to ∼0.06 T is present; Red curve - signal after linear cross-talk elimination. Bottom: non-linear cross-talk removal. Red curve - Mirnov coil signal without linear cross-talk (zoom of the top figure); Green curve - signal after non-linear cross-talk elimination

effect uses total toroidal vessel current obtained from Rogowski coil and External Partical Rogowski coil: $I_{VV}^{tor} = I_{p+VV}^{tor} - I_p$. Another kind of vacuum discharge is exploited, as presence of the vacuum vessel currents is required while there is no plasma in the vessel (#14888 is used in this work). The cross-talk is removed from reconstructed I_p (according to equation 3.8) where other types of cross-talks were already removed. The reconstructed signal is then treated similarly to equation 3.14:

$$K_{VV} = \frac{< I_{magn-coil} >}{< I_{VV}^{tortotal} >} \tag{3.14}$$

where $< I_{magn-coil} >$ is I_p signal reconstructed by magnetic coils (IPR or Mirnov). The result of this procedure applied to a plasma discharge is illustrated in Figure 3.27 where non-negligible difference is observed between I_p with and without vacuum vessel currents cross-talk (blue and red curves) in the interval of toroidal vessel currents presence (green curve). Note that ideally the cross-talk during disruption should be removed by considering the response of every vessel segment to the change of current around. A possible solution is to use local toroidal vessel currents obtained by pairs of IPR and EPR coils and eliminate cross-talk individually in each magnetic coil. However, an attempt to implement this was not successful and significant parasitic signal was observed in the coils located on the LFS (Figure 3.14, right). It can be seen as a large positive spike of coil #2 (LFS) signal after current quench start (marked as t^{disr}). This is due to more magnetically inert walls further from the tokamak geometrical centre. Moreover, several coils on the top of the vacuum vessel (#6 and #7) are also immune to vessel-currents cross-talk removal, while their counterparts in the bottom (coils #19 and #20) can be treated successfully. It was not clear where this different in behaviour originates. Therefore, it was preferred to treat the vessel currents cross-talk after I_p reconstruction using total toroidal vessel current. As a result,

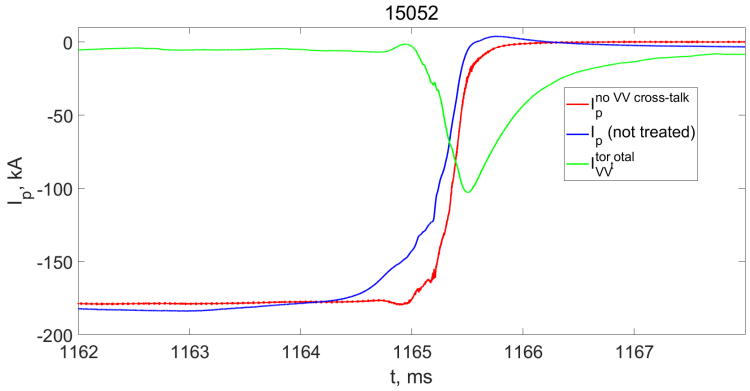

Figure 3.27: Removal of the cross-talk induced by toroidal vessel current in discharge # 15052. Green curve - total toroidal vessel current deduced using Rogowski coil and External Rogowski coil. Blue curve - the plasma current with cross-talk present. Red curve - the plasma current with cross-talk eliminated.

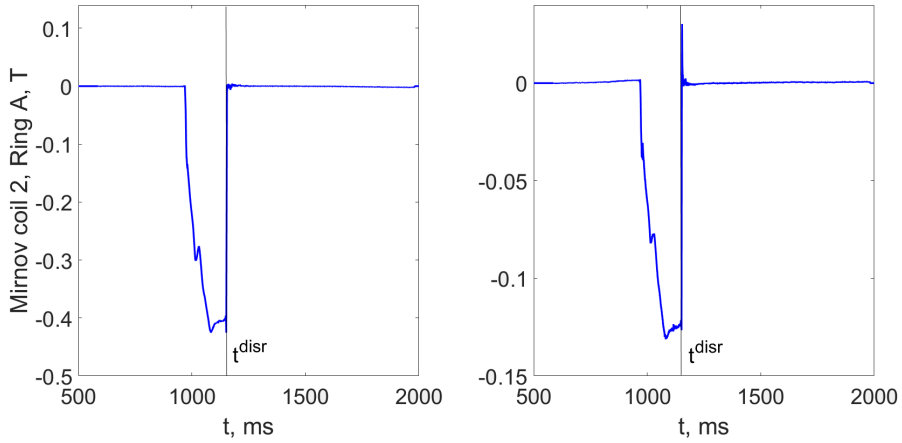

Figure 3.28: Mirnov coils signals after cross-talk removal in discharge #14856. Linear, non-linear and local vessel currents contributions were taken into account. Left: Mirnov coil # 12 (HFS); Right: Mirnov coil # 2 (LFS)

the post-processed signal represents plasma behaviour independent on PF coils parasitic signal and partly independent on vessel currents.

It should be taken into account, that some of the coils are broken and cannot be used in calculation of I_p. Therefore, the effective length of the neighbouring coils should be extended accordingly. Moreover, some coils have less reliable data than others. Their data quality can vary from discharge to discharge making some coils more useful for I_p calculation, while other coils might bring significant error. An algorithm was developed to automatically determine the combination of magnetic coils that provides most accurate result. Least deviation between I_p measured by full Rogowski coil and I_p reconstructed by discrete magnetic coils serves as a figure of merit of reconstruction quality. The procedure consists of the following steps:

- Preparation of data from magnetic coils without analogue integrator: raw signal is processed as described in section 3.1.5: channels with different sensitivities are combined, the signal is numerically integrated and the drift

is removed

- Linear and non-linear cross-talks are removed
- Permanently non-working coils are removed from the coils list used in I_p reconstruction
- Faulty coils are identified and removed from the coils list used in I_p reconstruction: this includes failure of the data acquisition system as well as coils having large offset after disruption ($> 10\%$).
- Among the remaining coils suitable for I_p reconstruction it is a prerequisite that at least 12 coils will be used.
- All possible combinations of the suitable coils and formed and their effective lengthes are determined.
- For each combination I_p is reconstructed
- Deviation from full Rogowski coil I_p^{Rog} is determined as two offsets - before and after disruption: $S_{offset}^{before/after} = |\frac{<I_p^{Rog}> - <I_p^{coil}>}{<I_p^{Rog}>}|$. Here I_p^{coil} is the plasma current reconstructed with a defined set of discrete magnetic coils. Averaging is performed in the following intervals: over 1 ms starting from 5 ms before disruption for S_{offset}^{before} and over 100 ms starting from 200 ms after disruption for S_{offset}^{after}.
- Among coils combinations that deviate from I_p^{Rog} by 5 % at maximum the least S_{offset}^{after} is found. This is considered as a best coils combination for I_p reconstruction.

The resulting reconstructed I_p is then stored in the COMPASS database CDB.

3.2 Current quench characterisation

Plasma displacement and current quench are the main phases of disruption that determine the currents flowing in the vacuum vessel wall and hence the forces acting on the machine. Understanding of the current quench parameters and related vessel currents can help determining disruptions scenarios and their mitigation in future machines. Therefore, it is crucial to investigate the related parameters such as the duration and rate of the plasma motion as well as I_p decay. This section summarises the extensive current quench characterisation reported in [2]. An example of CQ in several representative disruptions is shown in Figure 3.29. I_p decay can take different waveforms such as almost linear (Figure 3.29, top), fast drop of I_p in the beginning of CQ which is slowed down later (Figure 3.29, middle), slower beginning of CQ with fast I_p drop at the end (Figure 3.29, bottom). Another characteristic feature indicating TQ is the I_p spike marked in Figure 3.29 (bottom). The following CQ characterisation takes an approach of International Tokamak Physics Activity (ITPA) disruption database IDDB [66] which contains disruption parameters from more than 10 tokamaks from all over

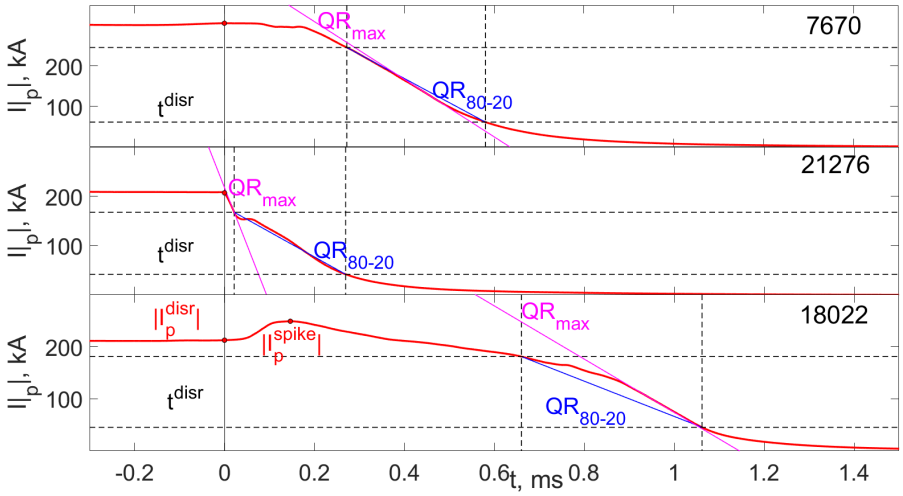

Figure 3.29: Examples of I_p decay behaviour at COMPASS. Top: maximum quench rate QR_{max} is only slightly different from QR_{80-20}; Middle: non-linear I_p - rapid drop of I_p in the beginning of CQ and slower decay later. Bottom: major disruption with prominent I_p spike in the beginning of CQ. Slower decay rate in the beginning, which accelerates towards the end of CQ.

the world. While the COMPASS tokamak is not included in IDDB, it is beneficial to determine the parameters used there.

The characteristic I_p can take up to 25 % of the predisruptive plasma current I_p^{disr} (Figure 3.30, left). Note the spike is more prominent in major disruptions (marked by blue circles). This might be due to higher stored magnetic energy as it can be seen in Figure 3.30 (right).

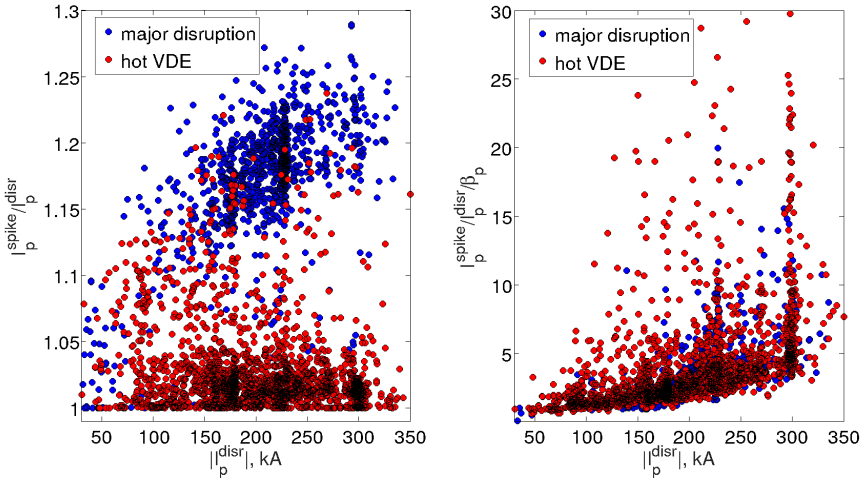

Figure 3.30: Characteristic I_p spike statistics with respect ro predisruptive plasma current I_p^{disr}. VDEs are marked by blue color and major disruptions by red color. Left: The spike magnitude is normalized to I_p^{disr}. Right: The spike magnitude is normalized to I_p^{disr} and β_p

The current quench time τ_{CQ} defines the duration of I_p decay. It is often calculated as a linear extrapolation of τ_{80-20} : $\tau_{CQ} = 1.67 \cdot \tau_{80-20}$, where τ_{80-20}

is the time of I_p drop from 80 % to 20 % of I_p^{disr}. Note that while the interval 80-20 % is widely used, some machines can exploit different intervals such as 90-10 % at ADITYA [87] or 80-30 % at EAST [60]. The choice of the interval is affected by the presence of eddy currents in the vacuum vessel, which can induce parasitic signal in I_p measurement. Similarly, CQ rate QR_{80-20} can be defined as the linear I_p decay over the τ_{80-20} interval. In order to compare current quench time between different devices the plasma area and self-inductance should be taken into account. Area-normalised current quench time τ_{CQ}/S at COMPASS uses plasma area prior to the displacement (at least 3 ms before the start of the CQ). ITPA defines a minimum value of τ_{CQ}/S across multi-device database as 1.67 ms/m^2 (Figure 3.31). The limit found at COMPASS is 2.1 ms/m^2 (Figure 3.32, right), which is consistent with ITPA. The limit lowers to 1.73 ms/m^2 when self-inductance normalisation is performed using a dimensionless parameter L = ln(8R/a)-1.75.

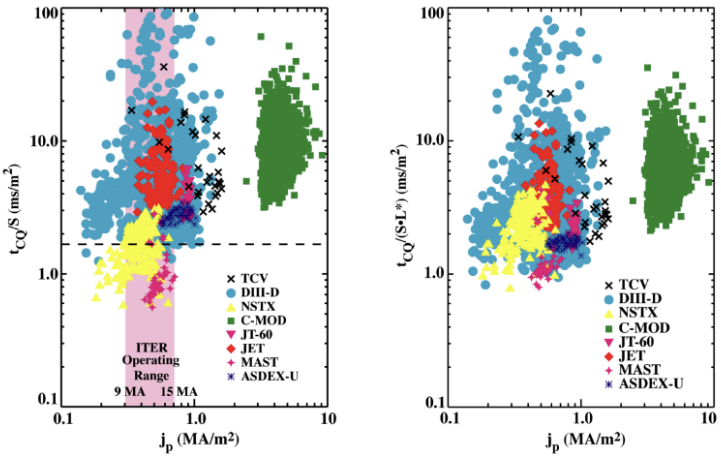

Figure 3.31: ITPA limit as reported in [88] (Figures 2 and 3). Left: area-normalised current quench time. Right: current quench time normalised by area and self-inductance

Note that there is a number of data entries that lie below the indicated ITPA limit of 1.67 ms/m^2 (Figure 3.32, left). These disruptions belong to the group with significant RE presence (which are not taken into account in ITPA). RE discharges are indicated by yellow dots in the figure and are not taken into account in further statistics. An example of an extreme RE disruption is presented in Figure 3.33. In this case Rogowski coil integrator failed which is indicated by a spurious offset of the signal after disruption (red curve). An upper bound of the CQ time can be estimated by external Rogowski coil measuring I_p together with the vessel currents, which results in $\sim$ 1000 kA/ms rate, which is faster that any of non-RE quench rates (on average 168 kA/ms). In addition to this, I_p was calculated using Mirnov coils Ring B, which provided $\sim$ 6000 kA/ms quench rate. However, this is an exceptional case even during RE campaigns. Disruptions that are not affected by RE have QR_{80-20} distribution shown in (Figure 3.34)

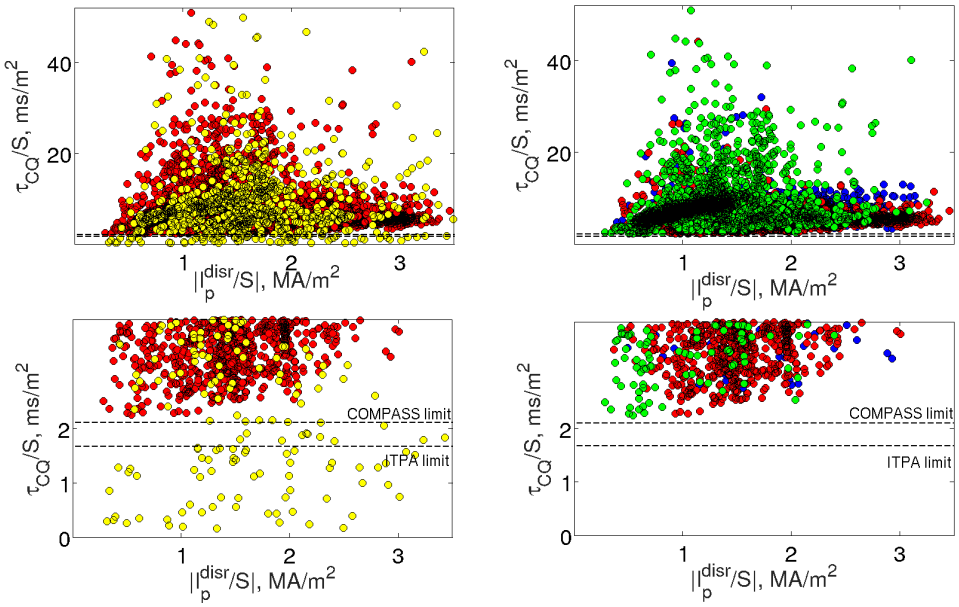

Figure 3.32: Statistical analysis of current quench time τ_{CQ} at COMPASS. Quench time τ_{CQ} is plotted against I_p^{disr}, both parameters are normalised to predisruptive plasma area S. Dashed line at $\tau_{CQ}/S = 1.67ms/m^2$ indicate the lower bound that is common to many tokamaks (determined in international disruption database IDDB). Dashed line at $\tau_{CQ}/S = 2.1ms/m^2$ indicates lower limit for COMPASS. The limit does not consider RE discharges (shown by yellow dots on the left figure). Right figure distinguishes different disruption directions: downward - red color, upward - blue color, HFS - green color.

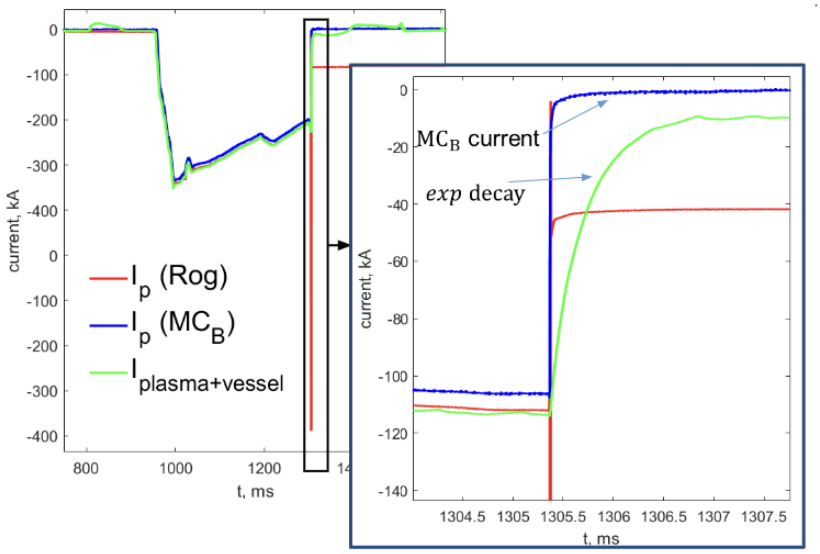

Figure 3.33: Extremely fast CQ during disruption in discharge #10806 (RE campaign). Red curve - I_p measured by Rogowski coil. Blue curve - I_p measured by Mirnov coils Ring B. Green curve - I_p together with the vessel current measured by external Rogowski coil.

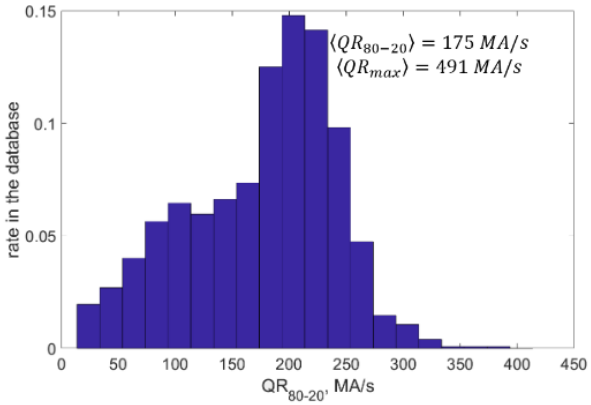

Figure 3.34: Occurrence of various QR_{80-20} in the COMPASS disruption database (only upward and downward disruptions without RE are taken into account)

3.3 Currents in the vacuum vessel wall

This section summarises the vessel currents measurements reported in [2] and provides additional example of unusual disruptions.

3.3.1 Toroidal vessel currents

A basic measurement of toroidal vessel current exploits combination of internal and external Rogowski coils: $I_{VV}^{tor} = I_{p+VV}^{tor} - I_p$, where I_{p+VV}^{tor} is the sum of the plasma current and vessel current measurement by external Rogowski coil. However, no information about toroidal vessel current distribution can be obtained with this technique. Local toroidal vessel currents densities are provided by pairs of IPRs and EPRs, which together serve as a small Rogowski coil encircling a toroidal slice of the vacuum vessel (Figure 3.35): $J_V^{tor} = \frac{2L(B_{EPR}-B_{IPR})}{\mu_0}$.

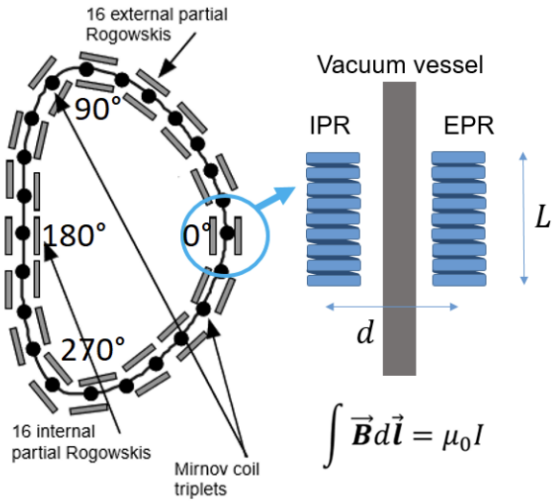

Figure 3.35: A pair of IPR and EPR coil that can serve as a Rogowski coil for toroidal vessel current measurement.

An example of toroidal vessel currents distribution is presented in Figure 3.36. Before the plasma column starts vertical movement no currents are detected by

the coils. Vertical displacement (upwards in this case) induces currents in the top and bottom part of the vacuum vessel to prevent the movement. The final phase is governed by CQ resulting in concentrated toroidal vessel currents in the top part of the vacuum vessel (where the plasma is heading).

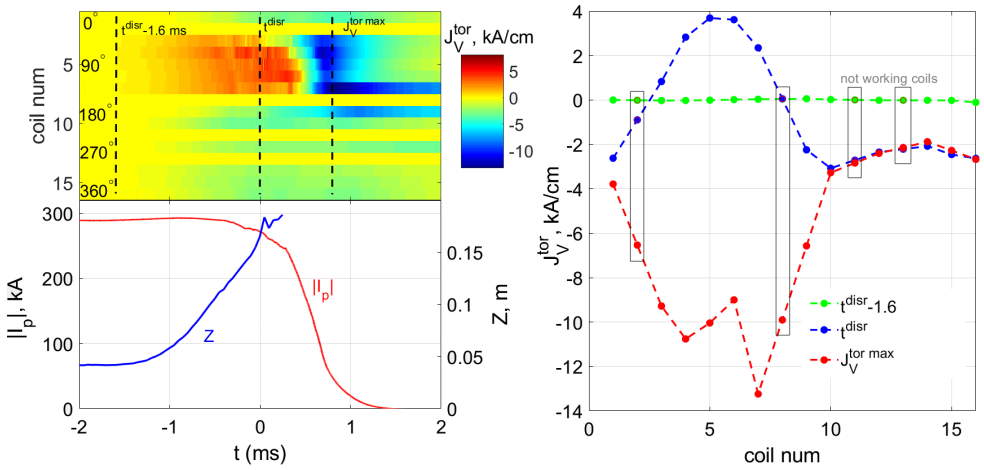

Figure 3.36: Toroidal vessel currents overview in discharge #19396 (hot VDE). Left top: toroidal vessel current density distribution over the poloidal cross-section of the vacuum vessel. Left bottom: vertical position Z (blue curve) and plasma current $|I_p|$. Right: Individual instances of the density distribution over the poloidal cross-section: before the start of the vertical displacement (green curve), during the vertical displacement (blue curve) and during CQ (red curve).

An interesting plasma behaviour was observed in discharge #20746 (Figure 3.37) during restart campaign. A disruption happened during ramp down with the flat-top current being $I_p \sim 238$ kA and predisruption plasma current $I_p^{disr} \sim 68$ kA. Initially the plasma column was moving upwards (Figure 3.37, left bottom) approximately until 3.5 ms before the start of CQ. However, the direction of the movement reverses resulting in a downward hot VDE. Both upward and downward movements induce dipole-like toroidal vessel currents in the top and bottom parts of the vacuum vessel. The polarity of these currents is consistent with the direction of the movement: counter-I_p vessel currents if the plasma moves towards the wall and co-I_p currents if the plasma moves away from the wall. In general, the direction of the vertical displacement should depend on the initial plasma position with respect to neutral point - the position where the plasma can be balanced by toroidal eddy currents. The plasma having the position upper from the neutral point will typically continue its motion upward and the plasma with the position lower than the neutral point disrupts in downward direction. However, this pattern can be interrupted by TQ and flattening of the plasma current profile. It was demonstrated at ASDEX-Upgrade [31] that plasma is pulled in the direction of divertor during TQ. In case of COMPASS discharge #20746 TQ occurs approximately at the time when the plasma column changes its direction of displacement. The TQ is manifested in a small spike in the I_p profile (Figure 3.37, left bottom) and can be a reason behind unusual vertical position behaviour.

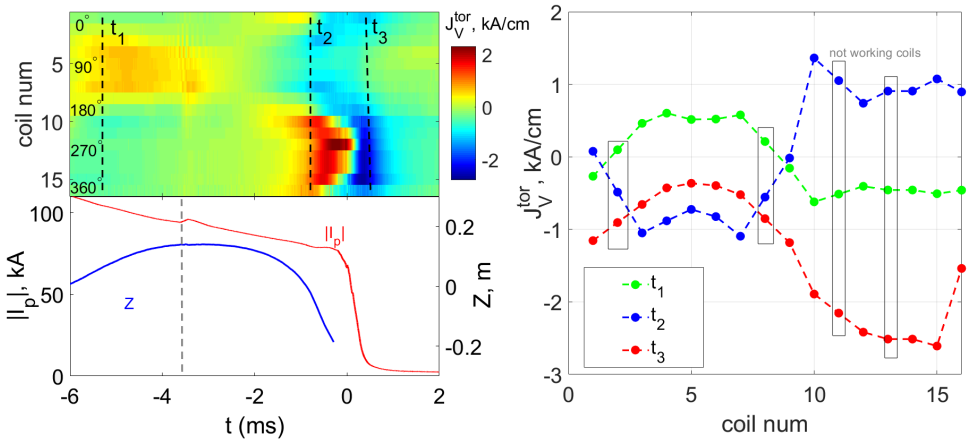

Figure 3.37: Toroidal vessel currents overview in discharge #20746 (hot VDE). Left top: toroidal vessel current density distribution over the poloidal cross-section of the vacuum vessel. Left bottom: vertical position Z (blue curve) and plasma current $|I_p|$. Right: Individual instances of the density distribution over the poloidal cross-section: during the movement upward (green curve), during the movement downward (blue curve) and during CQ (red curve).

3.3.2 Net poloidal eddy currents

Poloidal currents in the vacuum vessel (regardless of their nature) can be determined using toroidal Mirnov coils according to Ampere's law: $I_V^{pol} = \frac{2\pi R_0}{\mu_0}\Delta B$, where $\Delta B = B_{tor}^{ext} - B_{tor}^{MC}$ is the difference between externally applied toroidal field at the position of the coil and the toroidal field measured by the coil (Figure 3.38). 3 rings of toroidal Mirnov coils, 24 coils each enables determination of local poloidal vessel currents covering the whole vessel cross-section. An example of such measurements is presented in Figure 3.39 showing a downward major disruption. It has clearly separated TQ phase where poloidal vessel currents are observed on the whole extension of poloidal cross-section. These are net poloidal eddy currents. The second distinctive feature is observed around the middle of the CQ where poloidal vessel currents are concentrated in the bottom part of the chamber. These are attributed to halo currents, which will be discussed in 3.3.3.

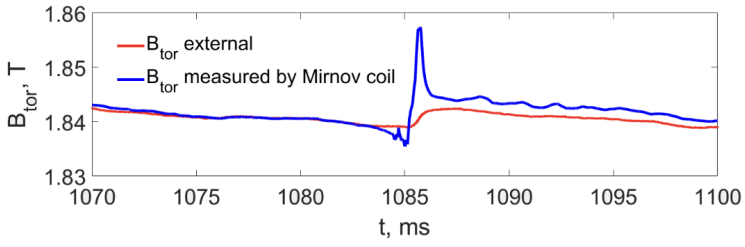

Figure 3.38: An example of Mirnov coil signal (blue curve) during disruption shown together with external toroidal field at the position of the coil (red curve).

It was shown that the net poloidal eddy current can be deduced using diamagnetic loop [89] as follows:

$$I_V^{pol} = \frac{V}{R_W} \tag{3.15}$$

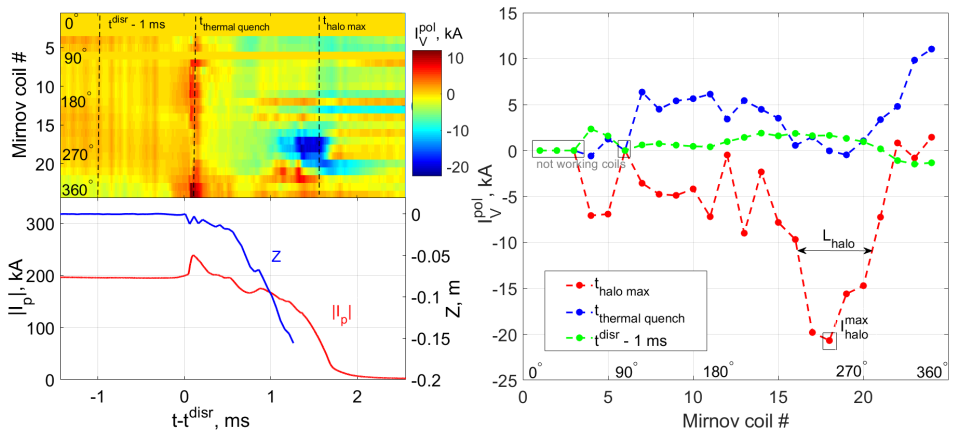

Figure 3.39: Poloidal vessel currents overview in discharge #18787 (major disruption). Left top: poloidal vessel current distribution over the poloidal cross-section of the vacuum vessel. Left bottom: vertical position Z (blue curve) and plasma current $|I_p|$. Right: Individual instances of the density distribution over the poloidal cross-section: before the start of the vertical displacement (green curve), during the TQ (blue curve) and during CQ (red curve).

where V is the voltage measured by Diamagnetic loop and R_W is the poloidal resistance of the vacuum vessel. In addition to this, the net poloidal eddy current can by analytically estimated using equations 2.8 and 2.9. A comparison between the three methods is presented in Figure 3.40 for a downward hot VDE. The signal from coil #8 is considered as it is located far from the plasma-wall contact region and should not be affected by halo current presence. The first positive spike of the signal of 5-7 kA corresponds to net poloidal eddy current induced by TQ. Relatively good agreement is observed between the Mirnov coils, diamagnetic coil and analytical solutions. Second spike in negative direction is induced by CQ. This phase cannot be represented by 2.8 model as EFIT reconstruction usually is not available during CQ, and the knowledge of β_p and elongation κ are required.

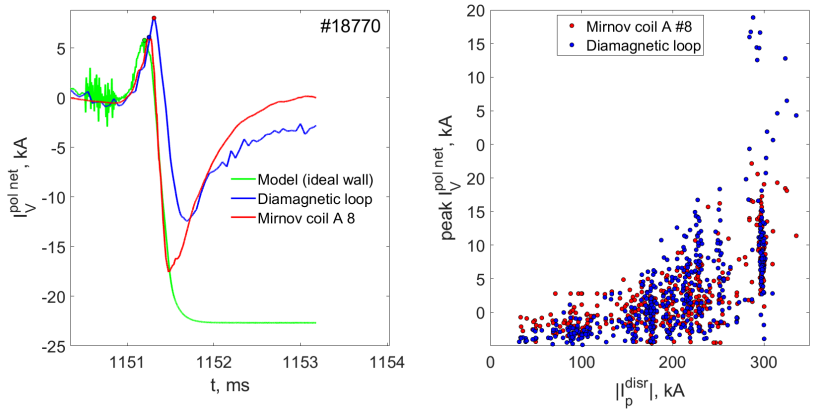

Figure 3.40: Net poloidal vessel currents measured by diamagnetic loop (blue color) and Mirnov coil #8 in Ring A (red color). Left figure shows discharge #18770 where comparison is done also with analytical solution using equation 2.9. All three signals reach approximately 5.3 kA during TQ. Right: the peak poloidal net currents are plotted against predisruptive plasma current.

3.3.3 Halo currents

Halo currents at COMPASS are measured primarily as a part of poloidal vessel current. When flowing in the wall, they can be detected by toroidal Mirnov coils the same way as the net poloidal eddy currents. Halo current exhibit quadratic dependence on plasma current and inversed dependence on toroidal magnetic field (as described in Section 2.2). The dependence is shown in Figure 3.41(left) together with the halo current plotted against $|QR_{80-20}/I_p^{disr}|$ (right). The latter plot was an attempt to investigate whether largest halo currents are observed at slower quench rates as it is predicted for ITER [90] and as observed at JET [51]. An opposite trend was reported at NSTX [54]. However, COMPASS data does not clarify the difference between the two trends as only a narrow range of QR_{80-20} is observed. This might be due to impurities coming from the carbon PFCs and enhancing radiation.

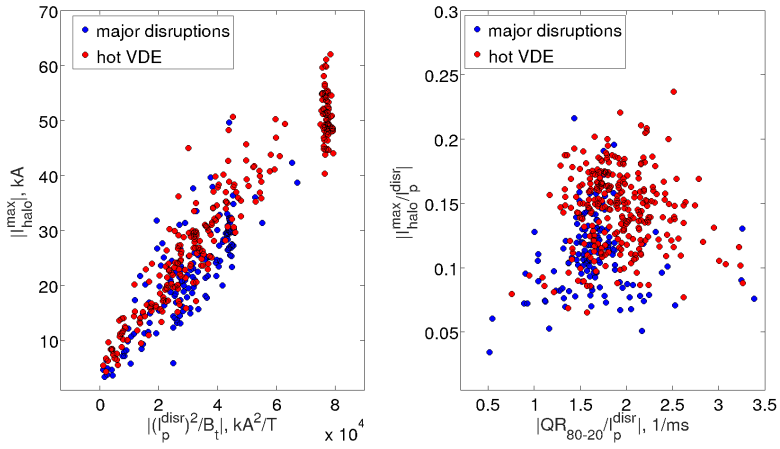

Figure 3.41: Halo currents at their maximum I_{halo}^{max} with respect to $(I_p^{disr})^2/B_t$ (left figure). Halo currents at their maximum I_{halo}^{max} plotted against current quench rate QR_{80-20} (right figure). Both parameters are normalised by I_p^{disr}

An important parameter of halo current is their extension in poloidal direction, which affect distribution of the forces acting on the vacuum vessel. While many machines (including COMPASS) are able to detect part of the halo width (e.g. by Langmuir probes), a set of Mirnov coils allows measurement of the full poloidal extension. This was used to validate a hypothesis that halo current density might be limited by ion saturation current [81]. A special set of disruption with different I_p was chosen for simultaneous analysis by Langmuir probes and Mirnov coils. It was shown by Langmuir probes that the halo current density is reaching the ion saturation current in these discharges. On the other hand, Mirnov coils provide clear proof that the halo current grows at larger I_p (Figure 3.41). This implies that the halo width has to increase at larger I_p (in agreement with equation 2.10). A result of this experiment is presented in Figure 3.42. A poloidal profile of halo current was taken at an instant where it peaks in time. The obtained profiles are averaged across several discharges having same I_p. The width at the half magnitude of the poloidal profile is referred to as halo width. The Figure 3.42 shows 3 groups of disruptions with flat-top I_p equal to $\sim 100kA$, $\sim 200kA$

and $\sim 300kA$. The halo width gradually increasing with I_p as can be seen on the right side of the Figure 3.42. At the same time, the maximum halo current detected in the vessel is also increasing. Therefore, this is consistent with the assumption of halo current density limitation.

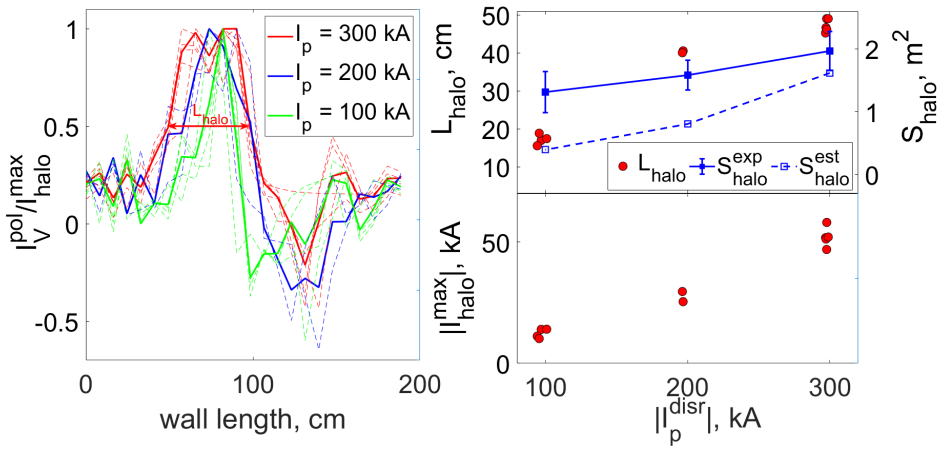

Figure 3.42: Left: halo current poloidal profiles used to determination of halo width. Right top: Halo width at FWHM is shown for discharges with flat-top plasma current $I_p \sim 110kA$, $I_p \sim 200kA$ and $I_p \sim 300kA$. Halo width estimated from the halo density according to 2.10 is shown by dashed blue line. Right bottom: growth of halo current with I_p.

When designing a vacuum vessel of a tokamak all possible paths of halo current should be considered. The COMPASS tokamak database includes several peculiar discharges with elongated plasma moving towards LFS during disruption. This are relatively rare occasions as usually time scale of the plasma current quench is shorter than the decay of stabilizing vertical magnetic field and plasma should be pushed to the HFS. However, in some case of hardware failure LFS directions is also possible. En example is given in Figure 3.43. In this discharge hydraulic system stopped the power supplies in the middle of the discharge. The power supplies started to lower their currents with pre-programmed ramps. The central solenoid created negative loop voltage and the plasma current started to decrease. However, the vertical magnetic field decreased at a faster rate than the plasma current resulting in a loss of radial stability and plasma column movement towards LFS. In Figure 3.43 the radial movement towards LFS is observed until ~ 1130.2 ms (red curve). Then the plasma drifts downward (blue curve) and I_p quenches. Note that although the plasma reached LFS the edge safety factor q is still larger than 2 an no current was transferred to the wall as can be seen from the toroidal Mirnov coils data measuring poloidal vessel currents (Figure 3.43, right). Halo currents appear only in the middle of the current quench (blue regions in Figure 3.43, right). Therefore, this type of disruption does not pose any threat to the vacuum vessel structures on the LFS.

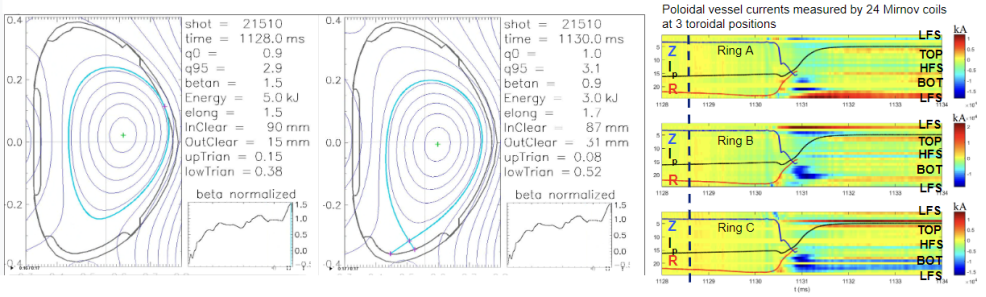

Figure 3.43: LFS disruption in discharge #21510 when hydraulic system failed. Left: EFIT reconstruction at the moment of plasma drift to the LFS. Middle: EFIT reconstruction during drift towards the bottom of the vacuum vessel (before CQ). Right: poloidal vessel currents measured by toroidal Mirnov coils at 3 positions in the vacuum vessel. Localized currents up to ∼15 kA are observed in the bottom part of the vacuum vessel.

Another type of LFS disruptions that needs to be considered occasionally occurs during RE campaigns. It was shown that RE discharges have require special care with respect to radial position control of circular plasma as the relativistic centrifugal force of the RE beam pushes the plasma towards LFS and standard feedback for the vertical magnetic field cannot cope with that effect [91]. In that case it is possible that poloidal currents will be concentrated on the LFS as shown in Figure 3.44. It depicts discharge #18876 where plasma is slowly drifting towards LFS (red curve) until the start of I_p decay (black curve). Vertical position of the plasma (blue curve) remains almost stable until the start of the current quench, when plasma starts to slide downwards.

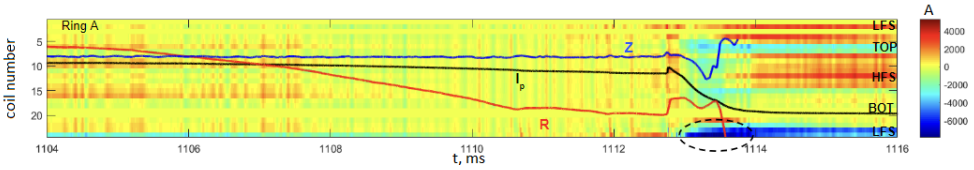

Figure 3.44: LFS disruption in discharge #18876 in RE campaign. Localized poloidal currents up to ∼5 kA are observed in the vessel on the LFS.

3.4 Asymmetrical disruptions

3.4.1 Plasma current asymmetry

It was observed that I_p measured at different toroidal positions tend to have substantially different waveforms and magnitudes (3.46), similarly as at JET [92]. First description of I_p asymmetries at COMPASS were reported in ([68]). This section extends previous investigations taking into account 5 toroidal measurements of I_p (instead of only 3 used before). In addition to this, rotation of the asymmetry is considered. Finally, relation to halo current measurement is provided.

Primary measurement of I_p is provided by Rogowski coil (Section 3.1). Rogowski coil data complimented by IPR coils and Mirnov coils measurement pro-

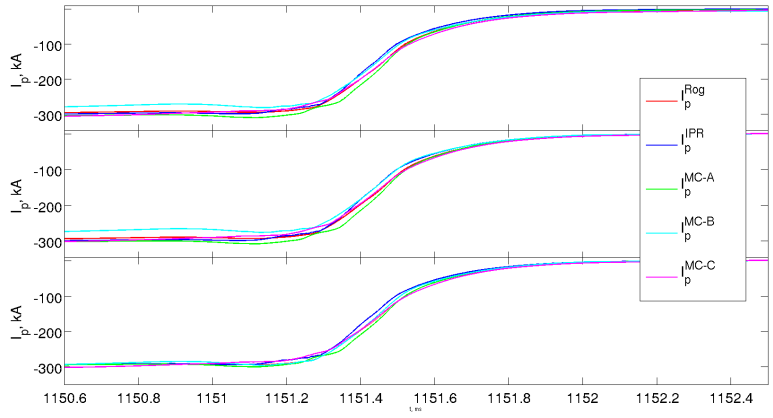

Figure 3.45: Preprocessing of I_p for asymmetry calculation. I_p measured by Rogowski coil (red curve) and reconstructed by IPR coils (blue curve), Mirnov coils Ring A (green curve), Ring B (cyan curve) and Ring C (magenta curve). Top: original signals without treatment. Middle: I_p offset after disruption is removed. Bottom: I_p curves are normalized to match Rogowski coil measurement

vides knowledge of I_p at 5 toroidal positions, 4 of which are orthogonal. An example of 5 measurements of I_p is shown in Figure 3.45 (top). It can be noted that the curves deviate from each other. However, before proceeding with determination of I_p^{coil} asymmetry it is necessary to perform pre-processing of I_p signals to normalize reconstructed I_p to the value measure by Rogowski coil I_p^{Rog} (which is assumed to be a primary reference measurement). At a first step, any offsets are removed from I_p signal. It is done by subtracting average value of the plasma current $< I_p >$ in the 0.5 ms interval starting 1 ms after I_p dropped to zero (Figure 3.45, middle). In the second step I_p^{coil} is normalised to I_p^{Rog} using the following coefficients:

$$K_{asym}^{coil} = \frac{< I_p^{Rog} >}{< I_p^{coil} >} \tag{3.16}$$

where averaging is performed in the interval of 0.5 ms starting from 1 ms before the CQ. The resulting normalized signal $I_{pnorm}^{coil} = K_{asym}^{coil} \cdot I_p^{coil}$ is shown in Figure 3.45 (bottom)

Assuming that 3D deformation of the plasma can be represented as $m/n = 1/1$ kink mode, the plasma current asymmetry can be described as a sine function:

$$I_p^{model}(\phi) = X_0 + X_1 sin(\phi + X_2) \tag{3.17}$$

where ϕ is the toroidal angle of the measurement location. The angle is counted from Rogowski coil ($\phi = 0°$) counter-clockwise (Mirnov coils Ring B at $\phi = 45°$, Ring C at $\phi = 90°$, IPR at $\phi = 180°$ and Mirnov coils Ring A at $\phi = 225°$). The magnitude of the asymmetry is determined using the least square method minimizing the difference between the $I_p^{model}(\phi)$ and the measured I_p:

$$min \sum_{i}^{5} (I_p^{model}(\phi_i) - I_p(\phi_i))^2 \tag{3.18}$$

Peak to peak magnitude of $I_p^{model}(\phi)$ is referred to as asymmetry magnitude I_p^{asym} and is determined at every time instant during $\tau_{CQ} \pm 1ms$. Normalized asymmetry magnitude is defined as the ratio between the asymmetry magnitude and predisruptive plasma current expressed in %:

$$A_p^{asym} = |\frac{I_p^{asym}}{I_p^{disr}}| \cdot 100\% \tag{3.19}$$

Asymmetry window ΔT is defined as the interval where the asymmetry magnitude in non-negligible, namely $A_p^{asym} > 2\%$. For simplification of the processing the asymmetry magnitude is then set to zero where this condition is not satisfied. During disruptions the electromagnetic forces acting on the vacuum vessel are affected not only by the magnitude of the asymmetry, but also by its duration. Therefore, a time integrated asymmetry (measured in ms) is introduced:

$$A = \int_{\Delta T} \frac{A_p^{asym}}{100\%} dt \tag{3.20}$$

The asymmetry can be locked on a certain position in the vacuum vessel or rotate toroidally. The number of rotation the asymmetry does and its frequency are determined using the phase of the fitted $I_p^{model}(\phi)$ function:

$$\begin{aligned} N_{turn} &= \frac{\phi_{max} - \phi_{min}}{2\pi} \\ f &= \frac{N_{turn}}{\Delta T} \end{aligned} \tag{3.21}$$

where ϕ_{max} and ϕ_{min} are maximum and minimum phases of $I_p^{model}(\phi)$ during ΔT. Disruptions having $N > 1$ are referred to as rotating and $N \leq 1$ - locked or standing. Examples of asymmetrical disruptions (rotating and standing) are shown in Figure 3.46. The left side of the Figure 3.46 represents a rotating disruption. The asymmetry window ΔT where $A_p^{asym} > 2\%$ is marked by yellow area with A_p^{asym} reaching $\sim 8\%$. The rotation can be clearly seen when comparing I_p measured in opposite toroidal positions: $\Delta I_p = I_p^{MC-B} - I_p^{MC-B}$ or $\Delta I_p = I_p^{Rog} - I_p^{IPR}$. Strongly varying ΔI_p that changes sign indicates rotational asymmetry (Figure 3.46, bottom left). The right sight of the Figure 3.46 represents standing asymmetry. While that while ΔI_p is larger than in the previous case, it does not change its sign, hence indicating standing or slowly rotating asymmetry.

About 87 % of disruptions at COMPASS are asymmetrical. The data collected over the period of June 2017 - October 2020 and includes $\sim$ 800 asymmetrical disruptions. Asymmetries are observed in all types of disruptions (major and hot VDEs) as well as in all directions (upward, downward and HFS). Time-integrated asymmetries at COMPASS are presented in Figure 3.47 and asymmetry magnitudes normalized to predisruptive plasma currents are shown in Figure 3.48. While previously reported asymmetries [68] reached 20 % at maximum, newly inspected discharges exhibit also larger values. This is due to ramp-down and RE discharges included in the current database. Longer I_p decay is beneficial for asymmetry developments. However, note that largest values up to 50 % are observed at very low $I_p < 100$ kA and do not pose significan threat in terms of electromagnetic loads.

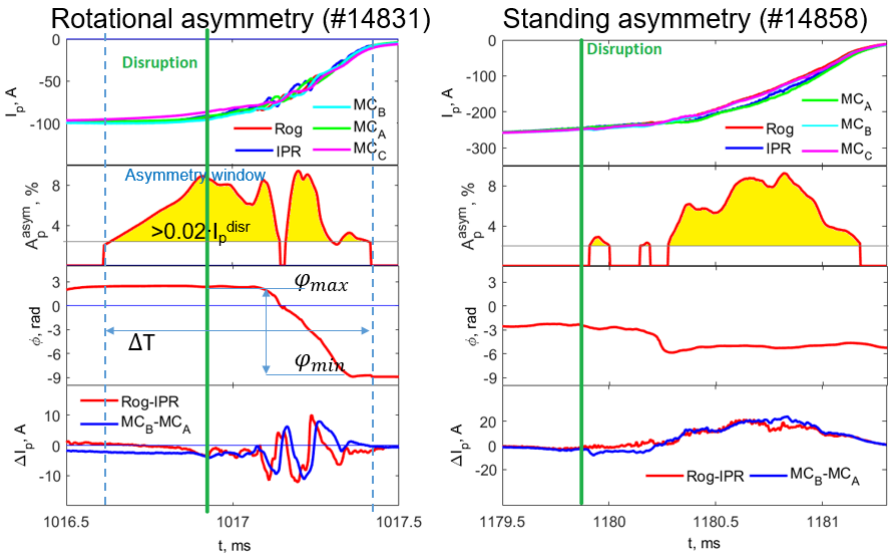

Figure 3.46: Left: rotational asymmetry during #14831 discharge. Right: standing asymmetry during #14858 discharge. From top to bottom: I_p measured at 5 toroidal positions; asymmetry magnitude A_p^{asym} trimmed at values $< 2\%$; asymmetry phase; plasma current difference at opposite toroidal positions $\Delta I_p = I_p^{MC-B} - I_p^{MC-B}$ and $\Delta I_p = I_p^{Rog} - I_p^{IPR}$

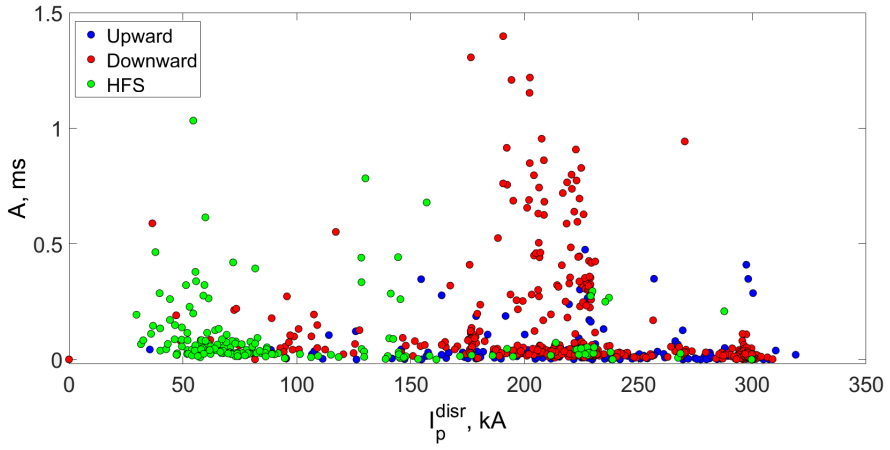

Figure 3.47: Time-integrated asymmetry A with respect to predisruptive plasma current I_p^{disr}. Directions of disruption are indicated by red color (downward), blue color (upward) and green color (HFS).

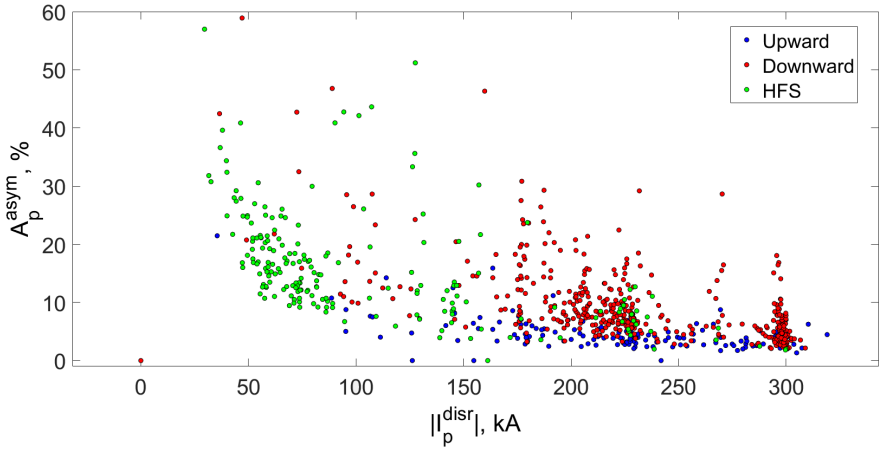

Figure 3.48: Normalised plasma current asymmetry magnitude I_p^{asym}/I_p^{disr} with respect to predisruptive plasma current I_p^{disr}. Directions of disruption are indicated by red color (downward), blue color (upward) and green color (HFS).

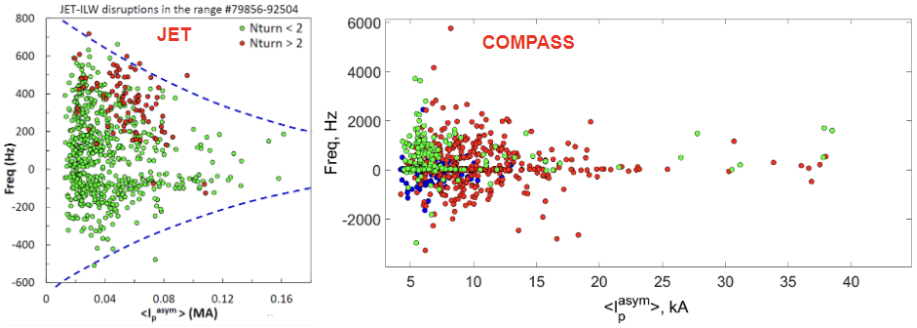

Figure 3.49: Frequency of asymmetry rotation with respect to the average value of I_p^{asym}. Left: JET results reported in [93] (figure by S.N. Gerasimov, CCFE, UK); Right: COMPASS data: upward disruptions are indicated by blue dots, downward disruptions - by red dots and HFS disruptions - by green dots.

The asymmetries at COMPASS rotate both in clockwise and counter-clockwise directions with a wide variety of frequencies. Positive frequencies correspond to anticlockwise direction of rotation, while negative frequencies indicated clockwise direction. It is observed both at JET [93] and at COMPASS that the rotational frequencies decrease at larger asymmetry magnitude. This is important for resonance avoidance, when the asymmetry frequency might coincide with the natural frequency of the vessel.

3.4.2 Halo current asymmetry

As the majority of disruptions at COMPASS are asymmetrical, this is manifested not only in I_p variation at different toroidal locations, but halo currents also undergo asymmetry. Toroidal peaking factor of halo current asymmetry can be roughly estimated using toroidal Mirnov coils. Note that Mirnov coils provide a very localised measurement in terms of toroidal direction. Therefore, the phase of the halo current plays a significant role and might lead to underestimation of TPF. 489 downward disruptions were used to determine TPF with Mirnov coils

#18 in Rings A, B and C. This coil was chosen as it is located in the region of the plasma-wall contact during downward disruptions. In addition to this it is one of the most robust coils after numerical integration (close to zero parasitic offset after disruption). TPF was calculated according to 2.13 at the peak of halo current sum across all rings of Mirnov coils: $max(I^A_{halo} + I^B_{halo} + I^C_{halo})$. TPF at COMPASS reach 2 at maximum while the halo fraction varies from 3 % tp 25 %. This is slightly lower compared to previously reported TPF up to 3 at COMPASS-D (as shown in Figure 2.4). However, it falls in line with other machines being closer to JET and MAST. No data points were found beyond ITPA boundary $F \cdot TPF = 0.7$.

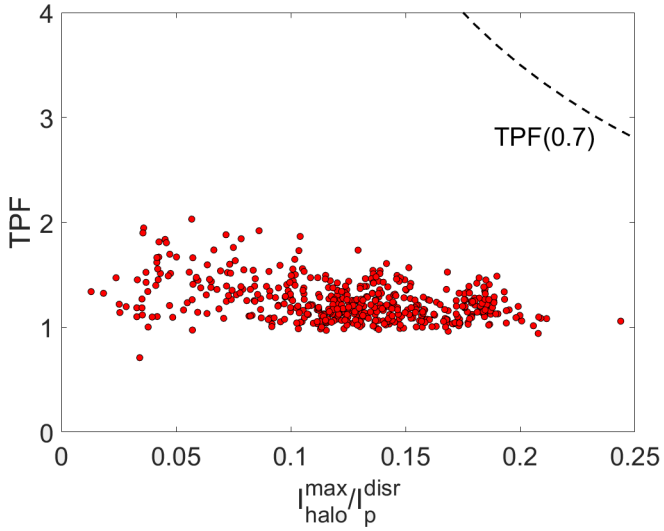

Figure 3.50: Toroidal peaking factor with respect to halo fraction $F = \frac{I^{max}_{halo}}{I^{disr}_{p}}$. ITPA limit of $F \cdot TPF = 0.7$ is marked by a dotted black line.

If the plasma asymmetry is represented as a m/n = 1/1 kink mode then it is natural to expect, that large asymmetries of I_p should correlate with larger TPF. This is due to plasma current transfer to the wall in the form of halo current. This tendency is depicted in Figure 3.52, where largest TPF tend to occur at larger asymmetry magnitudes A^{asym}_p as well as time-integrated values A.

An attempt has been made to relate directly the halo currents asymmetry and the plasma current asymmetry when measured in two opposite toroidal positions. It is expected that when part of I_p flows into the wall it gives rise to vessel currents in that position. Therefore, at given toroidal position the larger I_p should be accompanied by smaller halo current and vice versa. And example of such a case is shown in Figure 3.53 where the difference $I^{ringA}_{vessel} - I^{ringB}_{vessel}$ is depicted together with $I^{ringA}_{p} - I^{ringB}_{p}$. It can be seen that their time evolution is in counter-phase with respect to each other. While this supports the idea that halo current asymmetry and I_p asymmetry should be directly related, there are only few discharges that clearly show similar trend. The difficulty in data interpretation is connected with the phase of the asymmetry. Largest values of $I^{ringA}_{vessel} - I^{ringB}_{vessel}$ and $I^{ringA}_{p} - I^{ringB}_{p}$ can be observed only when the plasma column is tilted in the direction of Ring A or B (assuming m/n = 1/1 kink mode).

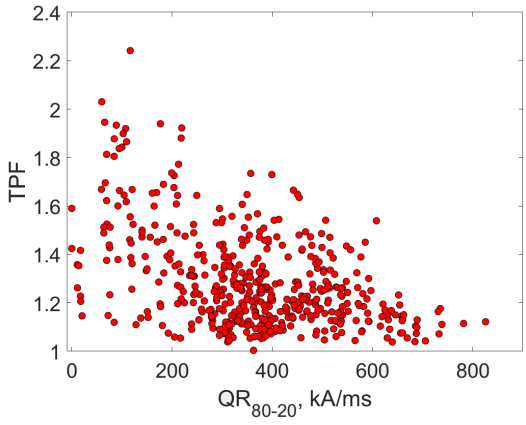

Figure 3.51: TPF with respect to current quench rate QR_{80-20}. All disruption directions are included. RE discharges are taken into account.

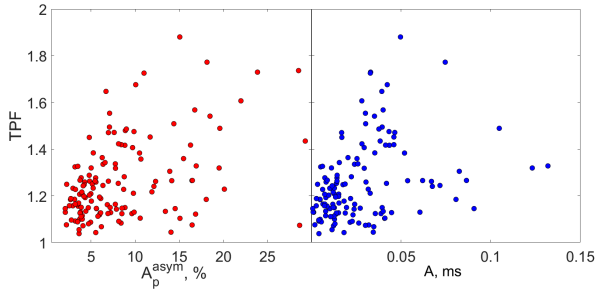

Figure 3.52: TPF with respect to plasma current asymmetry magnitude (left) and time-integrated value (right)

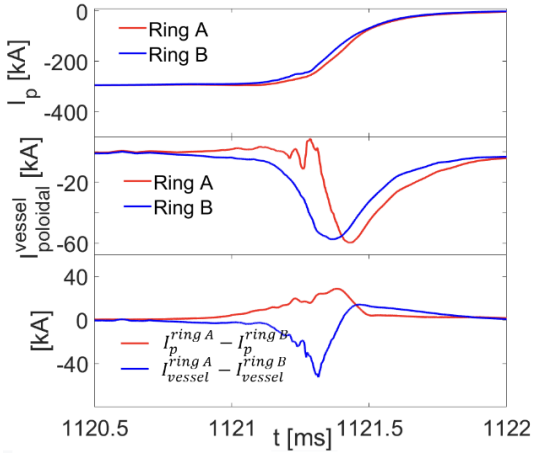

Figure 3.53: Halo current asymmetry with respect to the plasma current asymmetry in two toroidally opposite position. Discharge #18765 with downward disruption. Top: I_p measured by two toroidally opposite Mirnov coils Rings A and B. Middle: Poloidal vessel current during disruption measured by Mirnov coil #18 in Rings A and B. Bottom: Difference between the poloidal vessel currents and difference between the plasma currents measured in two opposite positions

3.5 Asymmetric Toroidal Eddy Currents

In addition to the vessel currents described in the previous Sections it is important to take into account PFCs and their effect on vessel current spatial distribution. Asymmetric Toroidal Eddy Currents model (ATEC) [94] suggests that toroidal eddy current might create a parallel circuit flowing from the vacuum vessel to the PFCs and short-circuiting the gaps between the PFCs. A schematic representation of ATEC model is shown in Figure 3.54. It depicts a toroidal section of JET vacuum vessel with dump plates. Upon plasma-wall contact part of toroidal eddy current (represented by green arrows) flows along the plates bridging the gaps between them. This phenomenon has two major consequences related to the electromagnetic loads and magnetic diagnostics operation. Firstly, the vertical component of the eddy current (when making its path from the vessel to the plate) will be coupled with toroidal magnetic field creating additional forces on the plates connections to the vessel. Secondly, magnetic pick-up coils (measuring poloidal magnetic field variation) placed behind the plates or the gaps between them will experience parasitic magnetic field contribution originated from the eddy currents. This effect can be illustrated by the coils #1 and #2 shown in Figure 3.54. Should these coils be used for I_p measurement, the coil #1 will pick up only the poloidal magnetic field variation induced by I_p. However, the coil #2 will detect both I_p and part of the eddy current leading to spurious signal. All in all, ATEC model predicts modified eddy currents path that has not been taken into account while estimating electromagnetic forces on the vacuum vessel or measuring I_p with magnetic diagnostics.

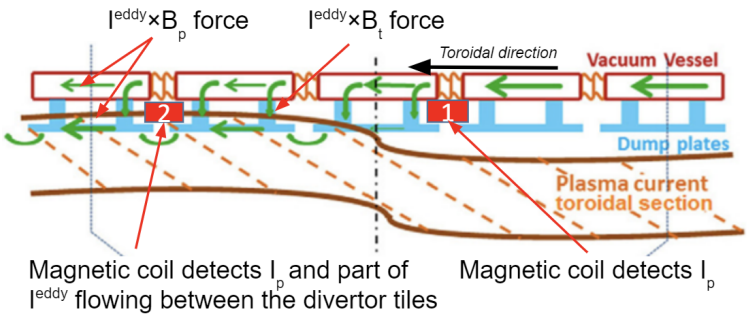

Figure 3.54: Schematic of the eddy current path according to ATEC model (modified Figure 2 in [94]). Toroidal section of the vacuum vessel with the dump plates is shown. Plasma is in contact with the plates on the left side of the schematic. Eddy currents (green arrows) are flowing toroidally in the vacuum vessel, while their fraction flows into the plates and through the gaps between them creating a parallel circuit. Possible positioning of magnetic pick-up coils is represented by red squares. The coil #1 detects poloidal filed variation induced by I_p, while the coil #2 experiences parasitic poloidal field from the eddy current flowing in the dump plates.

A first attempt of ATEC model experimental validation was done at the COMPASS tokamak in collaboration with ITER Organization under the service contracts $ITER/18/CT/4300001652$ and $IO/20/CT/4300002104$ covering the period of 21.03.2018 – 21.12.2019 and 13.05.2019 – 13.05.2020, respectively.

The author of this thesis contributed to conduction of experiments and data analysis. The author was also responsible for preparation of deliverable report on the hardware installation and experimental results interpretation. This Section summarizes the obtained results.

The aim of the experiments was to determine whether part of the vessel eddy current is transferred to the divertor tiles and flows in toroidal direction through the gaps between the tiles. Two special divertor tiles were installed in COMPASS allowing direct measurement of the current flow from the plasma to the divertor (halo current). The tiles are positioned 135° apart toroidally (Figure 3.55). Each tile consists of several graphite segments mounted on the insulating Boron-Nitride backplate. While there is a number of segments in poloidal direction, some of the segments have a small gap making two toroidally separated pieces. Each segments is connected to a cable leading outside of the vacuum vessel, where it is grounded on the vessel port. Current flow from the plasma to the tile's segment and then to the vacuum vessel through the cable is detected by commercial Rogowski coils (Algodue MFC150) located outside of the vacuum vessel. Assuming uniform halo current flow to toroidally neighbouring segments with a gap, it is expected that both segments will measure identical current magnitude. Any deviation can be attributed to short-circuiting of the gaps and additional contribution due to eddy currents modified path. The experiment analysis relies on comparing the current flows to the segments with a gap and relating them to eddy current and halo currents paths.

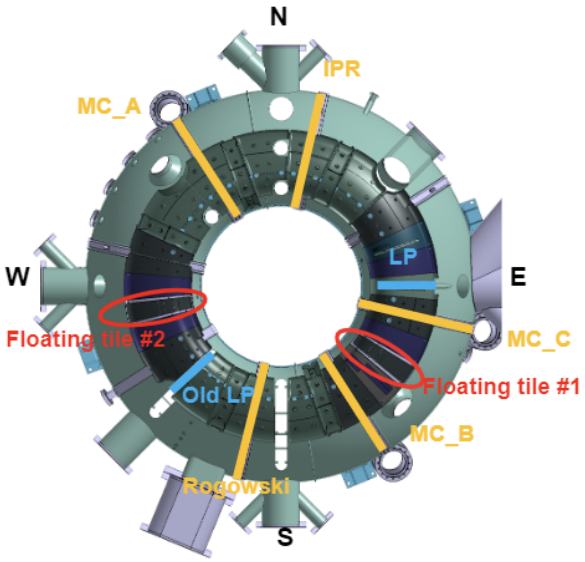

Figure 3.55: Special divertor tiles toroidal position location in the COMPASS tokamak vacuum vessel. The tiles are separated by 135°. Accompanying diagnostics are indicated as follows: full Rogowski coil – Rogowski; Mirnov coils (24 coils each ring, cover full poloidal cross section) - MC_A, MC_B, MC_C; Langmuir divertor probes – LP.

The experiment consisted of two phases with different tiles design (shown in Figure 3.56). During the first phase each tile had only one toroidally split segment (referred to as left and right segment, respectively) - Figure 3.56 (a). The two

tiles differ by the gap between their segments as well as to the neighbouring tiles. The tile #1 had 2.5 mm toroidal gap between the segments and larger gap to the neighbours (7.7-13 mm depending on the poloidal angle). The tile #2 had 10 mm and 2 mm gaps, respectively. The purpose of different gaps sizes was to investigate, whether it will improve or degrade possible short-circuiting. In the second phase the tiles design was revised and the number of split segments was increased to 6, forming 3 pairs of segments for investigation (Figure 3.56, b). The difference between the two phases of experiments are summarised in Table 3.4.

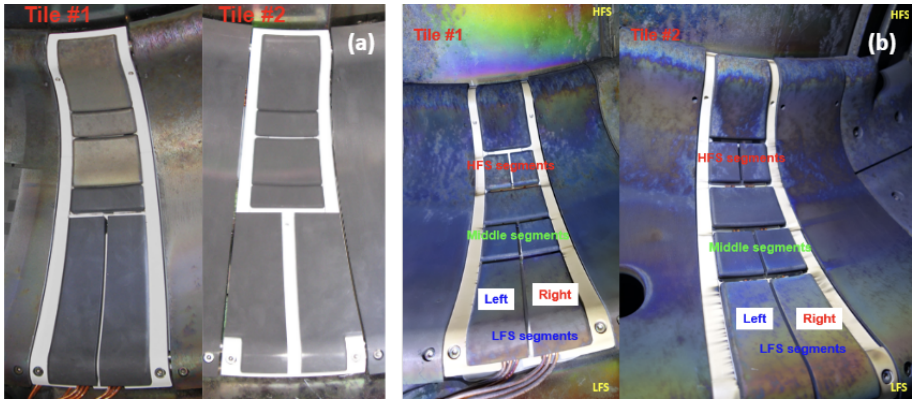

Figure 3.56: Special divertor tiles. Terminology: The investigation focuses on 3 pairs of toroidally split segments labelled as HFS, Middle and LFS segments respectively. The segments of each pair are called "Left" and "Right" (when looking from the top in the direction from the low field side LFS to the high field side HFS). Tile #1 and Tile #2 have identical gaps between the segments (2.5 mm) and to the neighboring standard divertor tiles (varies in 7.7 - 13.2 mm range depending on poloidal angle). The main difference between the tiles lies in cable leading. Tile #1 has its cables led through the feedthrough on the LFS, while tile #1 uses HFS feedthrough.

The positioning of the Rogowski coil on the cables outside of the vacuum vessel allowed several modifications of tile's segments connection. They are represented schematically represented in Figure 3.57 (a). Standard default configuration is grounded, meaning that the cables from the segments are connected to the vacuum vessel from the outside. Some of the segments can be disconnected completely. While the disconnected segments do not produce any measurement, they might affect the neighbouring segments. Floating configuration comprises the toroidally split segments connected to each other, while there is no electrical connection to the vacuum vessel. In the second phase of the experiments with revised tiles design an additional connection configuration was possible. The so-called cross-floating configuration uses similar principle as the floating one, but the segments from different poloidal angles are connected so each other. Each configuration explores various possible eddy currents paths and contributes to ATEC model understanding. The configurations of different pairs of toroidally split segments are independent and could be changed between individual discharges. This allowed investigation of different segments connection during one experimental session. The connection of the tiles and the measuring Rogowski coils outside of the vacuum vessel are shown in Figure 3.58. Each yellow-green

cable leads to one of the tile's segments. The length of the cables was kept as short as possible to minimise inductance affect. Rogowski coils (yellow) was fixed in a position to minimize pick up from toroidal magnetic field and to avoid variations of the PF cross-talks at different discharges.

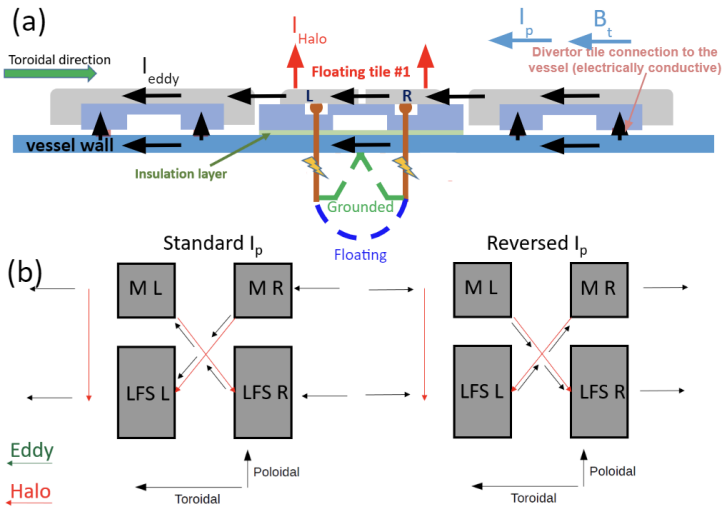

Figure 3.57: Schematic representation of experiment configurations. (a) Toroidal cross-section of toroidally split measuring segments are shown. Grounded mode (green): tile segment is connected to the VV outside of the chamber. Floating mode (blue): Left and right tile's segments are connected to each other and there is no connection to the vacuum vessel. Disconnected mode: cable leading from the tile segment is disconnected (the segment is fully floating). Left and right segments can be disconnected independently from each other. (b) Cross-floating mode. LFS Left segment is connected to Middle Right segment. LFS Right segment is connected to Middle Left segment. This option is not applicable to HFS segments.

Only downward VDEs discharges are of interest for these experiments. This is due to requirement of ATEC model that the gaps between PFCs can be short-circuited upon the contact with the plasma. It is possible to pre-programm direction of disruption at COMPASS using MARTe real-time plasma control system, which creates sudden vertical position shift emulating VDE in a requested direction. Therefore, the experiments included mainly discharges with forced downward VDEs, as the divertor with the special tiles is located in the bottom part of the COMPASS vacuum vessel. Several upward discharges and a vacuum discharge were also done as a preparation for the main experiments. This is to ensure an absence of large cross-talks with PF coils and absence of current flows to the tile when there is no contact with the plasma.

The experimental campaign plan aimed to repeat discharges with same requested plasma parameters varying only I_p flat-top magnitudes and directions of I_p and B_t. This was done to collect significant statistics and allow consistent comparison of different discharges. In addition to this, configurations of the segments connection were change throughout the experiments. The first phase of experiments contained 102 discharges and the second phase comprises 37 discharges. As a result, only about 5 discharges were obtained per each experimental

configuration. Additional information was collected during unintentional disruptions, as the special divertor tiles were left in the vacuum vessel until the end of COMPASS operation. Only grounded configuration of the segments was allowed during other experimental campaigns.

Phase 1	Phase 2
Non-identical tiles design	Identical tiles design
Only one pair of split segments LFS	3 pairs of split segments HFS, Middle, LFS
102 dedicated disruptions	37 dedicated disruptions
connection configurations: grounded, disconnected, floating	connection configurations: grounded, disconnected, floating + cross-floating
I_p=110, 190, 235, 275, 300 kA	I_p=300 kA
I_p and B_t direction change	I_p direction change
additional diagnostics: one set of Langmuir probes one fast visible camera	additional diagnostics: two sets of Langmuir probes two fast visible cameras

Table 3.4: Summary of two phases of ATEC validation experiments

An example of the first phase experiments results is shown in Figure 3.59. The segments of the main interest are toroidally split. They are labelled as Left and Right and are indicated by blue and red colors, respectively (Figure 3.59, a). The remaining segments also measure the current flows, but absolute values of the signals cannot be directly compared, as the segments have different collecting areas. It is worth noting that positive signal corresponds to halo current flowing from the plasma to the segment, while negative signal corresponds to the current flow direction from the segment to the plasma. However, what can be notice is that the sign of the current flow is opposite on the HFS and the LFS. Therefore, it can be seen, that in discharge shown in Figure 3.61 the halo current flows into the vessel on the HFS and flows out on the LFS. As it was noted in Section 2.2, the halo current direction depends only on B_t and not on I_p. The observed halo current flow is consistent with the standard direction of B_t at COMPASS (counter clockwise).

Several interesting observations have been made when studying a disruption with the segments in grounded mode (Figure 3.59). Current flow magnitudes up to 1.5 kA are detected at LFS split segments at flattop I_p around 300 kA. Note significant difference between the maximum current flows at tile #1 and tile #2 (up to ∼1 kA and ∼1.5 kA, respectively). In addition to this, tile #1 has substantial current flow asymmetry between its own neighbouring segments. Left segment reaches ∼0.5 kA, while Right segment has almost twice higher current flow magnitude ∼1 kA. It is assumed that the halo current flow to the toroidally neighbouring segments should be uniform. Therefore, no significant difference is expected between the current flows to Left and Right segments. The contradiction between this expectation and the observed results defined subsequent

Figure 3.58: Connection of the special divertor tiles segments in grounded configuration.

experimental campaign strategy. The aim was to find the origin of the asymmetry between Left and Right segments and its relation to ATEC model.

Several hypotheses were proposed to explain the Left-Right segments asymmetrical current flow:

- Eddy currents flowing through the gaps between the divertor tiles and increasing/decreasing the current flow of one of the segments.
- Non-uniform halo current flow due to shadowing by the neighbouring in-vessel structures.
- Non-uniform halo current flow due to misalignment of the segments.
- Non-uniform halo current due to measurement near the contact point.

It was shown that the contact point of the plasma (where poloidal magnetic field approaches zero) is located in the area of the toroidally split segments. This violates the main assumption of symmetric halo current flow to the segments. The halo current enters the plasma on the HFS from the contact point and exits the plasma on the LFS of the contact point, creating uncertainty in halo current flow measurement. The position of the contact point was tracked by divertor Langmuir probes (general reference) (Figure 3.60).

In addition to this tile #1 was positioned next to a divertor tile designed for infrared (IR) thermography. The IR tile has a rooftop shape and it was suspected that it could shadow the neighbouring tiles. Therefore, the halo current flow to the tile #1 could become non-uniform creating the asymmetry between Left and Right segments.

Another hypothesis to consider was possible misalignment of the segments during installation. Halo current flow to the segment depends on the angle between incident magnetic field lines and the collecting surface. The measurement

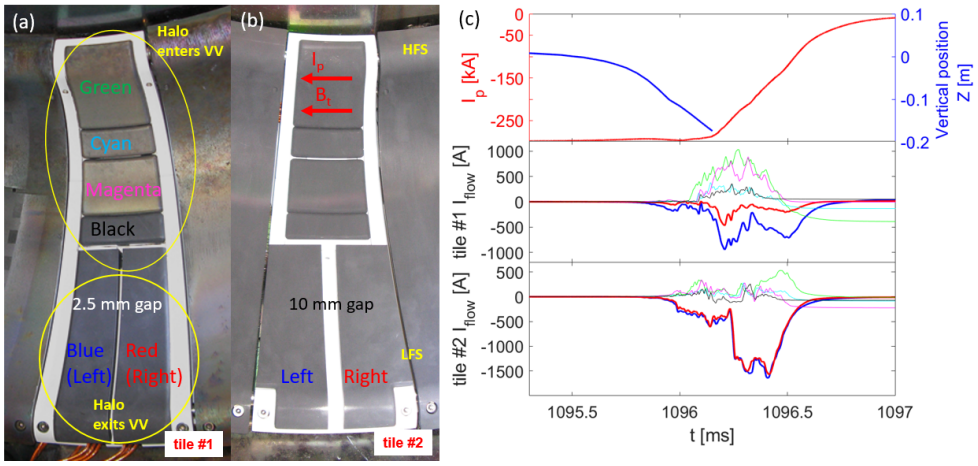

Figure 3.59: Special divertor tiles in the first phase of experiments. (a) Tile #1 (b) Tile #2 (c) Top: plasma vertical position Z (blue curve) and the plasma current I_p. Middle: current flows measured by tile #1. Blue curve - left segment. Red curve - right segment. Bottom: current flows measured by tile #2. Blue curve - left segment. Red curve - right segment.

becomes more sensitive to the surface alignment at the shallow incident angles of the magnetic field line. This is the case in the vicinity of the contact point.

All in all, the tiles design in the first phase of the experiments was not efficient for data interpretation mainly due to the contact point present on its surface. In addition to this, the behaviour of tile #1 and tile #2 was not consistent. While tile #1 exhibited significant current flow asymmetries between its Left and Right segments, tile #2 remained almost symmetrical. These led to reconsideration of the experimental strategy and proposal of newly designed tiles installation.

A revised tiles' design aimed to eliminate the effect of the contact point (Figure 3.56, b). The new design includes two identical segmentation of the tiles with the gaps of the same sizes (allowing easier comparison between the tiles). Each tile has 8 segments, 6 of them are making toroidally split pairs (HFS, Middle and LFS). Segments in each pair are referred to as Left and Right. While Middle segments are still significantly affected by the contact point presence, the investigation focuses on HFS and LFS segments.

In addition to the tiles' design revision, the IR divertor tile was replaced by a standard tile having plain surface. This was done to eliminate possible shadowing. Additional fast visible camera was put into operation to allow observation of both special divertor tiles. The cameras settings were adjusted to allow observation of disruptions (usually camera frames are saturated in that region). The data from the fast visible cameras was provided by Jordan Cavalier (IPP CAS). Two toroidally separated arrays of Langmuir probes were set in a special grounded to detect densities of the current flows from the plasma. The work related to Langmuir probes was done by Jiri Adamek (IPP CAS), Miglena Dimitrova (IPP CAS) and Jordan Cavalier (IPP CAS).

A typical measurement in grounded configuration is presented in Figure 3.61. Current flow magnitudes up to 1 kA are detected for a discharge with flattop I_p around 300 kA. It is assumed, that the halo current flow further from the contact point should be uniform resulting in equal signals to Left and Right toroidally

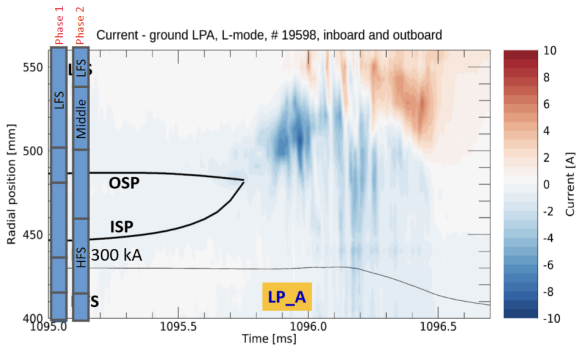

Figure 3.60: Currents measured by an array of divertor Langmuir probe in grounded mode. Respective position of the special divertor tiles segments (phase 1 and phase 2 designs) are shown on the left side. Change of the current sign corresponds to the contact point position. The contact point is observed in the area of toroidally split segment in phase 1 design. In phase 2 design the contact point falls onto the Middle segments area. Credits: the Langmuir probes measurements were performed and the figure was created by Jiri Adamek (IPP CAS).

split segments. However, the majority of discharges in the experimental campaign exhibit significant asymmetry between the segments in each pair - LFS, Middle and HFS. Only HFS and LFS pairs of segments are considered further as they are located further from the contact point.

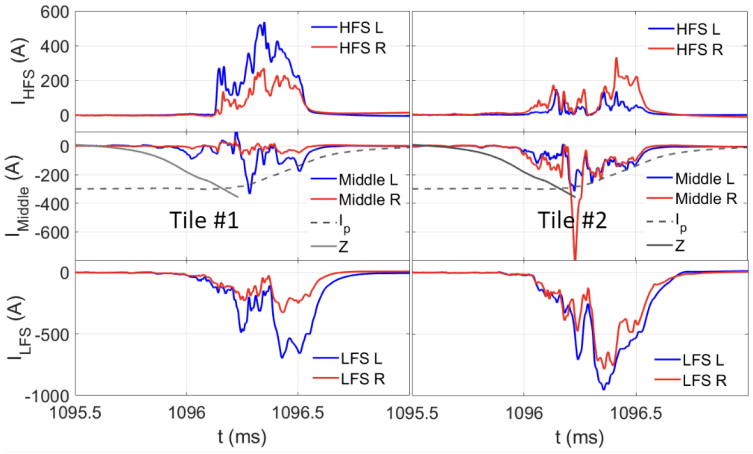

Figure 3.61: Divertor tiles' segments in grounded configuration (tile #1 on the left and tile #2 on the right) during disruption in #20807. HFS, middle and LFS segments are shown in the top, middle and bottom figures, respectively.

The tile #1 has largest asymmetries observe at the LFS, while HFS segments tend to have more symmetric current flow. The opposite is observed at the tile #1, where LFS segments exhibit more symmetrical current flow compared to the HFS. The symmetry detected at the peak of the halo flow is shown in Figure 3.62. Each tile has consistent behaviour throughout a number of disruptions with standard I_p and B_t directions and different plat-top I_p magnitudes. It can be noted, that on the LFS Left segment almost always has larger magnitude compared to Right segment. The opposite trend is observed on the HFS, where Right segment tend to dominate.

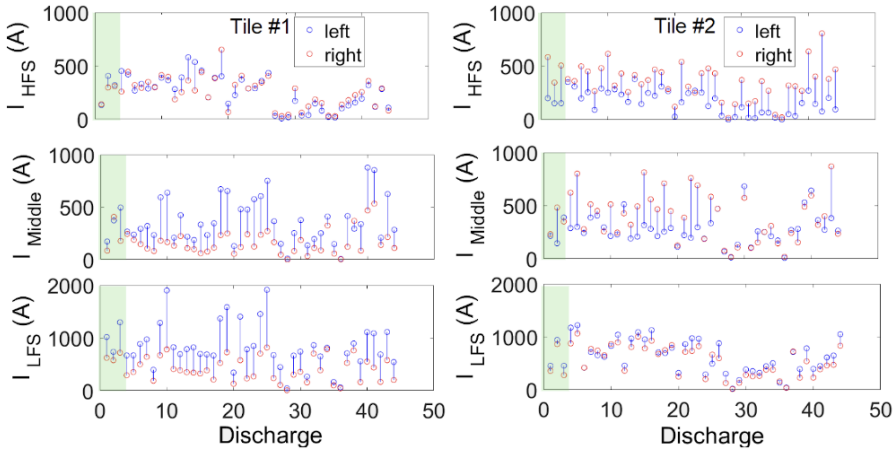

Figure 3.62: Instant current flows toward special divertor tiles at its maximum value. All segments are in grounded configuration. Discharges with various plasma currents are included. First 3 discharges (highlighted in green) belong to dedicated VDE campaigns (#20806- 20808), while the rest are unintentional disruptions (#20726, 20729, 20730, 20732- 20734, 20737, 20738, 20740, 20749, 20751, 20752, 20757, 20836, 20837, 20839, 20840, 20841, 20843, 20844, 20846, 20847, 20853, 20855, 20897, 20900, 20961- 20964, 20968, 20971).

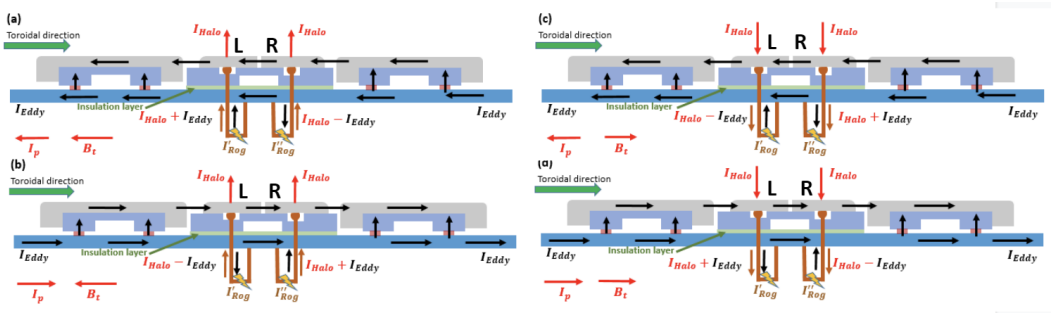

Figure 3.63: ITER halo eddy combination

The main hypothesis to explaine the described asymmetry considers combination of halo and eddy currents detected by the toroidally split segments. The proposed principle is illustrated in Figure 3.63. The Figure depicts toroidal section of the vacuum vessel with the special divertor tile having a gap between its segments (central tile in the Figure). The neighbouring tiles to the left and to the right are standard divertor tiles, meaning that they are electrically connected to the vacuum vessel inside the chamber, while the special tile has Boron-Nitride isolation layer. The section in Figure 3.63 shows the LFS segments viewed from the LFS of the vessel as an example, although the same principle can be applied to the Middle and HFS segments. The halo current on the LFS from the contact point flows from the vacuum vessel to the plasma (out of the tiles - red arrows in Figure 3.63) at the standard counter-clockwise direction of B_t. The toroidal eddy current during CQ flows in co-I_p direction (black arrows in Figure 3.63). Assuming that the plasma penetrates more the larger gaps on the sides of the special divertor tile enhancing the conductivity of the gaps the path of the eddy current will lead to the asymmetry between the split segments. The Left segment

will detect a sum of the halo and the eddy currents $I_L = I_{Halo} + I_{Edyy}$, while the Right segment will detect the difference $I_R = I_{Halo} + I_{Edyy}$ (Figure 3.63, a). Note that on the HFS from the contact point the halo current flows from the plasma to the tiles (equivalent to Figure 3.63, c), hence $I_L = I_{Edyy} - I_{Halo}$ and $I_R = I_{Halo} + I_{Edyy}$. The combination of the currents changes as I_{Halo} and I_{Edyy} change sign with B_t and I_p direction, respectively (Figure 3.63, b and d). The described approach suggest the following relation between the currents magnitudes detected by the Left and Right segments:

-	LFS segments	HFS segments
Standard I_p and standard B_t (Figure 3.63, a)	$I_L > I_R$	$I_L < I_R$
Reversed I_p and standard B_t (Figure 3.63, b)	$I_L < I_R$	$I_L > I_R$
Standard I_p and reversed B_t (Figure 3.63, c)	$I_L < I_R$	$I_L > I_R$
Reversed I_p and reversed B_t (Figure 3.63, d)	$I_L > I_R$	$I_L > I_R$

Table 3.5: Relation between Left and Right segments' currents magnitudes

An example of the Left and the Right segments relation change with I_p reversal is illustrated in Figure 3.64 for the tile #1. The current magnitudes of the Left segment on the LFS tend to be larger compared to the Right segment. The ratio reverses after I_p direction is switched from counter-clockwise to clockwise. An opposite trend is observed on the HFS as the halo current flows into the tiles there. This observation is consistent with the hypothesis that the gaps are short-circuited and the eddy current contributes to the segments measurements.

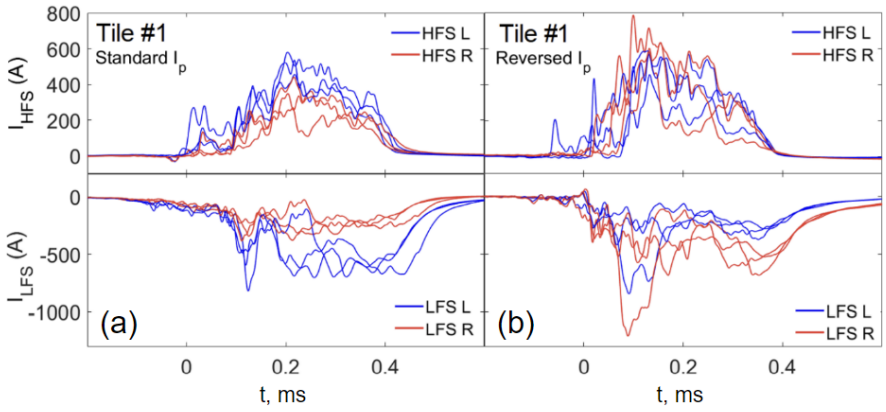

Figure 3.64: Current flows time evolution. Blue curve: current measured by the Left segment of the tile; red curve: current measured by the Right segment of the tile. Significant asymmetry between left and right segments measurements is observed. (a) Tile #1 standard I_p (# 20806, 20807, 20808) (b) Tile #1 reversed I_p (# 21004, 21005, 21006)

So-called floating configuration aim to investigate current flows behaviour when the Left and the Right segments are connected to each other, while there is no connection to the vacuum vessel at any point. Short-circuiting of the gaps should result into current flowing between the segments in co-I_p direction at standard I_p and in counter-I_p direction at reversed I_p. This effect is illustrated in Figure 3.65, where the signals from the Left segments of the tile #1 and the tile

Segment	**Standard I_p**		Reversed I_p	
	tile #1	**tile** #2	**tile** #1	**tile** #2
HFS	Co-I_p	Co-I_p	Co-I_p	Co-I_p
Middle	not clear	Counter-I_p	not clear	Co-I_p
LFS	Co-I_p	Counter- then co-I_p	not clear	Counter- then co-I_p

Table 3.6: Positions of toroidal-ϕ, poloidal-θ and radial-R Mirnov coils.

#2 are shown. Note that since the Left and the Right segments are connected to each other, the currents that they measure have same magnitude, but opposite signs.

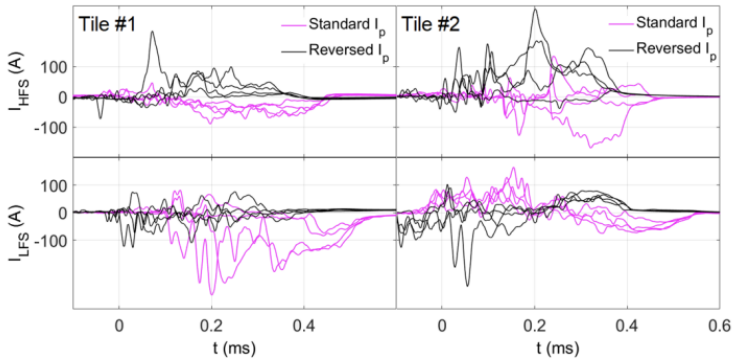

Figure 3.65: Current flows in floating configuration for the tile #1 (a) and the tile #2 (b). Only Left segment signal is shown for simplicity (the Right segment measures same current with different sign). Magenta curve corresponds to standard I_p direction, black curve - reversed I_p direction. Negative signal correspond to the current flowing towards the segment.

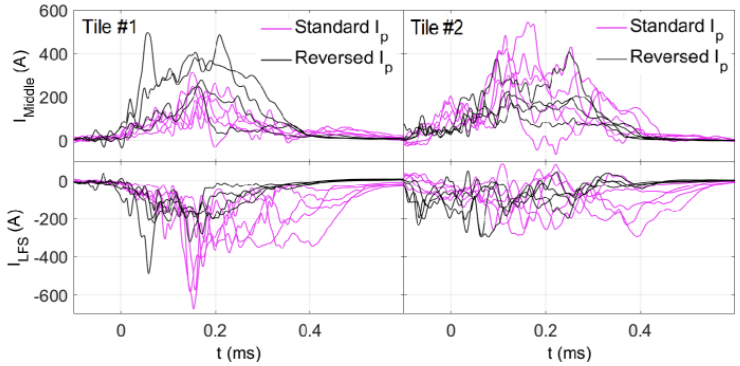

Figure 3.66: Current flows in cross-floating configuration for the tile #1 (a) and the tile #2 (b). Only LFS Left segment signal is shown for simplicity (the Right Middle segment measures same current with different sign). Magenta curve corresponds to standard I_p direction, black curve - reversed I_p direction. Negative signal correspond to the current flowing towards the segment.

A modification of floating configuration referred to as cross-floating is shown

in Figure 3.57 (b). In this case, the halo currents are expected to flow from the Middle segments towards the LFS. On the other hand, the eddy currents should flow from the Right to the Left segments (at standard I_p and B_t). In the absence of eddy currents contribution the currents measured between both pairs of connected segments should be equal. However, eddy currents flowing through the gaps (as ATEC predicts) will give rise to the Left LFS segment signal, while decreasing the Left Middle segment signal. The resulting signals are shown in Figure 3.66. The described ratio reverses upon the change of I_p direction. The effect is more pronounced at the tile #1, while no clear dependence can be seen at the tile #2. This might be due to closeness of the Middle segment and the contact point of the plasma.

While grounded, floating and cross-floating configurations indicated that there is a short-circuiting of the gaps between the divertor tiles there were other hypotheses that had to be eliminated for better understanding of the measured current flows. This was done with the help of additional diagnostics such as two fast visible cameras (references)(Figure 3.70) and two sets of divertor Lagmuir probes at different toroidal positions.

Some sparks were observed in the gaps between the segments (Figure 3.67), which could be attributed to arcing. This concern was also raised after inspecting the segments state when they were dismounted from the vacuum vessel. The sides of some segments had groups of small burns as can be seen in Figure 3.68. However, not all of the segments exhibited sparks or traces of burns on the sides and no direct correlation was found with the consistently observed asymmetry between the Left and the Right segments.

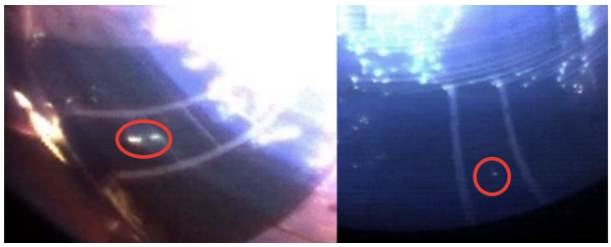

Figure 3.67: Two fast visible cameras' frames observing tile #1 (left) and tile #2 (right) during disruption. Sparks are observed in the gaps between the segments.

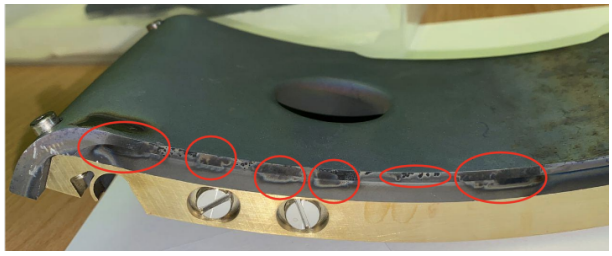

Figure 3.68: A standard divertor tile neighbouring special divertor tile #2 from the left side (when looking from the top). The standard divertor tile was dismounted after the dedicated VDE experiments. It exhibits traces of burns on the edges.

In addition two this, toroidal asymmetry of the plasma should be considered.

As it was described in Section 3.4, the majority of disruptions at COMPASS undergo large toroidal asymmetry resulting in a vertical tilt or/and radial shift of the plasma column. In certain discharges it can be also visibly observed by the fast cameras (as in Figure 3.70). The asymmetry might affect the positioning of the plasma contact point. This effect can be indicated by the two sets of Lagmuir probes separated toroidally and located in the vicinity of the special divertor tiles. Each set of the probes regularly measure plasma floating potential. The change of sign of the floating potential corresponds to the contact point position. Figure 3.69 shows the sign of the floating potential and approximate position of the contact point with respect to the special divertor tiles positions. It can be seen that at the toroidal position closer to the tile #1 the contact point lies closer to the LFS, while near the tile #2 the contact point is shifted closer to the HFS. This might explain the different magnitudes of the current flows to the tile #1 and the tile #2 (due to different halo current density).

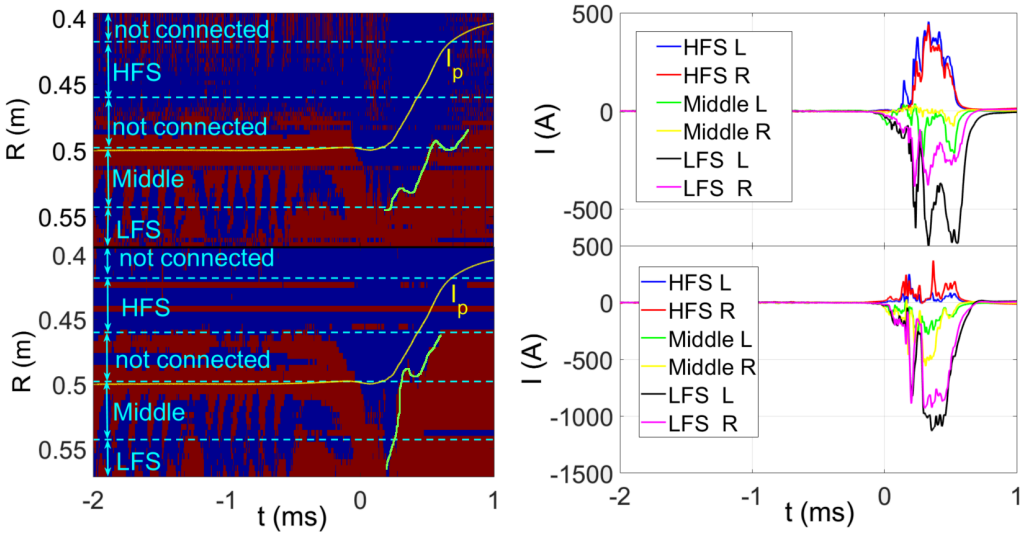

Figure 3.69: Left: contact point position during disruption estimated with two sets of Langmuir probes at different toroidal positions. Right: current flows to the special divertor tiles that are located in the vicinity of the Langmuir probes (tile #1 in the top and tile #2 in the bottom).

To summarise, two phases of experiments at the COMPASS tokamak provided a substantial ground for ATEC model validation. The current flows from the plasma to the two specifically designed divertor tiles were successfully measured. Additional diagnostics such as magnetics, Langmuir probes and fast visible cameras were available. It was noted that the detected current flows varied significantly from discharge to discharge with similar plasma parameters. Although tile #1 and tile #2 behaved differently, each of them individually exhibited consistent trends throughout the experiments. The revised tiles design allowed more extensive investigation thank to three pairs of measuring segments. The HFS and LFS segments are located far from plasma-wall contact point and are assumed to collect symmetric halo current flow. The following conclusions were made based on the current flows measurements with the revised tiles design:

- The gap size between the tile's segments and to the neighbouring tiles did

not affect the measurements. This was based on tile #2 measurements that showed similar results in the first and second phases of the experiments, although its design and gap sizes had changed.

- The asymmetry between the segments is not cause by shadowing from the neighbouring in-vessel structures. Tile #1 continued exhibiting asymmetrical behaviour even when the neighbouring IR tile (possible cause of the shadow) was removed.
- The asymmetry between the segments cannot be caused purely by their misalignment. While small tilt of the tiles could cause halo current flow asymmetry near the contact point, it does not play role on the LFS and HFS segments.
- Asymmetry between Left and Right segments in grounded configuration depend on I_p and B_t direction. This is consistent with ATEC model. However, some outliers were observed.
- The two tiles exhibit different trends: while tile #1 shows larger asymmetries on the LFS, tile #2 shows them in the HFS. This might be explained by major toroidal asymmetry of disruptions and shift of the contact point closer to the LFS in case of tile #1.
- Significant currents measured at floating configuration support ATEC model. This current also depends on I_p direction, although not all pairs of segments are consistent with ATEC predictions (the current should be always in co-I_p direction). This might be due to toroidal vessel currents changing their sign when transiting from the phase of vertical displacement to current quench.
- Cross-floating configuration showed that the tiles detect primarily the halo currents. However, an asymmetry is also observed on cross-floating configuration. The asymmetry dependence on I_p direction is consistent with ATEC model predictions.

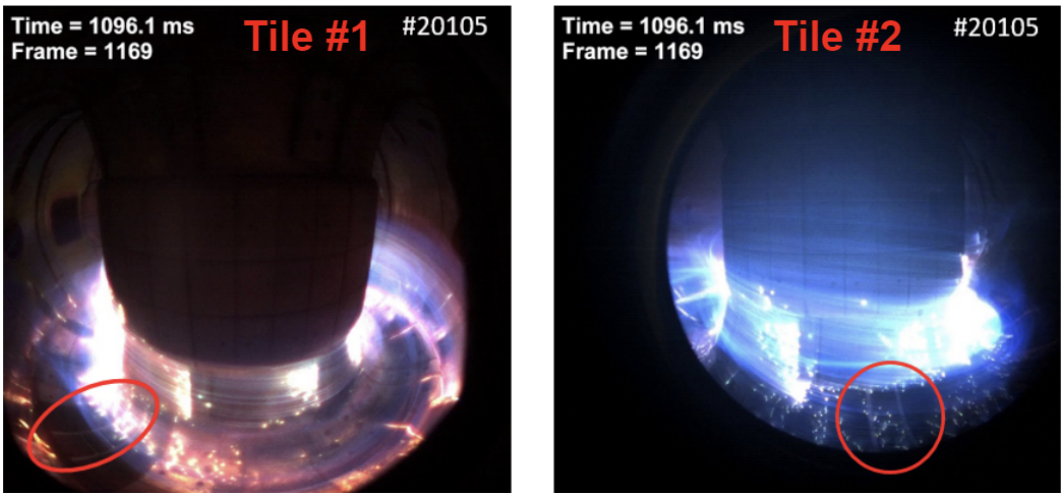

Figure 3.70: Two fast visible cameras' frames observing tile #1 (left) and tile #2 (right) during disruption in discharge #20105

Conclusion

Disruptions pose a severe threat to sustainable operation of tokamak devices. Investigation of electromagnetic loads during disruptions and underlying physical processes is a fundamental problem for design of the vacuum vessel that is able to withstand disruptions. Therefore, characteristic features of the current quench and related vessel currents need to be explored.

The COMPASS tokamak operated from 2008 to 2021 and provided an extensive disruption database consisting of ∼7000 entries. The thesis provides an overview of disruption characteristics at COMPASS. The work focuses on the final stages of disruption such as vertical displacement and plasma current quench. Special attention is given to the currents induced in the vacuum vessel during disruptions.

Section 1.1 gives an overview of disruption causes, phases and consequences. In section 2.2 the main sources of electromagnetic loads during disruptions are described. It was pointed out that each phase of disruption, such as plasma column motion, thermal quench and current quench induces poloidal and toroidal vessel currents that might by localized poloidally and also exhibit toroidal asymmetry.

The main results of this work are presented in chapter 3. It starts with an overview of the COMPASS disruption database which comprises disruptions in circular plasma, hot VDEs, major disruptions as well as minor disruptions at a large variety of plasma parameters. It was noted that time of vertical displacement during major disruptions is comparable to the plasma current quench time, which is an uncommon feature among other machines.

Section 3.1 gives a comprehensive description of magnetic diagnostics used in disruption investigation. It major advantage is capability to measure plasma current and local vessel currents in several toroidal positions. This allowed studies of 3D deformations of the plasma during disruptions which are manifested in plasma current toroidal asymmetries. This phenomenon requires precise measurement of I_p. Significant part of this thesis was devoted to modification of the data acquisition system and post-processing of the collected data to enable robust calculation of the plasma current asymmetries. Previously numerical integration of Mirnov coils in Rings A and C impeded their consideration in routine reconstruction of I_p because the sensitivity of DACs resulted in accumulation of errors and parasitic signals during disruption. New method of combination of two channel with different sensitivities was successfully implemented and significantly improved the processed data quality. Addition of Mirnov coils Rings A and C to the already used Rogowski coil, IPR coils and Mirnov coils Ring B (that have analogue integration) to I_p calculation enabled reliable determination of I_p asymmetries. In addition to this, for the first time at COMPASS all 3 rings of toroidal Mirnov coils were connected to the data acquisition system and their signals were used for poloidal vessel current determination. Modification of DAC integration gain was suggested and implemented to improve the data quality.

In section 3.2 typical COMPASS disruption parameters are statistically analyzed and compared to other machines.

Minimum area-normalised current quench time τ_{CQ}=2.1 ms/m^2 was determined at COMPASS. The parameter plays role in induction of eddy currents and its prediction for ITER relies on multiple-device statistics. τ_{CQ} at COMPASS is comparable to other European tokamaks such as JET, DIII-D, TCV and ASDEX-U (when RE are not taken into account) and lies above the universal lower bound 1.67 ms/m^2 (determined from several tokamaks in international disruption database IDDB).

It was noted that discharges with significant runaway electron fraction can result in extremely fast disruptions up to $\sim$ 6000 kA/ms. In general, non-RE disruptions have relatively narrow range of current quench times up to $\sim$1 ms. While fast runaway electron disruptions usually occur at relatively low I_p and do not induce large electromagnetic loads, they should not be completely excluded from consideration when determining lower limit of τ_{CQ}.

Section 3.3 deals with the currents flowing in the vacuum vessel during disruptions. These currents are the source of electromagnetic forces acting on the machine. The currents associated with each phase of disruption were measured by an extensive set of magnetic coils. As expected, vertical motion of the plasma induces dipole-like toroidal currents in the top and bottom of the vacuum vessel. Thermal quench results in poloidal vessel currents that are symmetrical along the cross-section (unless affected by halo current presence). Current quench induces toroidal vessel currents in the co-I_p, which are poloidally localized in the region of plasma-wall contact.

A special type of currents - halo currents flow in the vessel poloidally during current quench. Firstly, halo current scaling $(I_p^{disr})^2/B_t$ that was previously observed at other machines (e.g. Alcator C-Mod) was confirmed. Secondly, an attempt was done to determine whether slower current quenches lead to larger halo current formation as it is expected at ITER. However, the range of observed quench rates was too narrow to make accurate conclusions. Finally, magnetic coils covering the whole poloidal cross-section allowed determination of the full width of the halo region, while other devices are capable to detect only part of it.

It was suggested in [82], that the halo current density might be limited by ion saturation current (which can be measured with Langmuir probes). It was also noticed, that halo current increases at larger I_p. Together with the halo current density limitation it implies that the halo current width has to grow with (I_p at a given halo current density. This hypothesis was confirmed in a dedicated experiment with forces downward vertical displacement events.

Section 3.4 is devoted to toroidally asymmetrical disruptions. It comprises I_p variation measured at 5 toroidal positions and halo current variation measured at 3 toroidal positions.

I_p asymmetries that can take up to $\sim$ 20 % of (I_p^{disr} in elongated plasma and reach almost 50 % in circular plasma. Most of the asymmetries at COMPASS are locked or slowly rotating, only few disruptions are making more than one full turn in toroidal direction. The rotation of asymmetries exhibited similar behaviour

to JET - their rotation in toroidal direction slows down at larger asymmetry magnitudes. This is important to consider when avoiding resonance with the natural frequencies of the vacuum vessel.

Asymmetry of halo current was observed and toroidal peaking factor was deduced. A product of halo fraction with respect to I_p and toroidal peaking factor $F \cdot TPF$ define sideway forces acting on the vacuum vessel. Empirically estimated bound across numerous machines is defined in international disruption database IDDB as $F \cdot TPF = 0.7$. COMPASS values lie in the range similar to JET and MAST and are placed relatively far from the limit, meaning that the sideway forces are not critical.

Section 3.5 considers the path of the vessel current in the scope of Asymmetric Toroidal Eddy Current model (ATEC). The dedicated experiments for ATEC model validation were carried out in collaboration with ITER Organization. Two specifically designed insulated divertor tiles were installed in the vacuum vessel. Halo current flow from the plasma to the vacuum vessel was measured directly by several segments of the tiles aiming to determine whether there is any short circuit between the segments in toroidal direction. The experiments were carried out in two phases with different tiles design. The first phase of experiments was not entirely conclusive due to the contact point of the plasma located on the surface of the measuring segment. Asymmetry of the current flow to the neighbouring segments of the tile indicated a possibility of the short-circuit (as ATEC predicts). However, several other hypotheses could also partly explain the measured signals. In the second phase of the experiments with revised tiles design the following observations were clarified:

- The size of the gap between the segments does not play a significant role in the asymmetry between them.
- The asymmetry is not caused by the shadowing from the neighbouring in-vessel structures.
- The asymmetry is not caused purely by misalignment of the neighbouring segments.
- The asymmetry behaviour depends on I_p and B_t directions and subsequently depends on eddy current and halo current directions (consistent with ATEC model).
- When the neighbouring segments of the same tile are connected to each other (with no connection to the vacuum vessel) there is a current flowing between them. The possible source for this current is through short-circuit of the gaps between the segments.
- Significant toroidal asymmetry of the plasma column is observed and could cause different magnitudes of the current flows measured by the two tiles.

This demonstrates that the neighbouring toroidal segments must be short-circuited. However, it is not clear whether the short-circuiting occurs through the gap between the segments or via an open magnetic field line that might connect the segment to the vacuum vessel in an entirely different location far from the tile.

This possibility requires further investigation.

To summarize, the main results achieved during the author's doctoral studies are:

- Thorough characterization of disruption features at the COMPASS tokamak with the focus on vertical displacement, current quench and associated vessel currents.
- Improvement of the data acquisition system and development of the post-processing algorithms for magnetic diagnostics used in disruptions studies. This allowed robust calculation of the plasma current at several toroidal positions.
- For the first time local poloidal vessel currents (including halo current) were measured at COMPASS thanks to connection of the new magnetic coils. It provided a unique opportunity to detect halo current extension on the full poloidal cross-section of the vessel. The obtained results combined with the Langmuir probes data confirmed a novel hypothesis - halo current limitation by ion saturation current.
- Asymmetrical disruptions studies were extended. An algorithm for plasma current asymmetries calculation using measurements at 5 toroidal positions was developed. Asymmetries of halo currents were considered.
- In collaboration with ITER Organization special divertor tiles were installed in the COMPASS tokamak to measure direct current flow from the plasma to the vacuum vessel. Dedicated vertical displacement events experiments were performed to validate asymmetric toroidal eddy currents model. The results indicated new possible path of the vessel currents that affects electromagnetic forces distribution on the vacuum vessel.

This work contributed to several disruption related articles in impacted journals [81, 82, 95, 96]. First-authored article "Current quench and vessel currents characterization at the COMPASS tokamak" was accepted for publication in Plasma Physics and Controlled Fusion journal in October 2022 and is now available online [2].

Bibliography

[1] K. Ikeda. Progress in the ITER physics basis. *Nuclear Fusion*, 47(6), 2007.

[2] E. Matveeva, J. Havlicek, J. Artola, et al. Current quench and vessel currents characterization at the COMPASS tokamak. *Plasma Physics and Controlled Fusion*, 2022.

[3] Samuel Wurzel and Scott Hsu. Progress toward fusion energy breakeven and gain as measured against the lawson criterion, 05 2021.

[4] V.P. Smirnov. Tokamak foundation in USSR/russia 1950–1990. *Nuclear Fusion*, 50(1):014003, 2009.

[5] Radomir Panek, O. Bilykova, V. Fuchs, et al. Reinstallation of the COMPASS-D tokamak in IPP ASCR. *Czechoslovak Journal of Physics*, 56:B125–B137, 10 2006.

[6] Radomir Panek, Milan Aftanas, Petra Bilkova, et al. First results of the compass tokamak. *Acta Technica CSAV (Ceskoslovensk Akademie Ved)*, 56:T31–T42, 01 2011.

[7] R. Panek, T. Markovic, P. Cahyna, et al. Conceptual design of the compass upgrade tokamak. *Fusion Engineering and Design*, 123:11–16, 2017. Proceedings of the 29th Symposium on Fusion Technology (SOFT-29) Prague, Czech Republic, September 5-9, 2016.

[8] P. Vondracek, R. Panek, M. Hron, et al. Preliminary design of the COMPASS upgrade tokamak. *Fusion Engineering and Design*, 169:112490, 2021.

[9] R Pánek, J Adámek, M Aftanas, et al. Status of the COMPASS tokamak and characterization of the first h-mode. *Plasma Physics and Controlled Fusion*, 58(1):014015, 2015.

[10] J. Krbec. *Measurement of edge plasma density by energetic beam of Li atoms on the COMPASS tokamak*. PhD thesis, Prague, 2013. Diploma thesis. Czech Technical University in Prague. Faculty of Nuclear Science and Physical Engineering.

[11] J. Havlicek. *Study of Equilibrium Magnetic Configuration in Tokamak Type Devices*. PhD thesis, Charles University, Faculty of Mathematics and Physics, Prague, 2015. PhD thesis.

[12] V. Weinzettl, J. Adamek, M. Berta, et al. Progress in diagnostics of the compass tokamak. *Journal of Instrumentation*, 12:C12015–C12015, 12 2017.

[13] M. Lehnen, K. Aleynikova, P.B. Aleynikov, et al. Disruptions in ITER and strategies for their control and mitigation. *Journal of Nuclear Materials*, 463:39–48, 2015. PLASMA-SURFACE INTERACTIONS 21.

[14] B B.Kadomtsev. Behaviour of disruptions in tokamaks. *Plasma Physics and Controlled Fusion*, 26(1A):217–226, 1984.

[15] P.C. de Vries, M.F. Johnson, B. Alper, et al. Survey of disruption causes at JET. *Nuclear Fusion*, 51(5):053018, 2011.

[16] P.C. de Vries, G. Pautasso, E. Nardon, et al. Scaling of the MHD perturbation amplitude required to trigger a disruption and predictions for ITER. *Nuclear Fusion*, 56(2):026007, 2015.

[17] A. Murari, G. Vagliasindi, P. Arena, et al. Prototype of an adaptive disruption predictor for JET based on fuzzy logic and regression trees. *Nuclear Fusion*, 48(3):035010, 2008.

[18] S.P. Gerhardt, D.S. Darrow, R.E. Bell, et al. Detection of disruptions in the high-βspherical torus NSTX. *Nuclear Fusion*, 53(6):063021, 2013.

[19] G.F Matthews, P Andrew, T Eich, et al. Steady-state and transient power handling in JET. *Nuclear Fusion*, 43(9):999–1005, 2003.

[20] R.R. Khayrutdinov and V.E. Lukash. Studies of plasma equilibrium and transport in a tokamak fusion device with the inverse-variable technique. *Journal of Computational Physics*, 109(2):193–201, 1993.

[21] S.C. Jardin, N. Pomphrey, and J. Delucia. Dynamic modeling of transport and positional control of tokamaks. *Journal of Computational Physics*, 66(2):481–507, 1986.

[22] F. Villone, L. Barbato, S. Mastrostefano, et al. Coupling of nonlinear axisymmetric plasma evolution with three-dimensional volumetric conductors. *Plasma Physics and Controlled Fusion*, 55(9):095008, 2013.

[23] Jakub Hromadka, Josef Havlicek, Nisarg Patel, et al. Electromagnetic model for finite element analyses of plasma disruption events used in the design phase of the COMPASS-U tokamak. *Fusion Engineering and Design*, 167:112369, 2021.

[24] J.E. Menard, S. Gerhardt, M. Bell, et al. Overview of the physics and engineering design of NSTX upgrade. *Nuclear Fusion*, 52(8):083015, 2012.

[25] M. Buzio. *Structural effects of plasma instabilities on the JET tokamak*. PhD thesis, London Univ. (United Kingdom), 1999. PhD thesis.

[26] P. Noll, L. Sonnerup, C. Froger, et al. Forces on the jet vacuum vessel during disruptions and consequent operational limits. *Fusion Technol.; (United States)*, 15.

[27] R. L. Miller and R. W. Moore. Shape optimization of tokamak plasmas to localized magnetohydrodynamic modes. *Phys. Rev. Lett.*, 43:765–768, Sep 1979.

[28] F Troyon, R Gruber, H Saurenmann, et al. MHD-limits to plasma confinement. *Plasma Physics and Controlled Fusion*, 26(1A):209–215, 1984.

[29] J. Freidberg. *Plasma Physics and Fusion Energy, 1st ed.* Cambridge University Press, 2007.

[30] O Gruber, K Lackner, G Pautasso, et al. Vertical displacement events and halo currents. *Plasma Physics and Controlled Fusion*, 35(SB):B191–B204, 1993.

[31] Y. Nakamura, G. Pautasso, O. Gruber, et al. Axisymmetric disruption dynamics including current profile changes in the ASDEX-upgrade tokamak. *Plasma Physics and Controlled Fusion*, 44(8):1471–1481, 2002.

[32] F.J. Artola. *Free-boundary simulations of MHD plasma instabilities in tokamaks*. PhD thesis, Aix-Marseille University, Marseille, 2018. PhD thesis.

[33] D.A. Humphreys and I.H. Hutchinson. Filament-circuit analysis of Alcator C-MOD vertical stability. 02 2015.

[34] E.A. Lazarus, J.B. Lister, and G.H. Neilson. Control of the vertical instability in tokamaks. *Nuclear Fusion*, 30(1):111–141, 1990.

[35] Graham McArdle and D. Taylor. Adaptation of the mast passive current simulation model for real-time plasma control. *Fusion Engineering and Design - FUSION ENG DES*, 83:188–192, 2008.

[36] J. A. Leuer. Passive vertical stability in the next generation tokamaks. *Fusion Technology*, 15(2P2A):489–494, 1989.

[37] Paolo Bettini, M. Cavinato, and Francesco Trevisan. Dynamic identification of plasma magnetic contour in fusion machines. *Nuclear Fusion*, 45:1, 2004.

[38] A.J. Wootton and L. Wang. Tokamak position control. *IEEE Transactions on Plasma Science*, 18(6):1008–1020, 1990.

[39] S.C. Jardin and D.A. Larrabee. Feedback stabilization of rigid axisymmetric modes in tokamaks. *Nuclear Fusion*, 22(8):1095–1098, 1982.

[40] M. L. Walker and D. A. Humphreys. Valid coordinate systems for linearized plasma shape response models in tokamaks. *Fusion Science and Technology*, 50(4):473–489, 2006.

[41] M.M.M. Al-Husari, B. Hendel, I.M. Jaimoukha, et al. Vertical stabilisation of tokamak plasmas. In *[1991] Proceedings of the 30th IEEE Conference on Decision and Control*, pages 1165–1170 vol.2, 1991.

[42] J. William Helton, Kevin J. McGown, and Michael L. Walker. Conditions for stabilization of the tokamak plasma vertical instability using only a massless plasma analysis. *Autom.*, 46:1762–1772, 2010.

[43] V.D. Pustovitov. Disruption-induced poloidal currents in the tokamak wall. *Fusion Engineering and Design*, 117:1–7, 2017.

[44] F. Villone, G. Ramogida, and G. Rubinacci. Electromagnetic disruption analysis in IGNITOR. *Fusion Engineering and Design*, 93:57–68, 2015.

[45] Liu Sumei, Sun Jinxin, Lu Mingxuan, et al. Electromagnetic and structure analysis for EAST vacuum vessel with plasma facing components during VDE. *Fusion Engineering and Design*, 124:410–414, 2017. Proceedings of the 29th Symposium on Fusion Technology (SOFT-29) Prague, Czech Republic, September 5-9, 2016.

[46] Yusuke Shibama, Kei Masaki, Shinji Sakurai, et al. Design status of JT-60SA vacuum vessel. *J. Plasma Fusion Res. Ser.*, 9, 2010.

[47] M. Sugihara, M. Shimada, H. Fujieda, et al. Disruption scenarios, their mitigation and operation window in ITER. *Nuclear Fusion*, 47(4):337–352, 2007.

[48] L.L. Lao and T.H. Jensen. Magnetohydrodynamic equilibria of attached plasmas after loss of vertical stability in elongated tokamaks. *Nuclear Fusion*, 31(10):1909–1922, 1991.

[49] P. Andrew, P. Noll, and V. Riccardo. The relation between halo currents and plasma displacement/deformation in JET. In *17th IEEE/NPSS Symposium Fusion Engineering (Cat. No.97CH36131)*, volume 1, pages 108–111 vol.1, 1997.

[50] E.J. Strait, L.L. Lao, J.L. Luxon, et al. Observation of poloidal current flow to the vacuum vessel wall during vertical instabilities in the DIII-D tokamak. *Nuclear Fusion*, 31(3):527–534, 1991.

[51] V. Riccardo, T. C. Hender, P. J. Lomas, et al. Analysis of JET halo currents. *Plasma Physics and Controlled Fusion*, 46(6):925–934, 2004.

[52] V. Riccardo, G. Arnoux, P. Beaumont, et al. Progress in understanding halo current at JET. *Nuclear Fusion*, 49(5):055012, 2009.

[53] S. P. Gerhardt, E. Fredrickson, L. Guttadora, et al. Techniques for the measurement of disruption halo currents in the National Spherical Torus Experiment. *Review of Scientific Instruments*, 82(10):103502, 2011.

[54] S.P. Gerhardt, J. Menard, S. Sabbagh, et al. Characterization of disruption halo currents in the National Spherical Torus Experiment. *Nuclear Fusion*, 52(6):063005, 2012.

[55] G. Pautasso, L. Giannone, O. Gruber, et al. The halo current in ASDEX upgrade. *Nuclear Fusion*, 51(4):043010, 2011.

[56] T.E. Evans, A.G. Kellman, D.A. Humphreys, et al. Measurements of non-axisymmetric halo currents with and without 'killer' pellets during disruptions in the DIII-D tokamak. *Journal of Nuclear Materials*, 241-243:606–611, 1997.

[57] G. F. Counsell, R. Martin, T. Pinfold, et al. On the magnitude and distribution of halo currents during disruptions on MAST. *Plasma Physics and Controlled Fusion*, 49(4):435–446, 2007.

[58] F. Saint-Laurent, P. , Houy, G. , Martin, et al. Halo currents in a circular tokamak: measurements on Tore Supra. *26th EPS conference on controlled fusion and plasma physics, Maastricht (Netherlands)*, 1999.

[59] Y. Neyatani, R. Yoshino, and T. Ando. Effect of halo current and its toroidal asymmetry during disruptions in JT-60U. *Fusion Technology*, 28(4):1634–1643, 1995.

[60] Chen Da-Long, Granetz Robert, Shen Biao, et al. Characterization of plasma current quench during disruption in EAST tokamak. *Chinese Physics B*, 24(2):025205, 2015.

[61] P.J Knight, G.G Castle, A.W Morris, et al. Analysis of vertical displacement events and halo currents in COMPASS-D. *Nuclear Fusion*, 40(3):325–337, 2000.

[62] D. A. Humphreys and A. G. Kellman. Analytic modeling of axisymmetric disruption halo currents. *Physics of Plasmas*, 6(7):2742–2756, 1999.

[63] S.N. Gerasimov, T.C. Hender, M.F. Johnson, et al. Scaling JET disruption sideways forces to ITER. In *37th EPS Conference on Plasma Physics*, 2010.

[64] R.S Granetz, I.H Hutchinson, J Sorci, et al. Disruptions and halo currents in Alcator C-Mod. *Nuclear Fusion*, 36(5):545–556, 1996.

[65] Y Neyatani, R Yoshino, Y Nakamura, et al. Characteristics of halo currents in JT-60U. *Nuclear Fusion*, 39(4):559–567, 1999.

[66] N.W. Eidietis, S.P. Gerhardt, R.S. Granetz, et al. The ITPA disruption database. *Nuclear Fusion*, 55(6):063030, 2015.

[67] T.C Hender, J.C Wesley, J Bialek, et al. Chapter 3: MHD stability, operational limits and disruptions. *Nuclear Fusion*, 47(6):S128–S202, jun 2007.

[68] S.N. Gerasimov, P. Abreu, M. Baruzzo, et al. JET and COMPASS asymmetrical disruptions. *Nuclear Fusion*, 55(11):113006, 2015.

[69] V Riccardo, S Walker, and P Noll. Modelling magnetic forces during asymmetric vertical displacement events in JET. *Fusion Engineering and Design*, 47(4):389–402, 2000.

[70] Tyge Schioler, Christian Bachmann, Giuseppe Mazzone, et al. Dynamic response of the ITER tokamak during asymmetric VDEs. *Fusion Engineering and Design*, 86(9):1963–1966, 2011. Proceedings of the 26th Symposium of Fusion Technology (SOFT-26).

[71] Allen H. Boozer. Rotation of tokamak halo currents. *Physics of Plasmas*, 19(5):052508, 2012.

[72] C.F. Clauser, S.C. Jardin, and N.M. Ferraro. Vertical forces during vertical displacement events in an ITER plasma and the role of halo currents. *Nuclear Fusion*, 59(12):126037, 2019.

[73] D. Pfefferlé, N. Ferraro, S.C. Jardin, et al. Modelling of NSTX hot vertical displacement events using M3D-C1. *Physics of Plasmas*, 25:056106, 05 2018.

[74] I. Krebs, F. Artola, C. Sovinec, et al. Axisymmetric simulations of vertical displacement events in tokamaks: A benchmark of M3D-C^1, NIMROD and JOREK, 2019.

[75] C R Sovinec and K J Bunkers. Modelling of NSTX hot vertical displacement events using M3D-C1. *Plasma Phys. Control. Fusion*, 61(2):024003, 2019.

[76] D.F. Valcárcel, A.S. Duarte, A. Neto, et al. Real-time software for the COMPASS tokamak plasma control. *Fusion Engineering and Design*, 85(3):470–473, 2010. Proceedings of the 7th IAEA Technical Meeting on Control, Data Acquisition, and Remote Participation for Fusion Research.

[77] J. Mlynar, M. Imrisek, V. Weinzettl, et al. Introducing minimum fisher regularisation tomography to AXUV and soft x-ray diagnostic systems of the COMPASS tokamak. *Review of Scientific Instruments*, 83(10):10E531, 2012.

[78] J. Hugill. Transport in tokamaks – a review of experiment. *Nuclear Fusion*, 23(3):331–373, 1983.

[79] P.C. de Vries, M.F. Johnson, and I. Segui and. Statistical analysis of disruptions in JET. *Nuclear Fusion*, 49(5):055011, 2009.

[80] F. Salzedas, S. I. W. Shah, J. Havlicek, et al. Study of secondary instability of precursor magnetic island in COMPASS density limit disruptions. *Physics of Plasmas*, 27(2):022515, 2020.

[81] J. Adamek, F.J. Artola, A. Loarte, et al. Current density limitation during disruptions due to plasma-sheaths. *Nuclear Fusion*, 62(8):086034, 2022.

[82] F. J. Artola, A. Loarte, E. Matveeva, et al. Simulations of COMPASS vertical displacement events with a self-consistent model for halo currents including neutrals and sheath boundary conditions. *Plasma Physics and Controlled Fusion*, 63(6):064004, 2021.

[83] E. J. Strait, E. D. Fredrickson, J.-M. Moret, et al. Chapter 2: Magnetic diagnostics. *Fusion Science and Technology*, 53(2):304–334, 2008.

[84] J. Wesson and D.J. Campbell. *Tokamaks*. International Series of Monographs on Physics. OUP Oxford, 2011.

[85] D.F. Valcárcel, A. Neto, J. Sousa, et al. An ATCA embedded data acquisition and control system for the compass tokamak. *Fusion Engineering and Design*, 84(7):1901–1904, 2009. Proceeding of the 25th Symposium on Fusion Technology.

[86] Fateme Shakeri, Ardavan Kouhi, Bahram Jazi, et al. Measurement of plasma current in damavand tokamak using magnetic probes assembly as a discrete rogowski coil. *Fusion Engineering and Design*, 168:112414, 2021.

[87] S. Purohit, M.B. Chowdhuri, J. Ghosh, et al. Characterization of the plasma current quench during disruptions in ADITYA tokamak. *Nuclear Fusion*, 60(12):126042, 2020.

[88] J. WESLEY, A. HYATT, E. STRAIT, et al. Disruption characterisation and database activities for ITER. 2006.

[89] V.D. Pustovitov. Extended theory of diamagnetic measurements with account of the wall currents in tokamaks. *Fusion Engineering and Design*, 138:53–58, 2019.

[90] R. Yoshino, D. J. Campbell, E. Frederickson, et al. Characterization of disruption phenomenology in ITER. *17th IAEA Fusion Energy Conference, Yokohama, Japan, IAEA-CN-69, ITERP1/14*, 1999.

[91] O. Ficker, E. Macusova, J. Mlynar, et al. Runaway electron beam stability and decay in COMPASS. *Nuclear Fusion*, 59(9):096036, 2019.

[92] S.N. Gerasimov, T.C. Hender, J. Morris, et al. Plasma current asymmetries during disruptions in JET. *Nuclear Fusion*, 54(7):073009, 2014.

[93] S.N. Gerasimov. Evaluation of JET-ILW disruptions. In *ITPA MHD, 9-11 October 2017*, 2017.

[94] Riccardo Roccella, M. Roccella, Valeria Riccardo, et al. Asymmetric toroidal eddy currents (ATEC) to explain sideways forces at JET. *Nuclear Fusion*, 56:106010, 2016.

[95] J. Coburn, M. Lehnen, R.A. Pitts, et al. Energy deposition and melt deformation on the ITER first wall due to disruptions and vertical displacement events. *Nuclear Fusion*, 62(1):016001, 2021.

[96] J. Coburn, M. Lehnen, R.A. Pitts, et al. Reassessing energy deposition for the ITER 5 MA vertical displacement event with an improved DINA model. *Nuclear Materials and Energy*, 28:101016, 2021.

List of Figures

List of Tables

List of Abbreviations

COMPASS	Compact Assembly
ITER	International Thermonuclear Experimental Reactor
VDE	vertical displacement event
AVDE	asymmetric vertical displacement event
PFC	plasma facing component
H-mode/L-mode	plasma mode with higher/lower energy confinement
MHD	magneto-hydrodynamic
ATEC	asymmetric toroidal eddy current
ICF	inertial confinement fusion
MCF	magnetically confined fusion
HFS	high field side
LFS	low field side
DC	direct current
NBI	Neutral beam injection
RF	Radio-frequency
TPF	toroidal peaking factor
LCFS	last closed flux surface
SXR	soft X-ray
SND	single-null diverted
MFPS	Magnetising Field Power Supply
SFPS	Shaping Field Power Supply
EFPS	Equilibrium Field Power Supply
BR	Radial (horizontal) magnetic field
BV	Vertical magnetic field
ATCA	Embedded Data Acquisition and Control System, the name is derived fr
CDB	COMPASS DataBase
EPR	External Partial Rogowski coil
IPR	Internal Partial Rogowski coil
MARTe	tokamak control system at COMPASS - Multithreaded Application Rea
Nimbus	data acquisition system at COMPASS (NI PXIe-6368 cards used)
SF	Shaping Field
JET	Joint European Torus
SOL	scrape-of layer
TF	toroidal field
IPP CAS	Institute of Plasma Physics of the Czech Academy of Sciences
CQ	current quench
TQ	thermal quench
EM	electromagnetic
RE	runaway electrons
MC	Mirnov coil
DAC	data acquisition channel
ITPA	International Tokamak Physics Activity
IDDB	International Tokamak Physics Activity disruption database
QR	quench rate

List of publications

Impacted publications

[1] **E. Matveeva**, J. Havlicek., J. Artola, V. Yanovskiy, A. Havranek et al. Current quench and vessel currents characterization at the COMPASS tokamak. *Plasma Physics and Controlled Fusion* (2022). DOI: 10.1088/1361-6587/ac9928

[2] J. Adamek, F.J. Artola, A. Loarte, **E. Matveeva**, J. Cavalier et al, Current density limitation during disruptions due to plasma sheaths. *Nuclear Fusion* (2022). DOI: 10.1088/1741-4326/ac7656

[3] F. J. Artola, A. Loarte, **E. Matveeva**, J. Havlicek, T. Markovic et al, Simulations of COMPASS vertical displacement events with a self-consistent model for halo currents including neutrals and sheath boundary conditions. *Plasma Physics and Controlled Fusion* (2021). DOI: 10.1088/1361-6587/abf620

[4] J. Coburn, M. Lehnen, R.A. Pitts, G. Simic, F.J. Artola et al, Energy deposition and melt deformation on the ITER first wall due to disruptions and vertical displacement events. *Nuclear Fusion* (2021). DOI: 10.1088/1741-4326/ac38c7

[5] J. Coburn, M. Lehnen, R.A. Pitts, E. Thoren, K. Ibano et al, Reassessing energy deposition for the ITER 5 MA vertical displacement event with an improved DINA model. *Nuclear Materials and Energy* (2021). DOI: /10.1016/j.nme.2021.101016

[6] M. Hron et al, Overview of the COMPASS results. *Nuclear Fusion* (2022). DOI: 10.1088/1741-4326/ac301f

[7] P. Vondracek, R. Panek, M. Hron, J. Havlicek, V. Weinzettl et al, Preliminary design of the COMPASS upgrade tokamak. *Fusion Engineering and Design* (2021). DOI: 10.1016/j.fusengdes.2021.112490

[8] S.N. Gerasimov, P. Abreu, G. Artaserse, M. Baruzzo, P. Buratti et al, Overview of disruptions with JET-ILW. *Nuclear Fusion* (2020). DOI: 10.1088/1741-4326/ab87b0

Conference publications

[9] **E. Matveeva**, J. Havlicek, O. Hronova, V. Weinzettl, A. Havranek et al, Disruptions and Plasma Current Asymmetries in Tokamak Plasmas. *Proceedings of the 26th Annual Conference of Doctoral Students – WDS 2017.* MATFYZPRESS, Prague, 2017, ISBN 978-80-7378-356-3.

[10] **E. Matveeva**, O. Ficker, J. Havlicek, A. Havranek, O. Hronova et al, Statistical analysis of disruptions in COMPASS. *Proceedings of the 27th Annual*

Conference of Doctoral Students – WDS 2018. MATFYZPRESS, Prague, 2018, ISBN 978-80-7378-374-7.

[11] **E. Matveeva**, J. Havlicek, O. Hronova, A. Havranek, V. Weinzettl et al, Vessel currents during asymmetrical disruptions on COMPASS tokamak. *Proceedings of the 28th Annual Conference of Doctoral Students – WDS 2019*. MATFYZPRESS, Prague, 2019, ISBN 978-80-7378-409-6.

[12] **E. Matveeva**, J. Havlicek, R. Dejarnac, M. Jerab, D. Sestak et al, Current flows towards the divertor during VDEs at COMPASS. *Proceedings of the 29th Annual Conference of Doctoral Students – WDS 2020*. MATFYZPRESS, Prague, 2020, ISBN 978-80-7378-435-5.

[13] **E. Matveeva**, F.J Artola, J. Havlicek, M. Lehnen, R. Pitts et al, Current flows towards the divertor during VDEs at COMPASS. *Proceedings of the 30th Annual Conference of Doctoral Students – WDS 2021*. MATFYZPRESS, Prague, 2021, ISBN 978-80-7378-455-3.

[14] **E. Matveeva**, O. Ficker, J. Havlicek, A. Havranek, O. Hronova et al, Statistical analysis of disruptions in COMPASS. *45th EPS Conference on Plasma Physics 2 - 6 July 2018*. Vol. 42A ISBN: 979-10-96389-08-7. url: http://ocs.ciemat.es/EPS2018PAP/pdf/P1.1056.pdf

[15] V. Yanovskiy, N. Isernia, V. D. Pustovitov, F. Villone, J. Havlicek et al, Estimations of disruption forces in the COMPASS-U tokamak. *45th EPS Conference on Plasma Physics 2 - 6 July 2018*. Vol. 42A ISBN: 979-10-96389-08-7. url: http://ocs.ciemat.es/EPS2018PAP/pdf/P1.1059.pdf

[16] **E. Matveeva**, J. Havlicek, A. Havranek, V. Yanovskiy, V.D. Pustovitov et al, Toroidal and poloidal vessel currents during asymmetrical disruptions on COMPASS. *46th EPS Conference on Plasma Physics 8 - 12 July 2019*. Vol. 43C ISBN: 979-10-96389-11-7. url: http://ocs.ciemat.es/EPS2019PAP/pdf/P4.1040.pdf

[17] S.N. Gerasimov, P. Abreu, G. Artaserse, P. Buratti, I.S. Carvalho et al, Locked mode and disruptions in JET-ILW. *46th EPS Conference on Plasma Physics 8 - 12 July 2019*. Vol. 43C ISBN: 979-10-96389-11-7. url: http://ocs.ciemat.es/EPS2019PAP/pdf/P1.1056.pdf

[18] **E. Matveeva**, F. J. Artola, J. Havlicek, M. Lehnen, R. Pitts et al, Current flows towards the divertor during VDEs at COMPASS. *47th EPS Conference on Plasma Physics 21 - 25 June 2021*. Vol. 45A ISBN: 979-10-96389-13-1. url: http://ocs.ciemat.es/EPS2021ABS/pdf/P4.1034.pdf

[19] S.N. Gerasimov, P. Abreu, L.R. Baylor, A. Boboc, I.S. Carvalho et al, Mitigation of disruption electro-magnetic load with SPI on JET-ILW. *47th EPS Conference on Plasma Physics 21 - 25 June 2021*. Vol. 45A ISBN: 979-10-96389-13-1. url: http://ocs.ciemat.es/EPS2021ABS/pdf/P1.1031.pdf

A. Attachments

Attached publications

E. Matveeva, J. Havlicek., J. Artola, V. Yanovskiy, A. Havranek et al. Current quench and vessel currents characterization at the COMPASS tokamak. *Plasma Physics and Controlled Fusion* (2022). DOI: 10.1088/1361-6587/ac9928